CARBON AND OXYGEN INDUCED REACTIONS
ON THE N=28 NUCLEI

by

EMMANUEL CARMEL POLLACCO

A thesis submitted for the degree of
DOCTOR OF PHILOSOPHY
at the
AUSTRALIAN NATIONAL UNIVERSITY

November 1976

To My Parents

Preface

In this thesis the elastic and inelastic scattering and single neutron transfer induced by carbon and oxygen ions on N=28 nuclei are studied. The experimental work was performed in the Department of Nuclear Physics at the Australian National University.

The carbon elastic scattering and single neutron transfer reactions were measured by Dr D.M. Parkinson. The full theoretical analysis of these reactions was suggested by Dr D.C. Weisser and the calculations and interpretations of the results were performed by the author.

The inelastic scattering measurements were suggested by Dr J.R. Leigh and the author. The experimental work was shared by Dr L. Leigh, Mrs G. Garrett, Dr D.C. Weisser and the author and in the early part by Dr M. Shikazono. The data extraction was performed with available programs on the IBM 1800 computer by the author. The Optical Model and DWBA computations and other calculations were done by the author and the examination of the results were done with occasional help from Dr J.R. Leigh.

The Optical Model global search code GENOA and the full finite range DWBA code LOLA were provided by Dr R.M. DeVries and adopted to the UNIVAC 1108 computer by Dr D.C. Weisser and the author. The inelastic scattering code NUCSCAT was made available by Drs M. Samuel and U. Smilansky and ran on the IBM 360/50 computer.

Some of the work reported in this thesis has appeared in the following publication:

Differences in the Coulomb-Nuclear Interference
Patterns Produced by ^{12}C and ^{13}C ions.
J.R. Leigh, E.C. Pollacco, N. Shikazono, D.C. Weisser
and C. Garrett.
J.Phys.G:Nucl.Phys., Vol.2, No.3, 62, L39 (1976).

No part of this thesis has been submitted for a degree at any other university.

E Pollacco

E.C. POLLACCO

Acknowledgements

It is a pleasure to thank Dr Jack Leigh who has guided me during my Ph.D. course for the past three and a half years. His supervision was very valuable in my understanding of the experimental and theoretical aspects of this work.

I wish to thank Dr Jack Leigh, Mrs Claire Garrett, Dr David Weisser and Dr Moto Shikazono who participated in the collection of the data. Thanks are also due to all the technical staff of the Department of Nuclear Physics for their excellent maintenance of the experimental facilities.

I would like to acknowledge the many hours spent by Drs David Weisser, Jack Leigh and Al Zeller in correcting the drafted thesis and for making valuable suggestions. I also wish to thank Dr B. Robson for reading the draft of the theoretical chapter. I am grateful to Mr Tony Frawley for his assistance in drawing some of the diagrams and especially to Mrs Claire Garrett who photographed all the figures which appear in this work.

The award of an Australian National University Scholarship is greatfully acknowledged.

I am also indebted to my wife Sally for her great patience and encouragement over the past three years.

Finally, I would like to thank Prof. J.O. Newton for his interest in this work and for giving me the opportunity to use the excellent facilities at the Department of Nuclear Physics.

E.C. POLLACCO

TABLE OF CONTENTS

Page

CHAPTER 4 (Continued)

Abstract

Excitation functions for elastic and inelastic scattering and single neutron transfer reactions have been measured for incident energies spanning the Coulomb barrier at nominally 120° to the beam direction.

The elastic scattering data for $^{12,13}C$ on ^{48}Ca, ^{50}Ti, ^{52}Cr, ^{53}Cr and ^{54}Fe and $^{16,18}O$ on ^{52}Cr and ^{54}Fe have been analysed using the Optical Model. From the extracted optical potentials Coulomb barriers were obtained.

The inelastic scattering measurements to the first 2^+ states of ^{52}Cr and ^{54}Fe induced by ^{12}C, ^{13}C, ^{16}O and ^{18}O exhibit nuclear-Coulomb interference patterns which are remarkably different for the different projectiles. The cross-section data is reproduced by the distorted-wave Born approximation (DWBA) with a collective model form factor for nuclear excitation. From the sub-Coulomb data, B(E2) values were extracted and above the Coulomb barrier, nuclear deformation parameters $R\beta_N$ were obtained.

The single neutron transfer reactions (^{12}C,^{13}C) to the N=29 nuclei have been interpreted using full finite range (FFR) DWBA calculations. The excitation functions are generally well described by FFR-DWBA. Spectroscopic factors have been extracted from the data below the Coulomb barrier and are in agreement with values obtained from light ion work.

Chapter 1

INTRODUCTION

One of the attractive features of heavy ion induced reactions is the appropriateness of a semi-classical description. This is due to the relatively small de Broglie wavelength, $\lambdabar$ associated with the relative motion of the colliding nuclei, which is typically $\lambdabar \approx 0.2$ fm compared with some characteristic length, say, the sum of the nuclear radii ≈8 fm. Thus the wave packet describing the relative motion of two heavy ions is localised in space and leads to the concept of a well defined classical orbit (Fo59, Br72). Using this description, the many reactions that occur when two heavy ions interact can be broadly classified into three main groups. With trajectories corresponding to a large impact parameter, b (fig.1.1(a)) the nuclei are kept well separated by the centrifugal and Coulomb forces. The non-elastic reactions that can occur in this region of b are 'Coulomb excitation' (A166) and 'sub-Coulomb transfer' (Go74). For orbits with small impact parameters (fig.1.1(c)) the ions surmount the Coulomb and small centrifugal barriers resulting predominantly in compound nucleus formation. Projectiles with intermediate impact parameters have limited mass overlap and unlike the previous case the mass, charge, energy and angular momentum transferred are generally small. The reactions studied in this work are assumed to be direct and span the region between large and intermediate impact parameters. These processes are called 'Quasi-Elastic'.

Light ion induced reactions, such as (p,p'), (d,p), (^{3}He,d) and (p,t) have long been established as a powerful spectroscopic tool. From these measurements a large volume of information has been compiled on energy levels, spins and parities of nuclei throughout the periodic table.

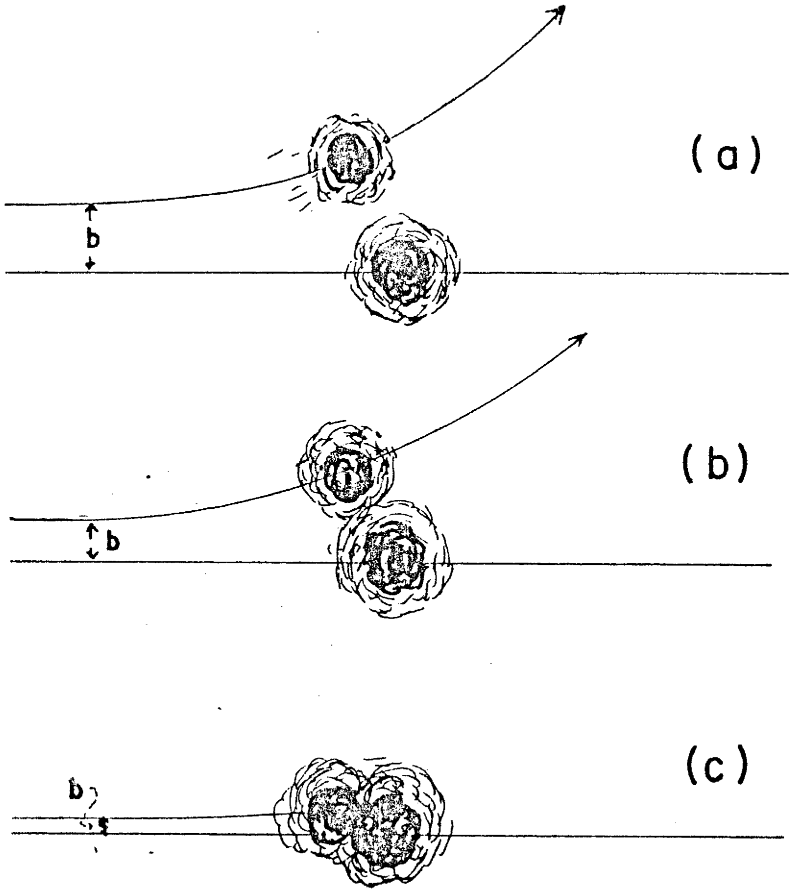

Fig.1.1

Experimental information from heavy ion induced direct reactions, however is less comprehensive. The first measurements with heavy ion beams were performed in the mid 1950s (Ch54, Re56), although relatively few direct heavy ion reactions were measured until the late 60s when adequate heavy ion accelerators and techniques for detecting heavy particles were developed. The direct reactions studied in the past eight years comprise elastic and inelastic scattering and one, two and four nucleon transfer, induced by a large range of projectiles, from Li to S. The spectroscopic information obtained from heavy ion reactions, excluding Coulomb excitation, have been mostly complementary to light ion work.

Most light ion induced reactions have been analysed, with a large measure of success, using the distorted wave Born approximation (DWBA).

Through these studies a relatively good understanding of the reaction mechanisms and mutual interactions between the colliding nuclei has been gained. Further, from single nucleon transfer reaction measurements, 'spectroscopic factors' are extracted by comparing the DWBA calculations with the data. The spectroscopic factor yields information on the magnitude of the single particle components in the wave function which describes the populated state. Hence the spectroscopic factors are a valuable test of nuclear structure model calculations. In view of this success with light ions it is therefore a natural progression to analyse the quasi-elastic heavy ion reactions with the same direct reaction theories.

The knowledge of the ion-ion effective potential is of importance since it is necessary for direct reaction calculations. The average potential is generally provided by analysing the elastic scattering data in terms of the 'optical model' (Chapter 2). Historically the optical model was formulated for nucleon-nucleus scattering by Bethe (Be35) and Fernbach *et al* (Fe49) who assumed that the nucleon-nucleus interaction is a simple two body potential. Later, Feshbach *et al* (Fe54) further developed the model to include an imaginary potential to take into account the effect of other channels absorbing flux from the elastic scattering. The introduction of the imaginary potential was necessary to predict the broad neutron scattering resonances (Fe54). Subsequently, the optical model was used to investigate the mass distribution of nuclei and dynamical effects such as target excitation and refined to study details of the nucleon-nucleus interaction (mass asymmetry, spin-orbit and tensor forces) (Si75). The applicability of the optical model to heavy ion elastic scattering is not entirely clear especially when the nuclear overlap between the ions is significant. Under these circumstances it is difficult to envisage a static potential, which is a function only of the separation of the centres of mass, as appropriate when dynamic distortions of the nuclei might be large. However, for heavy ion peripheral collisions the distortions should be small and therefore the optical model should be reliable (Sa74). Elastic scattering data induced by heavy ions is generally fitted by approximating the nuclear interaction in terms of a local, complex, Wood-Saxon potential (Gl67). Four free parameters are determined by the data or six if the geometry of the real and imaginary potentials are assumed to be different. Heavy-ion elastic scattering is generally well reproduced by the optical model. However, because of the many competing reactions, the absorption of the elastic flux becomes large once the nuclei start to overlap, therefore elastic scattering data is only sensitive to the tail of the optical potential. It has long been known that this results in large ambiguities in the choice of optical potential parameters (Ig 58). Because the average potential, to a large degree, determines whether the colliding ions will fuse or scatter elastically, or quasi-elastically, ways are being sought to reduce the potential ambiguities. Following the technique used in light ions studies (Gr68), attempts are being made to calculate the real ion-ion potential using the 'Folding model' in order to reduce some of the ambiguities. Preliminary studies using the folded potentials (Br72, Va73, Br74, Ba75) have not given full satisfactory results (Sa75).

The Coulomb barrier V_B is defined (Ob72) as the value of the potential when the sum of the Coulomb and real nuclear potentials is a maximum (fig.1.2)

$$V_B = V_c(R_B) + V_N(R_B) \qquad 1.1$$

where R_B is called the 'barrier radius'. From the optical model analysis of the elastic data the values of V_B can be calculated, which are important for heavy ion fusion mechanisms studies (Be67, Je71, Wo72).

The term 'Coulomb barrier' is however used rather loosely in this work.

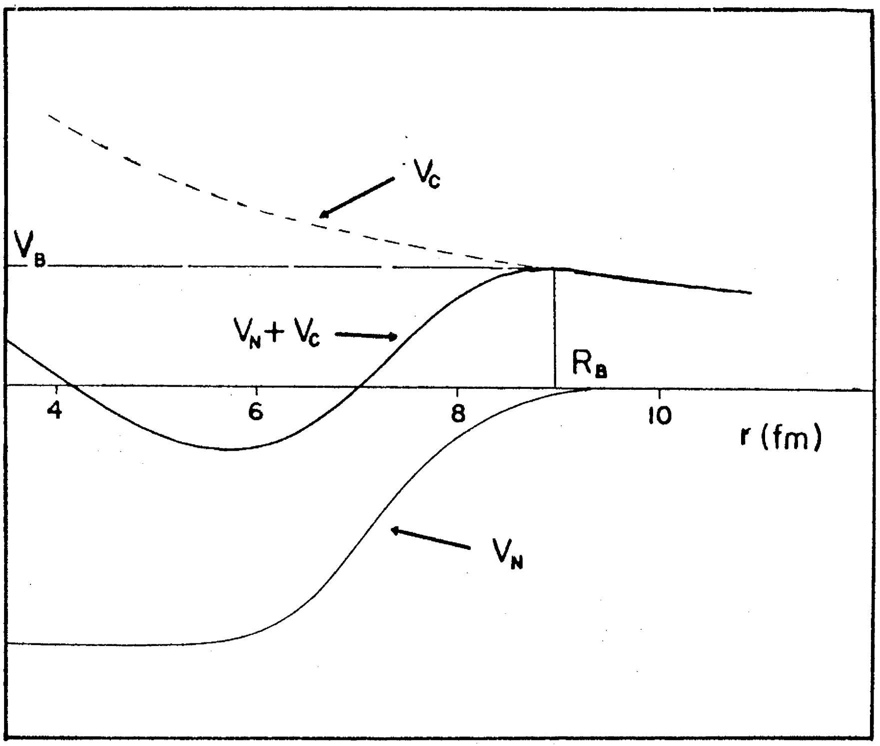

Fig.1.2

Heavy-ion inelastic scattering can be roughly divided into two incident energy regions, well below the Coulomb barrier, termed 'Coulomb excitation', and above the barrier. For low enough bombarding energies the nuclear interactions are negligibly small and the excitation of the projectile or target is only through the Coulomb force. The calculations of Coulomb excitations cross-sections are well established and use a semi-classical treatment to perform the otherwise difficult coupled channel calculations (Wi66). Since the Coulomb force is known the comparison between theory and experiment yields model independent reduced matrix elements (lifetimes) and quadrupole moments. Coulomb excitation studies have been extensive and very successful.

For incident energies around the Coulomb barrier the inelastic scattering is generally analysed using DWBA with a phenomonological collective form factor which assumes that the optical potential which describes the elastic scattering is deformed (Ba62). This model has been quite successful in reproducing the inelastic data, not only for heavy ions (Ch73), but also light ion scattering (Gs67, Ma68). The main difficulty with this model is that the deformation parameter, obtained by comparing theory with experiment is difficult to relate to intrinsic nuclear properties. However, lacking better alternatives for heavy ion scattering, this model cannot be dismissed lightly. Inelastic scattering induced by heavy ions for energies around the Coulomb barrier has generally a large cross-section, relative to transfer reactions, and has been measured for a large range of projectile-target combinations (Sa68, Re75, Be72, Gr74). The prime interest in this reaction has been the study of the 'Coulomb-nuclear interference' phenomenon in the hope of accurately determining the optical potential. The Coulomb-nuclear interference is generally manifested by a minimum in the measured angular distribution or excitation functions (Be73, Le76) when the repulsive Coulomb and attractive nuclear forces are of equal magnitude. Therefore these reactions are a formidable means of determining the strength and gradient of the tail of real nuclear potential by comparison with the Coulomb potential. Hence, some of the optical potential ambiguities are resolved (Co75, Pe73, Ch73) and the resultant potentials can then be used with increased confidence to determine spectroscopic information from heavy ion transfer reactions. It must be stressed however, that it is not entirely clear whether an optical potential which gives a good representation of the elastic and inelastic scattering data should in turn give a good fit to the corresponding transfer data (Au70, p.80).

The study of single nucleon transfer induced by heavy ions was originally motivated by Breit *et al* (Br52). Breit *et al* advocated the possibility of employing classical mechanics to describe the relative motion of the two ions. Subsequently, Breit *et al* (Br56, Br64) performed

semi-classical single nucleon transfer calculations which gave good account of experimental measurements for bombarding energies below the Coulomb barrier (Mc60, Be63). The fully quantised calculation was developed by Buttle and Goldfarb using DWBA with a zero-range approximation (Bu66). The calculations by Buttle and Goldfarb reproduce the sub-Coulomb transfer data very well and the extracted spectroscopic factors are in reasonable agreement with values obtained from light ion work (Ba71, Pa74). The attractive feature of sub-Coulomb transfer is that at these energies the ions have a large distance of closest approach and so they have negligible nuclear interaction.
Therefore the relative motion is well described by Coulomb wave functions. Hence the extracted spectroscopic factors are independent of any problem associated with the choice of the optical potential. The shapes of the angular distributions or excitation function, at these energies, are rather insensitive to the angular momentum transferred L (Bu71). Therefore, sub-Coulomb transfer reactions alone cannot be used to determine spin assignments. To extract spectroscopic factors using DWBA calculations, the configuration of the populated states must be known from other reactions. However the magnitude of the cross-section depends strongly on the magnitude of the single particle wave functions at the surface. Hence this dependence might be used to indicate what configuration might be populated.

The magnitude of the cross-section is a strong function of the Q-value of the reactions. The optimum Q-value Q_{opt} for neutron or proton transfer can be roughly estimated using classical arguments and given by (Ch73b)

$$Q_{opt} \approx E_i \left(\frac{z_f Z_f}{z_i Z_i} - 1 \right) \qquad 1.2$$

where E_i is the incident centre of mass energy, z_i and z_f are the charges of the incident (i) and outgoing (f) particles and Z_i and Z_f are the charges of the target (i) and residual (f) target. Figure 1.3 shows the dramatic variation in the cross-section with Q-value.

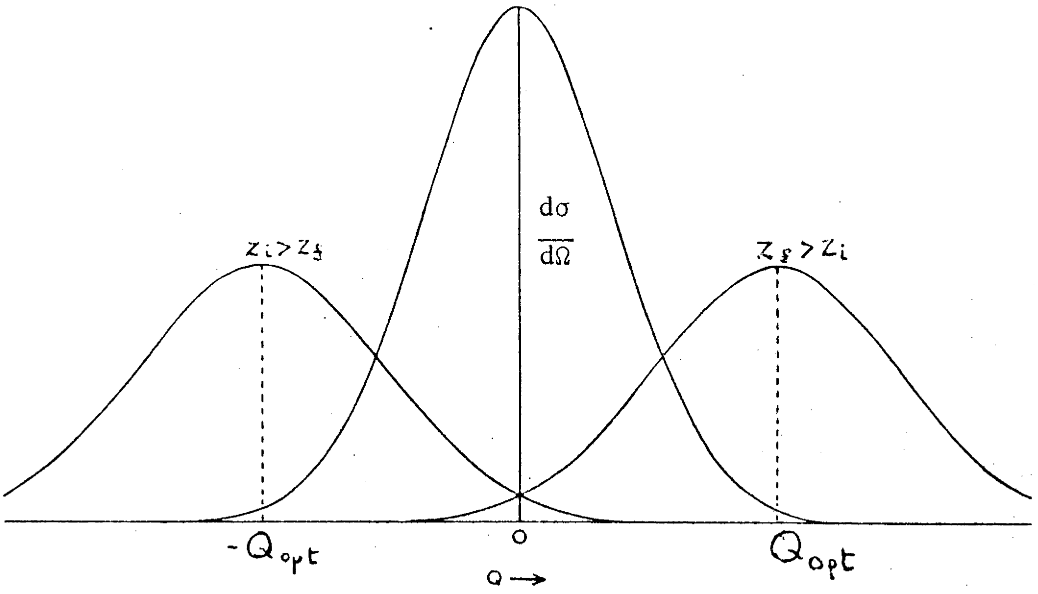

Fig.1.3 Single nucleon transfer cross-section dependence on the reaction Q-value.

At incident energies close to the Coulomb barrier the single nucleon transfer angular distributions or excitation functions have a characteristic bell shape (Ch73b). As the incident energy is increased the peak cross-section of the bell shape shifts to smaller angles in the angular distribution. For high enough bombarding energy the angular distributions exhibit structure at the peak cross-section (Bo73). In particular instances, from this structure, L and the total angular momentum j of the populated state can be determined (Sc73, Wh74). The no-recoil DWBA transfer calculations for energies above the Coulomb barrier fail to give a good description of the data and full finite range (FFR) DWBA has to be used (Ko73, De73). The extracted spectroscopic factors are generally within 20% of values obtained from light ion reactions. The shape of the angular distributions or excitation functions are generally well produced by FFR-DWBA, although in some instances discrepancies do occur, particularly for high Q-value proton transfer reactions. These discrepancies appear at extreme forward angles and also as a systematic shift between theory and experiment. In most instances the discrepancies can be removed by empirically changing the outgoing channel optical parameters (Lo74). Since this prescription is rather arbitrary it is questionable whether it is correct. Further, this disagreement might reflect something fundamentally wrong with DWBA calculations for heavy ions. Therefore for such cases it is vital to determine the optical potential accurately to assess the validity of DWBA.

The reactions studied in this work (table 1.1) are all in the form of excitation functions at nominally 120° (lab) for incident energies around the Coulomb barrier. The elastic scattering and single neutron transfer reactions induced by the carbon isotopes were measured by Parkinson (Pa74) and the experimental method used in the measurement of the other reactions are described in Chapter 3. The reactions are analysed using the optical model and DWBA as outlined in Chapter 4 and the results are discussed in Chapter 5. The purpose of this investigation is to determine if the theories employed can give satisfactory reproduction of the data with extracted spectroscopic information in agreement with values obtained from other reactions. The comparison between theory and experiment is particularly meaningful in the case of ^{13}C scattering from ^{52}Cr where data from three different reactions are measured. This represents a good test of the assumption that the optical potential which gives a good representation of the elastic and inelastic data should in turn give a good fit to the single nucleon transfer measurement. Of course this tests the individual theories at the same time. The reactions induced by ^{13}C on ^{54}Fe present a weaker test since the optical potential in the outgoing channel for the ^{54}Fe(^{13}C,^{12}C)^{55}Fe reaction cannot be obtained. Furthermore, all the reactions studied cover a domain

TABLE 1.1

Reaction	Angle (Lab)
^{48}Ca(^{12}C,^{12}C)^{48}Ca	120°, 150°
^{48}Ca(^{13}C,^{13}C)^{48}Ca	116°, 146°
^{48}Ca(^{13}C,^{12}C)^{49}Ca (GS)	120°
^{50}Ti(^{12}C,^{12}C)^{50}Ti	120°
^{50}Ti(^{13}C,^{13}C)^{50}Ti	120°
^{50}Ti(^{13}C,^{12}C)^{51}Ti (GS, 1.16 MeV, 2.37 MeV)	120°
^{52}Cr(^{12}C,^{12}C)^{52}Cr	120°
^{52}Cr(^{13}C,^{13}C)^{52}Cr	117°, 147°
^{53}Cr(^{12}C,^{12}C)^{53}Cr	120°
^{52}Cr(^{12}C,^{12}C)^{52}Cr* (1.434 MeV)	120°
^{52}Cr(^{13}C,^{13}C)^{52}Cr* (1.434 MeV)	120°
^{52}Cr(^{13}C,^{12}C)^{53}Cr (GS, 2.32 MeV, 3.71 MeV)	120°
^{53}Cr(^{12}C,^{13}C)^{52}Cr (GS)	120°
^{52}Cr(^{16}O,^{16}O)^{52}Cr* (GS, 1.434 MeV)	120°
^{52}Cr(^{18}O,^{18}O)^{52}Cr* (GS, 1.434 MeV)	120°
^{54}Fe(^{12}C,^{12}C)^{54}Fe	120°
^{54}Fe(^{13}C,^{13}C)^{54}Fe	118°, 148°
^{54}Fe(^{12}C,^{12}C)^{54}Fe* (1.409 MeV)	120°
^{54}Fe(^{13}C,^{13}C)^{54}Fe* (1.409 MeV)	120°
^{54}Fe(^{13}C,^{12}C)^{55}Fe (GS)	120°
^{54}Fe(^{16}O,^{16}O)^{54}Fe* (GS, 1.409 MeV)	120°
^{54}Fe(^{18}O,^{18}O)^{54}Fe* (GS, 1.409 MeV)	120°

All reactions are in the form of excitation functions.

of bombarding energies from below the Coulomb barrier, where the calculations are most reliable, to energies above the barrier, where the reaction mechanism might not be well understood. Therefore a comparison between theory and experiment over the whole range of energies should provide a sensitive probe as to whether the calculations can be extrapolated to high incident energies. Finally, the measurement of inelastic scattering induced by four projectiles on ^{52}Cr and ^{54}Fe targets might reveal information on the role played by the projectile in the inelastic scattering mechanism.

Chapter 2

OPTICAL MODEL AND DWBA

2.1 FOREWORD

In this chapter a review of the Optical Model and Distorted Wave Born approximation (DWBA) is given in support of the two final chapters, where analysis of the elastic, inelastic and transfer data is presented and discussed.

2.2 THE OPTICAL MODEL

To calculate the differential cross-section for elastic scattering it is necessary to know the form of the potential between the interacting complex nuclei. A microscopic treatment of the potential is exceedingly difficult; the nucleons in the target interact with nucleons in the projectile through non-local, spin-dependent and many-body forces. At present this complex problem cannot be solved. Another problem is that when two ions interact many possible reactions can occur (Ko76) and a proper treatment requires a coupled-channel calculation, which although possible is difficult to perform. An alternative approach which avoids the above difficulties is to use the Optical Model (OM). This model essentially assumes that the details of the microscopic interactions can be averaged out and can be represented by a phenomenological potential with a number of parameters, which are determined by systematically adjusting them in order to reproduce the elastic scattering data.

The OM as used in this work assumes that the ion-ion interaction is a simple, local, complex, spin-independent two-body potential V(r), where r is the distance between the centres of the two ions. The imaginary part of the potential is basic to the OM and takes into account the many open channels by absorbing flux from the incident channel. Differentiating between the channels is not necessary unless one of them is strongly coupled to the elastic channel. The exclusion of spin-dependent forces is justified because it is possible to obtain good representation of the data without them (Bi74). This does not imply that they are not important for heavy ions, it simply means that the present experiments are insensitive to these forces. Similar arguments can be put forward for not including contributions from non-local effects, density dependent and three-body forces. However it must be stressed that by using an effective potential these interactions are indirectly taken into account.

For energies above the Coulomb barrier, the dominant physical process in heavy ion reactions is the strong absorption, predominantly, into the compound nucleus formation (Ko76). This is demonstrated by the characteristic rapid fall in the elastic cross-section from Rutherford scattering (Ba75, Wi75, Re75) and occurs when the two ions have only limited inter-nuclear overlap (Sa74, Ba75). This implies that the reactions which can be observed experimentally are predominantly surface reactions and sample *only* the tail of the effective potential V(r). This also implies that the phenomenological optical potential is not without physical basis since the assumptions made in the OM become increasingly better for limited nuclear overlap (Ja76).

The elastic scattering cross-sections for a given effective potential V(r) are obtained by solving the Schrödinger equation, describing the relative motion of the projectile and target. The method of solving this differential equation and expressions for the differential cross-section are given elsewhere (Ro67, Ho66).

2.3 THE OPTICAL POTENTIAL

The average potential $\tilde{V}(r)^{(*)}$ between two heavy ions is written as the sum of the Coulomb $\tilde{V}_c(r)$ and nuclear $\tilde{V}_N(r)$ potentials. In the two following sections the functional form of $\tilde{V}_c$ and $\tilde{V}_n$ are discussed.

2.3.1 Coulomb Potential $\tilde{V}_c(r)$

In the optical model and DWBA calculations an approximate $\tilde{V}_c(r)$ is used. The target is assumed to have a uniform charge (Ho71) distribution of radius R_c (fig.2.1), while the projectile is described by a point charge.

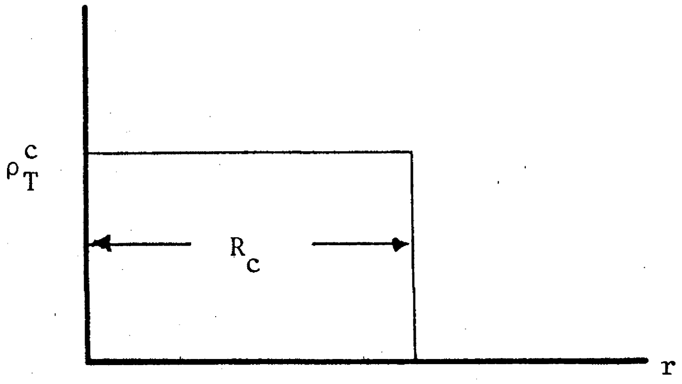

Fig.2.1

To take into account the finite size of the incident particle the Coulomb radius R_c is extended from $r_{oc}A_T^{\frac{1}{3}}$ to $r_{oc}(A_T^{\frac{1}{3}}+A_P^{\frac{1}{3}})$ where A_T and A_P are the target and projectile mass numbers and r_{oc} is the Coulomb radius parameter. The Coulomb potential using the above assumptions is given by

---

(*)The ~ denotes effective potential.

$$\tilde{V}_c(r) = \frac{Z_T Z_P e^2}{r}, \qquad r \geqslant R_c \tag{2.1a}$$

$$= \frac{Z_T Z_P e^2}{2R_c}\left[3-(\frac{r}{R_c})^2\right], \quad r < R_c \tag{2.1b}$$

$Z_T e$, $Z_P e$ are the atomic numbers of the target and projectile respectively.

The criticism of this prescription is evident: an unrealistic target charge distribution is assumed and the finite size and shape of the projectile is not explicitly taken into account. Since the Coulomb potential plays a crucial role in all the calculations it is important to examine the validity of above assumptions.

A more realistic form for the electrostatic potential is given by (Va74)

$$\tilde{V}_c^F(r) = Z_P Z_T e^2 \iint d^3r_P \, d^3r_T \, \frac{\rho_T^c(r_T)\,\rho_P^c(r_P)}{|\underline{r}_T - \underline{r} - \underline{r}_P|} \tag{2.2}$$

where ρ_T^c and ρ_P^c are the charge density distributions of the target and projectile respectively and are assumed to be spherically symmetric.

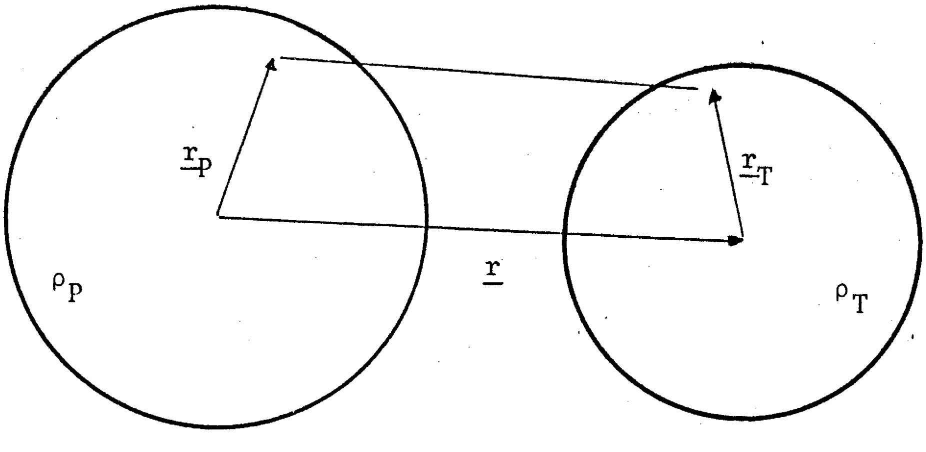

Fig.2.2

The co-ordinates are shown in fig.2.2. $\tilde{V}_c^F(r)$ takes into account most of the deficiencies present in $\tilde{V}_c(r)$, however it does assume that charge distributions do not change with decreasing r.

Equation 2.2 was evaluated for $^{12}C+^{52}Cr$ with ρ_T^c and ρ_P^c extracted from published electron scattering data using a modified harmonic oscillator shape for ^{12}C (K173)

$$\rho_P^c(r) \quad = \quad \rho_{oP}^c(1+\alpha(\frac{r}{\beta})^2)\exp(-(\frac{r}{\beta})^2) \qquad 2.3$$

(α=1.15, β=1.67 fm) and for ^{52}Cr a Wood-Saxon distribution was used (Be64)

$$\rho_T^c(r) \quad = \quad \rho_{oT}^c(1+\exp(\frac{r-R_T^c}{a}))^{-1} \qquad 2.4$$

(R_T^c=3.91 fm, a=0.53 fm). The volume integrals of (2.3) and (2.4) were normalised to unity.

The result of this calculation shows (fig.2.3) that $\tilde{V}_c^F$ and $\tilde{V}_c$ agree to within 0.1% for values of r larger than R_c=7.2 fm (r_{oc}=1.2 fm). Heavy ions at Coulomb barrier energies do not come within r smaller than R_c (Sa74, Mo76), therefore $\tilde{V}_c$ (2.1) is a good approximation. This agreement was not unexpected since the Coulomb potential is of such a long range. The large discrepancy between $\tilde{V}_c^F$ and $\tilde{V}_c$ at small values of r is not meaningful since equation (2.2) is not valid where dynamic effects are severe (My74).

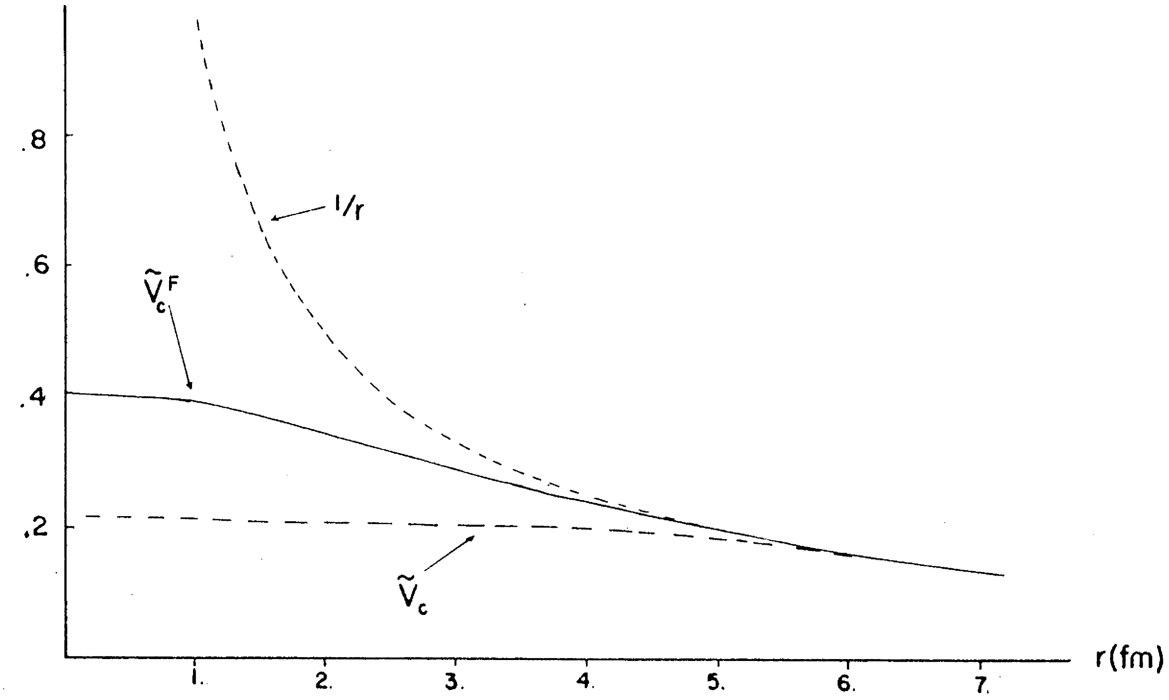

Fig.2.3 Coulomb potentials $\tilde{V}_c$ (2.1) and $\tilde{V}_c^F$ (2.2) as a function of r ($Z_P Z_T e^2 = 1$).

2.3.2 Nuclear Potential $\tilde{V}_N(r)$

The complex nuclear potential $\tilde{V}_N$ used in all the OM and DWBA calculations had the conventional Wood-Saxon form:

$$V_N(r) = V_o(1+\exp(\frac{r-R}{a}))^{-1} + i\, W_o(1+\exp(\frac{r-R'}{a'}))^{-1} \qquad 2.5$$

where $R = r_o(A_T^{\frac{1}{3}}+A_P^{\frac{1}{3}})$ -

$R' = r_o'(A_T^{\frac{1}{3}}+A_P^{\frac{1}{3}})$

r_o, r_o' are the real and imaginary radius parameters

a, a' are the real and imaginary diffuseness parameters

V_o, W_o are the real and imaginary potential depths.

This form of potential is chosen because it is simple to compute and has been shown to give good fits to a wide range of elastic data (Wi75, Ba75, Re75, Zi75). However, as in light-ion work, many optical parameter sets can be found which give equivalent fits to the data. Indeed with heavy ions the ambiguities are not only discrete but in many cases continuous (Ig59). In an effort to reduce or eliminate the ambiguities in the real part of $\tilde{V}_N$, attempts have been made to calculate the nucleus-nucleus potential with a 'microscopic' approach using the 'Folding model' (Sa74, Ei71, Va73).

The folding model assumes that the mass distributions are unperturbed when overlap occurs and that the real potential is calculated by convoluting the densities with an effective nucleon-nucleon interaction v, i.e.

$$\tilde{V}_N^F(r) = \int d^3r_T d^3r_P \; \rho_T(r_T) v(|\underline{r}_T-\underline{r}-\underline{r}_P|)\rho_P(r_P) \qquad 2.6$$

where ρ_P and ρ_T are spherically symmetric mass distributions of the projectile and target and the co-ordinates are shown in fig.2.2. This description is expected to be fairly accurate for elastic or quasi-elastic processes since exchange, dynamic and other effects should theoretically be small (Br74b, Ja76) for restricted density overlap (fig.2.4).

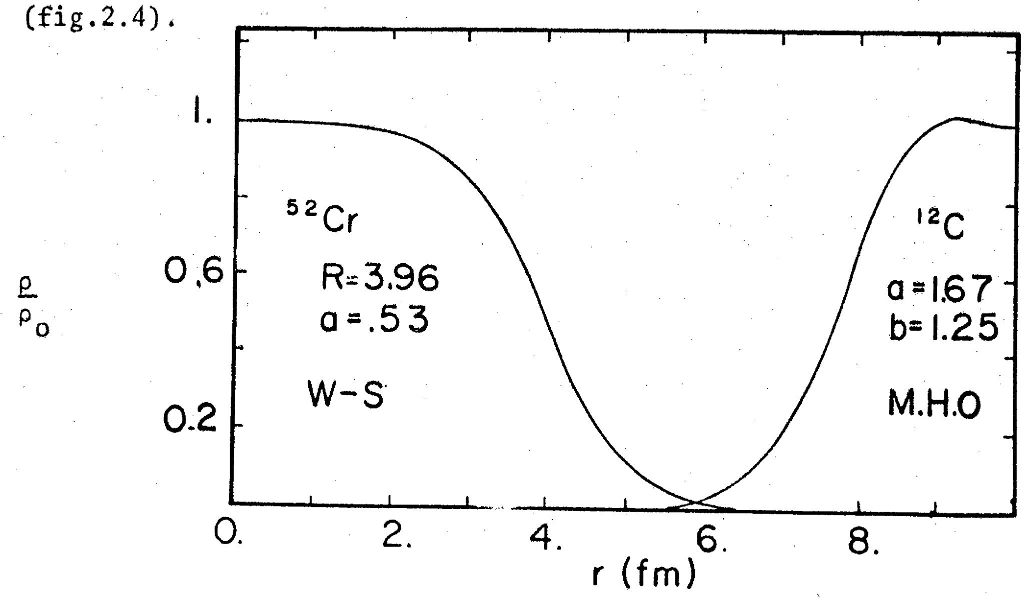

Fig.2.4 Charge distributions (De74) along the line of centres for separation 10 fm.

Elastic scattering data have been analysed using expression (2.6) with several forms of v (gaussian, Yukawa, zero-range) each giving reasonable results. The main discrepency is that a normalisation of $\tilde{V}_N^F$ by approximately one half is necessary to fit the data (Sa75), which indicates that an important effect in the calculation is being neglected. The imaginary potential is not predicted by the model and is generally assumed to be of the same form as $\tilde{V}_N^F$ with adjustable strength (Ba75).

The mass distributions are generally assumed to be the same as the charge distributions obtained from electron scattering studies.

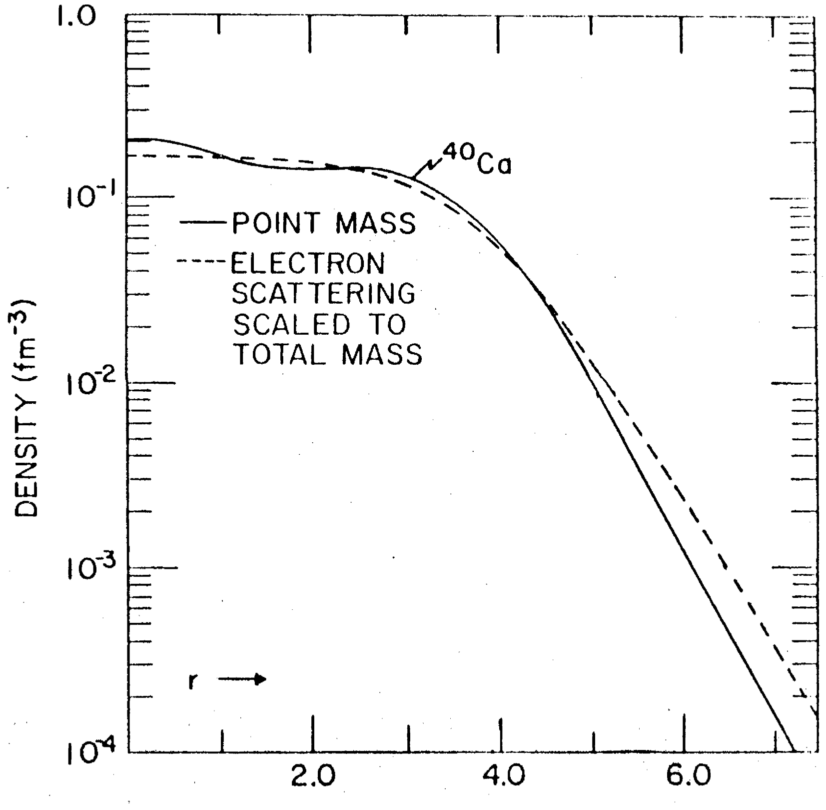

Fig. Mass distribution (2.7) and charge distribution for ^{40}Ca. Figure copied from reference (Va74).

However it is generally the case that electron scattering experiments are not sensitive enough to determine the tail of the distribution (Va74) (see fig. above). So in the more sophisticated calculations

(Do76) the ρ's have been obtained by using shell model wave functions $\phi_i(r)$.

$$\rho(r) = \sum_i W_i |\phi_i(r)|^2 \qquad 2.7$$

where i runs over occupied neutron and proton bound states and W_i is the statistical weight.

The choice of nucleon-nucleon interaction v to be used is not clear (Sa75) since different authors have used a variety of potentials with the same measure of success, thus in most cases the elastic data cannot discriminate between them (Ba75). However discounting the uncertainty in the choice of v, the use of the folding model reduces the number of free parameters to two, if the imaginary potential is assumed to have the same shape as the real part. Hence the number of ambiguities are greatly reduced.

An interesting result from folding calculations is that for large values of r, $\tilde{V}_N^F$ has the same exponential fall off as a Wood-Saxon potential (fig.2.5). Because heavy ion scattering is only sensitive to the tail of the potential this result makes the use of Wood-Saxon potentials less *ad hoc*.

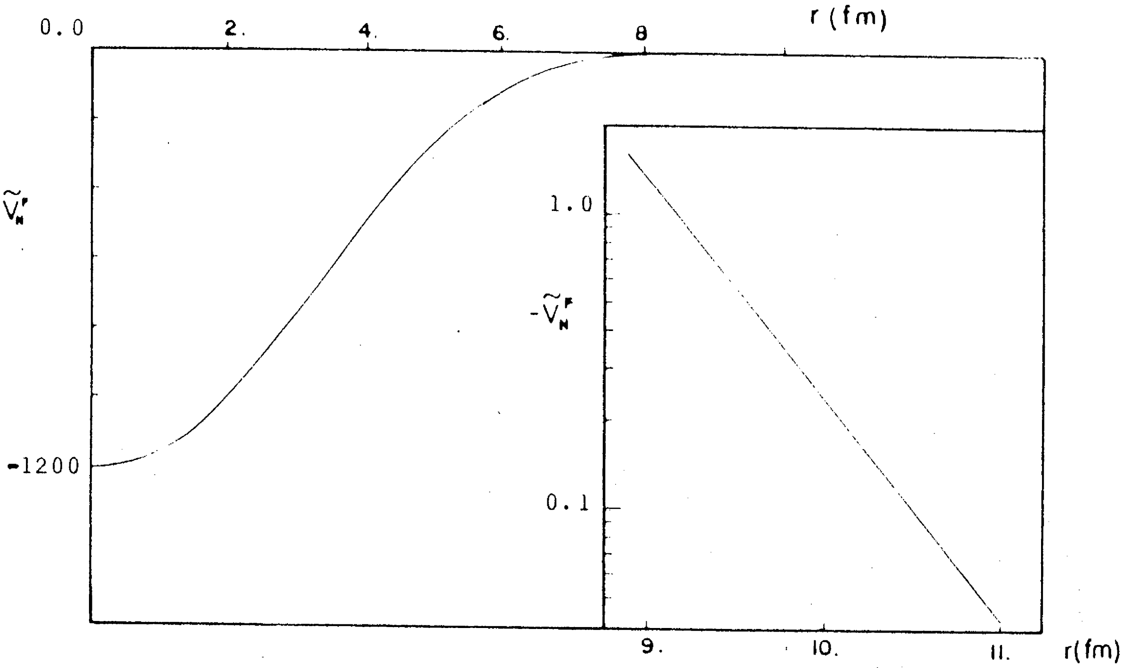

Fig.2.5 Folded potential for ^{54}Fe + ^{16}O using a δ-function for v and mass distributions assumed to have the same shape as electron scattering measurements (De74) ($\int\rho_{P(T)}d\tau = A_{P(T)}$).

2.4 THE DISTORTED-WAVE BORN APPROXIMATION

The experimentally measured inelastic and single neutron transfer reactions which are analysed in this work are assumed to be direct, single-step processes. Such a reaction mechanism is well described by the distorted-wave Born approximation, if the cross-section is weak relative to the corresponding elastic channel.

2.4.1 Mathematical Formalism

Consider the reaction A+a → B+b, where a and b are not necessarily different. The Hamiltonian H for this system is written:

$$H = H_\alpha + V_\alpha + K_\alpha = (H_A + H_a) + V_\alpha + K_\alpha \qquad 2.8a$$

or equivalently

$$H = H_\beta+V_\beta+K_\beta = (H_B+H_b)+V_\beta+K_\beta \qquad 2.8b$$

where $\alpha(a,A)$ and $\beta(b,B)$ denote the incident and outgoing channels respectively. $K_\alpha(K_\beta)$ and $V_\alpha(V_\beta)$ are the relative kinetic and potential energies between the two composite particles in channel $\alpha(\beta)$. H_A, H_a, H_B and H_b are the Hamiltonians describing the internal motion in each of the nuclei. The eigenfunctions for H_α can be written as

$$H_\alpha\phi_\alpha(\xi_\alpha) = (H_A+H_a)\phi_A(\xi_A)\phi_a(\xi_a) = E_\alpha\phi_\alpha(\xi_\alpha) \qquad 2.9$$

where E_α is the total energy of internal motion and $\xi_\alpha=(\xi_A,\xi_a)$ are the internal co-ordinates. The total energy E is then given by

$$E = E_\alpha+\hbar^2k^2_\alpha/2\mu_\alpha \qquad 2.10$$

where $\underline{k}_\alpha$ is the wave number and μ_α the reduced mass. Similar equations as (2.9, 2.10) are written for channel β.

The exact transition amplitude $T_{\alpha\beta}$ for transferring from channel α to β can be derived from formal scattering theory and given by (Au70)

$$T_{\alpha\beta} = <\phi_\beta(\xi_\beta)e^{i\underline{k}_\beta\cdot\underline{r}_\beta}|V_\beta|\Psi^{(+)}_\alpha> \qquad 2.11a$$

or alternatively

$$T_{\alpha\beta} = <\Psi^{(-)}_\beta|V_\alpha|\phi_\alpha(\xi_\alpha)e^{i\underline{k}_\alpha\cdot\underline{r}_\alpha}> \qquad 2.11b$$

Equation (2.11a) is known as the Post representation of the exact amplitude while (2.11b) is called the Prior representation. Both forms are equivalent (Me62). $\Psi^{(+)}_\alpha$ and $\Psi^{(-)}_\beta$ are the exact stationary solutions of the Hamiltonian (2.8). '+' ('-') denotes incoming plane (outgoing spherical) waves in channel $\alpha(\beta)$ and outgoing spherical (incoming plane) waves in all permissible channels $\beta(\alpha)$, i.e.

$$\Psi_{\alpha}^{(+)} = \phi_{\alpha}(\xi_{\alpha}) e^{i\underline{k}_{\alpha}\cdot\underline{r}_{\alpha}} + \sum_{\{\beta\}} f_{\alpha\beta}(\underline{k}_{\alpha},\underline{k}_{\beta}) \frac{e^{ik_{\beta}r_{\beta}}}{r_{\beta}} \qquad 2.12$$

where $\underline{r}_{\alpha}$ and $\underline{r}_{\beta}$ are the channel co-ordinates and $f_{\alpha\beta}$ is related to the differential cross-section by (Me62)

$$\frac{d\sigma_{\alpha\to\beta}}{d\Omega} = \frac{k_{\beta}}{k_{\alpha}}\frac{\mu_{\alpha}}{\mu_{\beta}} |f_{\alpha\beta}(\underline{k}_{\alpha},\underline{k}_{\beta})|^2$$

or

$$= \frac{\mu_{\alpha}\mu_{\beta}}{(2\pi\hbar^2)^2} \cdot \frac{k_{\beta}}{k_{\alpha}} |T_{\alpha\beta}|^2 \qquad 2.13$$

A minor modification to the Hamiltonian H is required to render the numerical calculation of (2.13) possible.

$$H = H-\tilde{V}_{\alpha}+\tilde{V}_{\alpha} \qquad 2.14a$$

$$H = H-\tilde{V}_{\beta}+\tilde{V}_{\beta} \qquad 2.14b$$

The choice of the function $\tilde{V}_{\beta}$ $(\tilde{V}_{\alpha})$ is arbitrary and in anticipation it is the optical potential in the outgoing (incident) channel. Replacing V_{β} by $V_{\beta}-\tilde{V}_{\beta}+\tilde{V}_{\beta}$ in (2.11a) and using Gell-mann Goldberg transformation (Me62), $T_{\alpha\beta}$ becomes

$$T_{\alpha\beta} = \langle\phi_{\beta}\chi_{\beta}^{(-)}|V_{\beta}-\tilde{V}_{\beta}|\Psi_{\alpha}^{(+)}\rangle + \langle\phi_{\beta}\chi_{\beta}^{(-)}|\tilde{V}_{\beta}|\phi_{\alpha}e^{i\underline{k}_{\alpha}\cdot\underline{r}_{\alpha}}\rangle \qquad 2.15$$

where the χ's are the solutions of the Schrödinger's equation:

$$(K_{\beta}+\tilde{V}_{\beta})\chi_{\beta}(\underline{k}_{\beta},\underline{r}_{\beta}) = (E-E_{\beta})\chi_{\beta}(\underline{k}_{\beta},\underline{r}_{\beta}) \qquad 2.16$$

Again '+' and '-' denote the asympotic boundary conditions:

$$\chi^{(+)}(\underline{k},\underline{r}) = e^{i\underline{k}.\underline{r}} + \text{outgoing spherical waves} \qquad 2.17$$

and $$\chi^{(+)}(\underline{k},\underline{r})^* = \chi^{(-)}(-\underline{k},\underline{r}) \qquad 2.18$$

where (*) denotes the complex conjugate. The χ's are called 'Distorted waves' and describe the relative motion of the ions in the potential $\tilde{V}_\beta$ or $\tilde{V}_\alpha$.

The second term in (2.15) is normally considered to be equal to zero for $\alpha \neq \beta$. This is indeed true for inelastic scattering since ϕ_α and ϕ_β are orthogonal. However for a rearrangement collision the orthogonality is no longer valid since ϕ_α and ϕ_β are solutions to different Hamiltonians, H_α and H_β (2.8). This problem was resolved by H.L. Goldberg and K.H. Watson (Go64) who pointed out that wave packets located at asymptotically large values of $\underline{r}_\alpha$ and $\underline{r}_\beta$ are necessarily non-overlapping and hence orthogonal.

By substituting $\phi_\alpha(\xi_\alpha)\chi_\alpha^{(+)}(\underline{k}_\alpha,\underline{r}_\alpha)$ for $\Psi^{(+)}$ in (2.15), the transition amplitude in the Born approximation $T^B_{\alpha\beta}$ is obtained.

$$T_{\alpha\beta} \simeq T^B_{\alpha\beta} = \langle\phi_\beta\chi_\beta^{(-)}(\underline{k}_\beta,\underline{r}_\beta)|V_\beta-\tilde{V}_\beta|\phi_\alpha\chi_\alpha^{(+)}(\underline{k}_\alpha,\underline{r}_\alpha)\rangle \qquad 2.20$$

where $\chi_\alpha^{(+)}$ is calculated with an optical potential $\tilde{V}_\alpha$ which gives a good description of the elastic scattering in the incident channel. This approximation is justified if $\phi_\alpha\chi_\alpha^{(+)}$ and $\psi_\alpha^{(+)}$ differ very little in the field of $V_\beta-\tilde{V}_\beta$. Therefore V_β is no longer arbitrary and choosen so $|V_\beta-\tilde{V}_\beta|$ is small. $\tilde{V}_\beta$ is set to the optical potential which describes the elastic scattering in channel β. Similarly, $T^B_{\alpha\beta}$ in the prior representation implies $|V_\alpha-\tilde{V}_\alpha|$ must be a small perturbation to V_α. Thus for the Born approximation to hold the elastic cross-sections in both the incident and outgoing channels must be large compared to the inelastic or transfer cross-sections.

Expressing $T^{B}_{\alpha\beta}$ in integral form over the relative co-ordinates $\underline{r}_{\alpha}$ and $\underline{r}_{\beta}$ gives:

$$T^{B}_{\alpha\beta} = \int d^3r_{\alpha} d^3r_{\beta}\; \chi^{(-)*}_{\beta}(\underline{k}_{\beta},\underline{r}_{\beta}) \langle bB|V_{\beta}-\tilde{V}_{\beta}|aA\rangle \chi^{(+)}_{\alpha}(\underline{k}_{\alpha},\underline{r}_{\alpha}) \qquad 2.20b$$

where the 'nuclear matrix element' t_N is given by

$$t_N = \langle bB|V_{\beta}-\tilde{V}_{\beta}|aA\rangle = \int d\xi_A d\xi_a d\xi_B d\xi_b\; \phi^{*}_{B}(\xi_B)\phi^{*}_{b}(\xi_b)(V_{\beta}-\tilde{V}_{\beta})\phi_A(\xi_A)\phi_a(\xi_a) \qquad 2.20c$$

The integration (2.20c) is done over those co-ordinates independent of $\underline{r}_{\alpha}$ and $\underline{r}_{\beta}$, hence generally the nuclear amplitude depends only on the channel co-ordinates, whilst t_N contains all the information on the nuclear structure and angular momentum selection rules. Also since t_N factors out from (2.20b) the calculation and extraction of the spectroscopic information is generally easy to perform.

To summarise, the calculations of the transition amplitude in the Born approximation assumes that the relative motion of the colliding pair is assumed to be determined by the optical potential $\tilde{V}_{\alpha}$ which describes the elastic scattering in that channel. The interaction V_{β} (or V_{α}) gives rise to a single-step transition from the initial state (defined by H_{α}) to the final state (defined by H_{β}) of the system. The outgoing particles move in the optical potential $\tilde{V}_{\beta}$ defined by the elastic scattering in the outgoing channel. The necessary conditions which must be fulfilled for DWBA to be applicable are that the reaction must be direct, one-step process, with the elastic channels being much stronger than any other channel.

2.5 INELASTIC SCATTERING

When two ions interact a non-elastic process can occur in which some of the relative energy and angular momentum is transferred to one of the nuclei. This is known as inelastic scattering, and denoted by A(a,a)A* for target A excitation.

To simplify the calculation of the transition amplitude for inelastic scattering it is assumed that the potential contains no exchange terms and no spin dependent components. The first assumption implies that the displacement variables $\underline{r}_\alpha$ and $\underline{r}_\beta$ are equal, thus the six dimension integral of $T^B_{\alpha\beta}$ (2.20) is reduced to three dimensions (Au70). From the second assumption the internal wave functions for the projectile have identical spin components (no spin flip) and are therefore orthogonal. So the reduced nuclear amplitude becomes simply $<J_BM_B|V_\beta-\tilde{V}_\beta|J_AM_A>$ where (J_AM_A) and (J_BM_B) are the angular momentum and projection of the target before and after excitation. Thus the generalised transition amplitude (2.20) reduces to

$$T^B_{\alpha\beta}\ (\text{inel}) = \int d^3r\chi^{(-)}_\beta{}^*(\underline{k}_\beta,\underline{r})<J_BM_B|V_\beta-\tilde{V}_\beta|J_AM_A>\chi^{(+)}_\alpha(\underline{k}_\alpha,\underline{r}) \qquad 2.21$$

Another simplifying assumption which is made is to ignore any difference between the optical potentials $\tilde{V}_\alpha$ and $\tilde{V}_\beta$ and $\tilde{V}_\beta = \tilde{V}_\alpha = \tilde{V}$ is solely determined from the incident elastic scattering channel.

To evaluate the transition amplitude (2.21) the interaction $V(\underline{r},\alpha)$, where α represents an operator acting on the internal co-ordinates of the target, is expanded into multipoles (Ba62)

$$V(\underline{r},\alpha) = \sum_{\ell,m} V_{\ell m}(r,\alpha)(i^\ell Y_{\ell m}(\hat{r}))^* \qquad 2.22a$$

and

$$V_{\ell m}(r,\alpha) \quad = i^{\ell}\int V(\underline{r},\alpha)Y_{\ell m}(\hat{r})d\Omega \qquad 2.22b$$

Further, the reduced matrix elements $<J_B||V_\ell||J_A>$ of $V(\underline{r},\alpha)$ are obtained by expanding (2.22a) into multipoles using Wigner-Ekart theorem (Me62)

$$<J_BM_B|V|J_AM_A> \quad = \quad \sum_\ell <J_A\ell,M_A,m|J_BM_B><J_B||V_\ell||J_A>\left[i^\ell Y_{\ell m}(\hat{r})\right]^* \quad 2.23$$

where $m=M_B-M_A$. The ℓ^{th} moment of the expansion corresponds to the angular momentum transfer ℓ to the target. From the Clebsch-Gordan coefficient $<J_B\ell,M_A,m|J_BM_B>$, ℓ is confined to

$$|J_A-J_B| \leqslant \ell \leqslant J_A+J_B \qquad 2.24$$

and the spherical harmonic $Y_{\ell m}$ determines the change in parity $(-1)^\ell$ The reduced matrix elements are only a function of the radius r and for convenience are expressed as a product of a 'form factor' $F_\ell(r)$ and the 'strength' A_ℓ, which contains all the spectroscopic information.

$$<J_B||V_\ell||J_A> \quad = \quad A_\ell F_\ell(r) \qquad 2.25$$

Inserting (2.23) in (2.21) and in (2.13) and making use of the properties of Clebsch-Gordan coefficients, the cross section for exciting the target nucleus is given by

$$\frac{d\sigma}{d\Omega} \quad = \quad \left(\frac{\mu_\alpha}{2\pi\hbar^2}\right)^2 \frac{k_\beta}{k_\alpha} \sum_\ell A_\ell^2 \sum_m |\beta^{\ell m}|^2 \qquad 2.26a$$

where $$(2\ell+1)^{\frac{1}{2}}\, i^\ell\, \beta^{\ell m} \quad = \quad \int d^3r\chi_\beta^{(-)*}(\underline{k}_\alpha,\underline{r})F_\ell(r)Y_{\ell m}^*(\hat{r})\chi_\alpha^{(+)}(\underline{k}_\beta,\underline{r}) \qquad 2.26b$$

To evaluate (2.26b) for a given form factor $F_\ell(r)$, the distorted waves, χ's are expanded in partial waves. This procedure is standard (Ba62) and will not be given here.

2.5.1 The Inelastic Form Factor

Unlike light ion inelastic scattering (Ma75), there is at present no successful microscopic calculation of the inelastic form factor for heavy ions. Therefore, in this work a phenomenological form factor is used. This is derived by assuming that the target nucleus is described by collective model wave functions interacting via an effective non-spherical potential (Bo53). The main difficulty with such a description is to relate the parameters used in this model to other nuclear properties. On the other hand the phenomenological picture has been largely successful in interpreting a large variety of heavy ion inelastic data (Ch73, Re75, Br74, Co76).

The phenomonological approach is an extension of the optical model. The deformed potential $V(\underline{r},\alpha)$, representing the interaction between the projectile and target, is derived by introducing a dynamic variable or deformation in the Coulomb and optical potentials. This is normally achieved by replacing the usual radius parameter $R = R_P+R_T$ (2.5) by

$$\mathcal{R} = R_P+R_T(1+\sum_{\ell m}\alpha^*_{\ell m}\ Y^*_{\ell m}(\hat{r})) \qquad 2.27$$

where R_P and R_T are the projectile and target radii respectively and $\alpha=(\alpha_{\ell m})$ are operators which create the excitation in the target.

The following discussion of the form factor will be devoted to excitation of pure vibrational states from the ground state of even-even nuclei. Thus the eigenfunctions of the collective Hamiltonian can be expressed in terms of quadrupole creation operators a^{*L}_M acting on the ground state vacuum $|00\rangle$. The first 2^+ state with z-projection

M is then given by (L=2)

$$a^{2*}_{M}|00\rangle = |2M\rangle \qquad 2.28$$

and the operators $(\alpha_{\ell m})$ create or annihilate vibrational phonons with angular momentum ℓ and z-projection m

$$\alpha^*_{\ell m} = \left(\frac{\hbar w_\ell}{2C_\ell}\right)^{\frac{1}{2}} (a^{\ell *}_{m} + (-)^m a^{\ell}_{-m}) \qquad 2.29$$

$\hbar w_\ell$ is the energy of the phonon and C_ℓ is the restoring force (Ba62).

$F_\ell(r)$ is made up of the sum of the nuclear and Coulomb form factors and in the next two sections these will be discussed.

2.5.2 Nuclear Form Factor $F^N_\ell(r)$

Assuming that the strength of the nuclear potential V_N depends only on the distance $r-\mathcal{R}$ from the surface (Be62), then expanding the dynamically deformed nuclear potential $V_N(r-\mathcal{R})$ in a Taylor series about R gives

$$V_N(r-\mathcal{R}) = V_N(r-R) + \sum_{n=1}^{\infty} \frac{(-1)^n}{n!} \frac{d^n V_N}{dR_T^n} (r-R_o)\ \Delta R^n \qquad 2.30$$

where $$\Delta R = R_T \sum_{\ell m} \alpha^*_{\ell m}\ Y^*_{\ell m}(\hat{r}) \qquad 2.31$$

(Since the deformation is dynamic, (2.30) and (2.31) are referring to the space fixed axis.) $V_N(r-R)$ is the spherically symmetric optical potential and in the usual notation is given by $\tilde{V}_N$. The second term in the sum (2.30) (n=1) contributes to transitions from the ground state of the target to the lowest adjacent vibration state of order ℓ, and is the only one retained in this treatment. The second and higher order terms in α, can couple the ground state to higher collective states which introduce changes in the elastic scattering and hence in the first order contribution. These corrections are assumed to be small and they cannot be treated consistently in DWBA, for terms of comparable order and equal importance have been neglected in the DW (Au70). When such terms become important a couple channel calculation has to be performed.

Thus the matrix elements are given by

$$<J_M|V_N-\tilde{V}_N|00> \;=\; <JM|-R_T\sum_{\ell m}\alpha^*_{\ell m}Y^*{}_{m}(\hat{r})\frac{d\tilde{V}_N}{dR}(r)|00>$$

$$= R_T\,\frac{d\tilde{V}_N(r)}{dR}\sum_{\ell m}\;Y^*_{\ell m}(\hat{r})\;<JM|\alpha^*_{\ell m}|00> \qquad 2.32$$

where the r dependence factors out. Comparing (2.32) with (2.23) for $J_B=J=\ell$, $J_A=0$ and m=M gives

$$<J||V_\ell||0> \;=\; -i^\ell\,R_T\frac{d\tilde{V}(r)}{dR}\;<JM|\alpha^*_{\ell m}|00> \qquad 2.33$$

It is customary (Ba62, Ho71) to introduce the root mean square deformation, β_ℓ of the ground state due to zero-point oscillation, where

$$\beta_\ell \;=\; \sqrt{<\Sigma|\alpha_{\ell m}|^2>} \qquad 2.34$$

which from (2.29) is equal to $((2\ell+1)\hbar w_\ell/2C_\ell)^{\frac{1}{2}}$. Hence the strength and form factor (2.25) in the collective model are given by

$$A^N_\ell \;=\; \frac{-i^\ell}{(2\ell+1)^{\frac{1}{2}}}\,\beta_\ell \qquad 2.35a$$

and $$F^N_\ell(r) \;=\; R_T\,\frac{d\tilde{V}_N(r)}{dR} \qquad 2.35b$$

The derived form factor for rotational excitation of a deformed axially symmetric even-even nucleus is identical to 2.35 (Be62), hence rotational states cannot be distinguished from vibrational states by an appropriate choice of form factor.

The salient feature of this result (2.35) is that there is only one free parameter β_ℓ. This can be determined very easily in most instances, since A_ℓ^N factors out from the cross-section expression (2.26a). All the other parameters are related to $\tilde{V}_N$ and extracted from the OM analysis of the corresponding elastic scattering. It is however important to note that F_ℓ^N, unlike that for Coulomb excitation (2.5.2) has no explicit ℓ dependence.

The real part of the nuclear form factor can also be derived for a folded potential (2.6) by deforming the target mass distribution $\rho_T(r_T-R_T)$, i.e. replacing R_T by $R_T(1+\sum_{\ell m} \alpha_{\ell m}^* Y_{\ell m}^*(\hat{r}))$. By expanding ρ_T in a Taylor series about R_T up to first order in α,

$$\rho(r_T-R_T) - R_T \frac{d\rho_T}{dR_T}(r_T-R_T) \sum_{\ell m} \alpha_{\ell m}^* Y_{\ell m}^*(\hat{r}) \qquad 2.36$$

inserting in (2.6) and forming the matrix elements with the non-spherical part of the resultant potential, the expression for $F_\ell^{FOLD}(r)$ is obtained

$$F_\ell^{FOLD} = U_o R_T \int_o^\infty dr_T \frac{d\rho_T(r_T)}{dR_T} r_T^2 \int_{-1}^{1} d\mu P_\ell(\mu) \rho_P((r^2+r_T^2-2r_T r\mu)^{\frac{1}{2}}) \qquad 2.37$$

A_ℓ^N is still given by 2.35a and P_ℓ are Legendre polynomials. In the above expression a δ-function nucleon-nucleon interaction v with adjustable strength U_o is used. Computing (2.37) with parameters for ρ_T and ρ_P from electron scattering measurements (De74), shows that F_ℓ^{FOLD} has an explicit ℓ dependence, (fig.2.7), unlike 2.35a. Also for a Wood-Saxon potential with choice of parameters such that $\tilde{V}_N(r) = \tilde{V}_N^F(r)$ for r between 9 to 11 fm, 2.35b and 2.37 differ only in magnitude (fig.2.6). These two results still hold when using a finite range nucleon-nucleon potential v (Mo75).

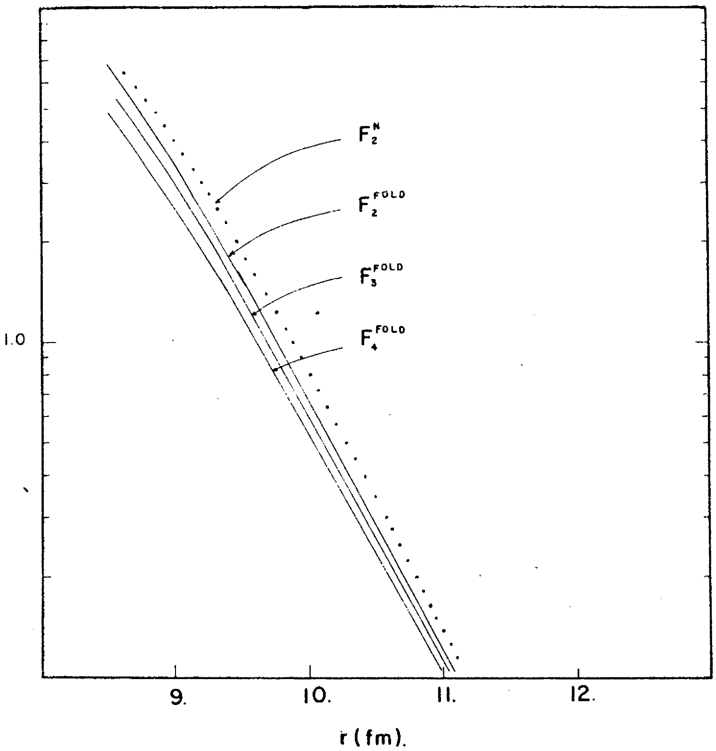

Fig.2.6 $\mathbb{R}e\ F_\ell^{FOLD}$ for $\ell = 2, 3, 4$ and $\mathbb{R}e\ F_2^N$ as a function of r.

It is important to note that the extracted β_ℓ using the folding model refers to the root-mean-square mass deformation of the target, while for the other method, β_ℓ refers to that of the ion-ion optical potential due to the mass deformation of the target. It is often assumed that the mass and potential deformations are equal or simply related (Ch73), however there is no clear justification for this assumption (Sa72).

2.5.3 Coulomb Form Factor $F_\ell^C(r)$

The Coulomb potential V_c is given by the two-centre integral (2.2). Let,

$$U(|\underline{r}_T-\underline{r}|) = Z_P e \int \frac{d^3r_P\ \rho_P^C(r_P)}{|\underline{r}_T-\underline{r}-\underline{r}_P|} \qquad 2.38a$$

so (2.2) becomes

$$V_c(r) = Z_Te \int d^3r_T \, \rho_T^c(\underline{r}_T) \, U(|\underline{r}_T-\underline{r}|) \qquad 2.38b$$

where ρ_T^c is not necessarily spherically symmetric. Evaluating 2.38a for ^{12}C with MHO (2.3) charge distribution (K173) shows that $U(|\underline{r}_T-\underline{r}|).|\underline{r}_T-\underline{r}|$ is essentially unity for values of $|\underline{r}-\underline{r}_T|$ larger than R_T^c =3.91 fm for ^{52}Cr with a Wood-Saxon distribution, ρ_T^c (Be64). Therefore, since heavy ions have limited density overlap, the projectile distribution can be represented by a point charge. Hence 2.38b is written as

$$V_c(\underline{r}) = Z_PZ_Te^2 \int d^3r_T \frac{\rho_T^c(\underline{r}_T)}{|\underline{r}_T-\underline{r}|} \qquad 2.39$$

Expanding $1/|\underline{r}_T-\underline{r}|$ in spherical harmonics (Me62)

$$V_c(\underline{r}) = \sum_{\ell m} 4\pi \frac{Z_PZ_Te^2}{(2\ell+1)} Y^*_{\ell m}(\hat{\underline{r}}) \int d^3r_T \frac{r_<^\ell}{r_>^{\ell+1}} Y^*_{\ell m}(\hat{\underline{r}}_T)\rho_T^c(\underline{r}_T) \qquad 2.40$$

where $r_>$ and $r_<$ are the larger and the smaller of the lengths r_T and r. The first term of the expansion 2.40 is the monopole-monopole term and comparing expressions (2.40) with (2.22a) gives

$$V_{\ell m}^c(r) = \frac{4\pi Z_PZ_Te^2}{(2\ell+1)} i^\ell \int d^3r_T \frac{r_<^\ell}{r_>^{\ell+1}} Y_{\ell m}(\hat{\underline{r}}_T)\rho_T^c(\underline{r}_T) \qquad 2.41$$

The deformation in the charge distribution ρ_T^c is again introduced by replacing the target charge radius, R_T^c, by

$$R_T^c = R_T^c(1 + \sum_{\ell m} \alpha_{\ell m}^{c*} Y^*_{\ell m}(\hat{r}_T)) \qquad 2.42$$

where ($\alpha^{c}_{\ell m}$) are the charge dynamic distortion operators. Expanding ρ^{c}_{T} in a Taylor series about R^{c}_{T} (retaining terms linear in α), inserting in (2.41) and using the orthogonality of the spherical harmonics gives

$$V^{c}_{\ell m}(r) = \frac{i^{\ell}4\pi Z_{P}Z_{T}e^{2}}{(2\ell+1)}\,\alpha^{c*}_{\ell m}\,R^{c}_{T}\int dr_{T}\,\frac{r^{\ell}_{<}}{r^{\ell+1}_{>}}\,\frac{d\rho^{c}_{T}}{dR^{c}_{T}}\,(r_{T}-R^{c}_{T}) \qquad 2.43$$

In most DWBA calculations ρ^{c}_{T} is assumed to be a uniform distribution with cut off radius $R^{c'}_{T}$, then the reduced matrix element from (2.43) is given by the product of the form factor $F^{c}_{\ell}(r)$ and the strength A^{c}_{ℓ}.

$$A^{c}_{\ell} = \frac{i^{\ell}\beta^{c}_{\ell}}{(2\ell+1)^{3/2}} \qquad 2.44a$$

$$F^{c}_{\ell}(r) = 3Z_{P}Z_{T}e^{2}\begin{cases}(R^{c'}_{T})^{\ell}/r^{\ell+1}, & r \geqslant R^{c'}_{T}\\ \\ r^{\ell}/(R^{c'}_{T})^{\ell+1}, & r < R^{c'}_{T}\end{cases} \qquad 2.44b$$

where β^{c}_{ℓ} is the root-mean-square charge deformation. If a more realistic distribution is used for ρ^{c}_{T}, such as a Wood-Saxon form then $F^{c}_{\ell}(r)$ becomes

$$F^{c}_{\ell}(r) = 4\pi R^{c}_{T}Z_{T}Z_{P}e^{2}(X+Y) \qquad 2.45$$

where

$$X = \frac{1}{r^{\ell+1}}\int_{0}^{r} dr_{T}\,\frac{d\rho_{T}}{dR^{c}_{T}}\,r^{\ell+2}_{T}$$

$$Y = r^{\ell}\int_{r}^{\infty} dr_{T}\,\frac{d\rho_{T}}{dR^{c}_{T}}\,r^{-\ell-1}_{T}$$

Fig.2.7 shows the contributions of X and Y to (2.45). For $r > R_c^T$, Y can be ignored and $r^{\ell+1}X$ is essentially constant. By comparing 2.44b with 2.45 for $r > R_T^{c'} > R_T^c$, determines $R_T^{c'}$ with a charge distribution ρ_T^c obtained from electron scattering experiments. Thus the expression (2.44) has no free parameters (Ow64)

$$\left(R_T^{c'}\right)^2 = \frac{4\pi R_T^c}{3}\int_0^\infty dr \, \frac{d\rho_T^c}{dR_T^c} \, r^{\ell+2} \qquad 2.46$$

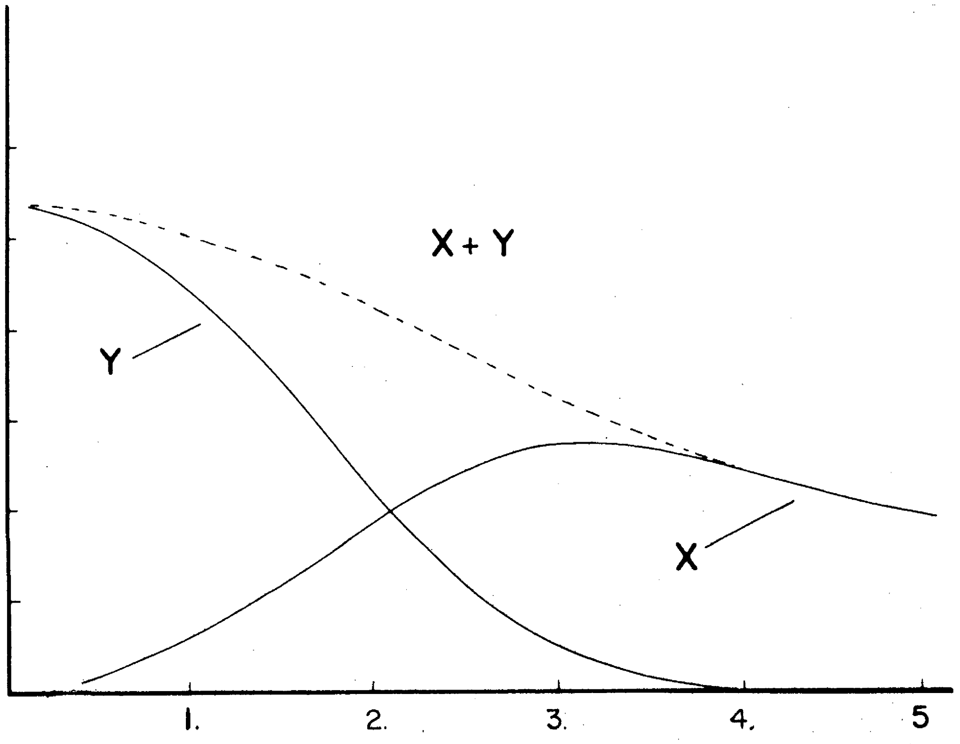

Fig.2.7

It is very important to note that for $r > R_T^{c'}$ (2.44) can be written in a *model independent* form (Al66, Ba62) using the relationship (Ow64)

$$B(E\ell) = \left(\frac{3}{4\pi}\,(R_T^{c'})^\ell \, Z_T e \, \beta_\ell\right)^2 \qquad 2.47$$

where B(Eℓ) is the reduced transition amplitude.

To summarise, the main features of the Coulomb form factor $F_{\ell}^{c}(r)$ are

(i) that for $r > R_T^{c'}$ it is model independent

(ii) it has an explicit ℓ dependence and finally

(iii) because of the long range of the $1/r^{\ell+1}$ term it is necessary to have a large number of partial waves in the distorted wave expansion.

2.6 SINGLE NEUTRON TRANSFER

Consider the stripping reaction A(a,b)B where a=b+n, B=A+n and n denotes the transferred neutron. The reaction mechanism used to construct the reaction amplitude (2.21) assumes that the neutron is stripped off the projectile from a particular shell model configuration and placed into another in the target, without either of the cores taking an active role. This process takes place through the interaction ΔV_β (Post) or ΔV_α (Prior).

In the post representation ΔV_β is the remaining interaction between the final fragments B and b after the effective potential $\tilde{V}_\beta$ has been subtracted

$$\Delta V_\beta = V_\beta - \tilde{V}_\beta = V_{bA}^{N} + V_{bn} + V_{CE} - \tilde{V}_\beta \qquad 2.48$$

V_{bA}^{N} represents the core-core nuclear interaction and it's contributions are assumed to be cancelled out by the nuclear part of the effective potential. This approximation is most accurate for energies below the Coulomb barrier where both V_{bA}^{N} and the optical potential are small (Bu71). The Coulomb interaction V_{CE} is the sum of the monopole-monopole and multipole-multipole terms. The monopole-monopole term is subtracted out by the Coulomb part of the average potential $\tilde{V}_\beta$. The multipole-multipole term represents Coulomb excitation before or after the transfer and therefore cannot be treated consistently in a single step calculation, hence they are neglected. However such multistep processes are generally of second order. The remaining term of eq. (2.48) is the binding potential of the neutron to the core b V_{bn}, and is the interaction through which the stripping occurs. V_{bn} is assumed to be spin independent and only a function of r_{bn} (fig.2.9).

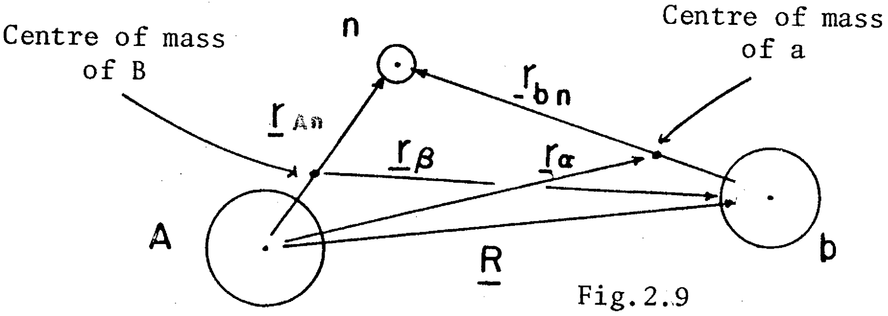

Fig.2.9

The co-ordinates (fig.2.9) are related vectorially by

$$\underline{r}_\alpha = \underline{r}_{Am} - \frac{X_b}{X_a}\underline{r}_{bn} \qquad 2.49a$$

$$\underline{r}_\beta = \frac{X_A}{X_B}\underline{r}_{An} - \underline{r}_{bn} \qquad 2.49b$$

where X_i denotes the mass of the i^{th} particle.

The wave function for the particle B with total angular momentum J_B and z-projection M_B is expanded in wave functions of the core A, with angular momentum and z-projection $(J_A M_A)$, vector coupled to single particle wave functions of the neutron (G163).

$$\Psi^{\alpha_B}_{J_B M_B}(\xi_A,\xi_n,\underline{r}_{An}) = \sum_{\ell_j J_A n} S_B^{\frac{1}{2}}(nj\ell,J_A J_B \alpha_A \alpha_B)\left[\Psi^{\alpha_A}_{J_A M_A}(\xi_A) \times \phi^n_{\ell_j m_j}(\xi_n,r_{An})\right]_{J_B M_B} \qquad 2.50$$

where the square brackets denote vector coupling to $(J_B M_B)$, α's are the quantum numbers other than the one specified and ξ's represent the internal co-ordinates of the appropriate particles. The wave functions ϕ, with angular momentum and z-projection (j,m_j), are the single particle shell model wave functions for the neutron in the target and given by

$$\phi^{n}_{\ell_j m_j}(\xi_n,\underline{r}_{An}) = R_n\ (r_{An})\left[i^{\ell} Y_{\ell m}(\hat{\underline{r}}_{An}) \times \chi_{\frac{1}{2}}(\xi_n)\right]_{jm_j} \qquad 2.51$$

where $R_{n\ell}$ is the radial wave function with principle quantum number n and orbital angular momentum ℓ, and $\chi_{\frac{1}{2}}$ is the neutron spin function. The coefficients $\{S^{\frac{1}{2}}\}$ (2.50) are called spectroscopic factors and represent the degree to which the final state has the configuration denoted by the indices. Since the core A is assumed to play no role in the reaction and is in its ground state the indices, J_A, J_B, α_A, α_B are dropped from $S^{\frac{1}{2}}$. The projectile wave functions have the same form as (2.51).

Using the wave functions given above, the nuclear matrix elements are evaluated and given by

$$<bB|\Delta r_\beta|aA> = \sum_{jj'L} \bar{i}^{L}(-1)^{J_b-M_b}(2J_b+1)^{\frac{1}{2}} <J_A j M_A m_j|J_B M_B>$$

$$\times <J_a J_b\ M_a,-M_b|j'm_{j'}> <Lj'M\ m_{j'}|jm_j>$$

$$\times F_{LMjj'}\ (\underline{r}_{An},\underline{r}_{bn})$$

$$F_{LMjj'}(\underline{r}_{An},\underline{r}_{bn}) = (-1)^{\ell+j+M}\frac{(2\ +1)^{\frac{1}{2}}\ (2J_a+1)^{\frac{1}{2}}}{(2J_B+1)^{\frac{1}{2}}} W(\ell L\tfrac{1}{2}j',\ell'\ell)\, i^{L+\ell'-\ell}$$

$$\times S^{\frac{1}{2}}_{B}(nj\ell)\ S^{\frac{1}{2}}_{a}(n'j'\ell')\ \left[(-1)^{m_j}\ Y^{*}_{\ell m}(\hat{\underline{r}}_{An}) \times Y_{\ell'm'}(\hat{\underline{r}}_{bn})\right]_{L,-M}$$

$$\times R_{n\ell}(r_{An})\ V_{bn}(r_{bn})\ R_{n'\ell'}(r_{bn})$$

$$m_j = M_B - M_A; \qquad m_j = M_a - M_b; \qquad M = m_j - m_{j'} \tag{2.52}$$

where the primed quantum numbers refer to the neutron plus core b, W is a Racah coefficient and L the orbit angular momentum transferred.
No summation over the principle quantum numbers is required because of energy consideration. The triangular conditions (denoted by Δ) over the various quantum numbers, as a result of angular momentum and parity conservation are given below:

$$\left.\begin{array}{lll} \Delta(J_A, J_B, j); & \Delta(J_a, J_b, j'); & \Delta(L, \ell, \ell') \\ \Delta(L, j, j'); & \Delta(\ell, j, \tfrac{1}{2}) \;; & \Delta(\ell', j', \tfrac{1}{2}) \\ \pi_a \pi_b = (-1)^{\ell'}; & \pi_A \pi_B = (-1)^{\ell} & \end{array}\right\} \tag{2.53}$$

The ½ in the above conditions is the spin of the neutron.

The expression for the differential cross-section is obtained by inserting (2.52) in (2.13) and making use of the Clebsch-Gordan coefficients relations to sum over the z-projections giving

$$\frac{d\sigma}{d\Omega} = \frac{\mu_\alpha \mu_\beta}{(2\pi\hbar^2)^2} \frac{k_\beta}{k_\alpha} \frac{(2J_B+1)(2J_A+1)}{(2J_b+1)(2J_a+1)} \sum_{LMjj'} |\beta^{LM}_{jj'}(\theta)|^2 \tag{2.54}$$

where

$$(2L+1)^{\frac{1}{2}} i^L \beta^{LM}_{jj'}(\theta) = \int d^3r_\alpha d^3r_\beta \chi_\beta^{(-)*}(\underline{k}_\beta, \underline{r}_\beta) F_{LMjj'}(\underline{r}_{An}, \underline{r}_{bn}) \chi_\alpha^{(+)}(\underline{k}_\alpha, \underline{r}_\alpha) \tag{2.55}$$

Finally to compute (2.54), the χ's are expanded into a finite number of partial waves, which for heavy ion scattering could be quite large. Because the radial parts of the bound state and partial wave functions are not analytic the final expression for (2.55) involves calculation of a large number of two dimensional (2-D) radial integrals which present a large computational effort. Such a calculation is commonly called 'full finite range'. The transfer analysis presented in this work used the full finite range DWBA code LOLA (De73). The code was based on the calculations of Austern *et al* (Au64) and uses Gaussian numerical integration to evaluate the (2-D) integrals.

Conventional DWBA codes use the 'zero-range approximation' (whereby $\beta^{LM}_{jj'}$ (2.55), is reduced from a 6-D to a 3-D integral) which in essence implies that the nucleon is restricted to move along the vector $\underline{R}$ (fig.2.11) in the transfer process and ignores the resultant change in the centre of mass of the projectile (De73). As a result of this approximation the transferred angular momentum L besides conforming with conditions imposed by (2.53) must also comply with (Bu71, De73)

$$\ell_1 + \ell_2 + L \;=\; \text{even} \qquad 2.56$$

The values of L which satisfy (2.56) are called 'normal', whilst those which do not are termed 'non-normal'. The zero-range calculations performed by Buttle and Golfarb (Bu71) have been shown to give good representation of single nucleon transfer data (Pa74) for incident energies below the Coulomb Barrier. For higher bombarding energies, the zero range approximation becomes dubious and in some cases totally inadequate in reproducing heavy ion transfer data (Ko73, De73).

In summary, the calculation of the single neutron stripping (or pickup) assumes that the neutron is picked up from a single particle orbit in the projectile and placed into one in the target, with cores b and A playing only a passive role. Also that the interaction V_{bn}, responsible for the transfer is spin independent and a function only of r_{bn}. Finally the process is assumed to be a single-step direct process and hence Coulomb excitation is ignored.

Chapter 3

EXPERIMENTAL METHOD

3.1 INTRODUCTION

In this chapter the experimental procedures adopted for the measurement of the elastic and inelastic excitation functions at energies close to Coulomb barrier are described. The reactions listed in table 3.1 were studied and the scattered projectiles were observed using a magnetic spectrometer at 120° with a position sensitive detector located in the focal plane.

Table 3.1

Reactions	Energy Range (MeV) Lab.
$^{52}Cr(^{12}C,^{12}C)^{52}Cr^*$ (1.434 MeV)	22.0 - 30.0
$^{52}Cr(^{13}C,^{13}C)^{52}Cr^*$ (1.434 MeV)	19.5 - 30.0
$^{54}Fe(^{12}C,^{12}C)^{54}Fe^*$ (1.409 MeV)	19.5 - 32.0
$^{54}Fe(^{13}C,^{13}C)^{54}Fe^*$ (1.409 MeV)	19.5 - 32.0
$^{52}Cr(^{16}O,^{16}O)^{52}Cr$ (G.S.)	31.0 - 40.0
$^{52}Cr(^{16}O,^{16}O)^{52}Cr^*$ (1.434 MeV)	31.0 - 40.0
$^{52}Cr(^{18}O,^{18}O)^{52}Cr$ (G.S.)	30.0 - 40.0
$^{52}Cr(^{18}O,^{18}O)^{52}Cr^*$ (1.434 MeV)	30.0 - 40.0
$^{54}Fe(^{16}O,^{16}O)^{54}Fe$ (G.S.)	30.0 - 44.0
$^{54}Fe(^{16}O,^{16}O)^{54}Fe^*$ (1.409 MeV)	30.0 - 44.0
$^{54}Fe(^{18}O,^{18}O)^{54}Fe$ (G.S.)	31.5 - 44.0
$^{54}Fe(^{18}O,^{18}O)^{54}Fe^*$ (1.409 MeV)	32.0 - 44.0

Because of contaminants in the targets and the many transfer channels which are open for bombarding energies above the Coulomb barrier, the detection system had to incorporate good energy resolution and mass identification. The alternative techniques which are available for the cross-section measurements involved the use of a semi-conductor particle telescope or particle-gamma coincidences. The semi-conductor telescope had to have mass identification capabilities better than 1 in 18 for incident particle energies of approximately 10 MeV. This required a transmission detector less than 5 μm thick, a requirement unattainable at the time. The second technique was attempted with a 7.5 cm × 7.5 cm NaI(Tl) and annular surface barrier detector using an ^{16}O beam. The large cross-sections for compound nucleus formation with carbon and oxygen contaminants in the target give both gamma rays and alpha particles in the energy regions of interest. In order to reduce the carbon build-up a copper shroud, surrounding the self supporting ^{52}Cr and ^{54}Fe targets, was maintained at liquid nitrogen temperature. However the relative compound nucleus to inelastic yield was still high and made the data reduction difficult.

The double focussing spectrometer inherently can provide good energy resolution. The background contribution under the inelastic group from the low energy tail of the elastic peak was negligible. The elastic peaks from contaminants in the targets were resolved. Also with the energy and momentum analysis the nucleon transfer reactions could be resolved from the peaks of interest. However there are obvious disadvantages associated with the use of the spectrometer; only one reaction at one angle could be measured at any one time, whereas with the other methods several reactions could be studied at two or three angles simultaneously. The use of the spectrometer also requires charge state distributions to be measured and associated corrections to be made.

3.2 TARGET PREPARATION

The carbon backed targets were prepared from enriched material (^{52}Cr, 99.8% and ^{54}Fe, 96.8%) in the form of oxides, obtained from Oak Ridge National Laboratory. The carbon backings were made by evaporating natural carbon onto glass slides coated with a releasing agent (RBS 25, Stansen & Co., Melbourne). The ^{54}Fe targets were prepared by placing the oxide in a tungsten boat and heating it in an atmosphere of hydrogen. Then the isotopic metal was evaporated in vacuum onto the carbon coated slides. The carbon backed foils were floated on distilled water and picked up on target frames. The ^{52}Cr targets were made almost in the same way except a tantalum boat was used to act as a reducing agent. The reduction of the chromium oxide to the metal was achieved by slowly heating the crucible before evaporation.

The energy resolution for detecting carbon and oxygen ions is primarily determined by the target thickness. Since the ions were detected after reflection from the target, the energy spread due to straggling and energy loss of the beam and reaction products is considerable. Therefore the targets had to be thin. Target thicknesses were measured using a mixed α-source (^{241}Am, ^{244}Cm, ^{239}Pu) by comparing the energy loss for α-particles transmitted through the carbon and carbon plus target. The targets used had 10-15 μgms/cm^2 carbon backing and 12-16 μgms/cm^2 of ^{54}Fe or ^{52}Cr for the carbon beams and 5-12 μgms/cm^2 for the oxygen beams. The lowering in the mean incident energy due to energy loss in the target was less than 0.07% and hence ignored.

The calculated energy spread due to energy loss and straggling in the target, added in quadrature, is approximately 110 keV, with the target at 65°. Smaller target angles would have interfe-red with the operation of the monitor detector at 45°.

3.3 BEAMS

The elastic and inelastic excitation functions of ^{12}C, ^{13}C, ^{16}O and ^{18}O projectiles were studied using the ANU EN tandem. The negatively charged carbon and oxygen ions were produced by HVEC duo plasmatron using isotopically enriched methane for ^{13}C and carbon dioxide for ^{18}O each mixed with 98% hydrogen. The C^- and O^- beams were stripped in a carbon foil at the terminal and were subsequently momentum analysed by a 90° double focussing magnet. The beams were deflected by a switching magnet and then focussed onto the target by a magnetic quadrupole doublet. A tantalum collimator (0.3 cm diameter) was placed 32 cm in front of the target. The collimator was polished to reduce slit edge scattering and therefore decreasing the low energy tail of the elastic peak.

The beam was collected in a small, magnetically suppressed Faraday cup 5 cm away from the target and current integrated by an Ortec 439 digitizer. The Faraday cup had a graphite beam stop to eliminate any backscattering of carbon and oxygen ions. Beam intensities were typically 50 particle nano amps.

3.4 SCATTERING CHAMBER AND MONITOR ASSEMBLY

To monitor the measured yield in the spectrometer two monitors at ±45° and ±40°, for carbon and oxygen scattering respectively, were used. The elastic cross-section at these angles, within the range of the excitation functions, is equal to that for Rutherford scattering. This was confirmed by calculating the elastic scattering at these angles with optical potentials which fit the elastic scattering data. Two monitors were used to reduce the error in the normalisation due to beam spot movement in the horizontal plane. The calculated uncertainty in the normalisation due to the motion of the beam spot on the target is approximately 2%.

The target chamber (fig.3.1, 3.2) is of a sliding band type with internal diameter 13.4 cm. The monitor assemblies are held by a central column (fig.3.2). This is clamped to an external rigid support so that the monitors do not move relative to the optical axis of the beam line when the spectrometer is moved.

The monitors were mounted on perspex blocks with two tantalum collimators placed in front of each detector. The collimators were set 1 cm apart and the front collimator was 4.0±0.2 mm in diameter and the rear was 1.01±0.01 mm. Each monitor assembly was suspended from a steel arm clamped to the central support. The rear collimators were set at 5.0±0.1 cm away from the target by sliding the perspex blocks along the steel arms. The monitor angles were nominally set against an angular scale above the steel arms (fig.3.2). To accurately measure the angles with respect to the optical axis of the beam line the clamp between the external and the central support was removed, allowing the monitors to rotate with the spectrometer. Then with a telescope mounted along the beam axis, the spectrometer was rotated until the rear collimator was sighted. For reproducable and accurate measurements of the monitor angles (E168) the spectrometer was leveled and rotated through +10° to reach the required angles. The clamp was placed back with spectrometer at an angle such that the monitor angles were equal relative to the optical axis of the beam line. The monitors were small area surface barrier detectors with a maximum depletion depth of 100 μm manufactured at the ANU Nuclear Physics Laboratory.

Since the particles reaching the position sensitive detector from the target had to travel 200 cm it was necessary to have good vacuum to minimise charge exchange collisions. The pressure in the chamber and in the magnet box was maintained at a maximum of 8.0×10^{-6} torr by a 250 litre/sec oil diffusion pump. At this pressure the mean free path is of the order of 1000 cm.

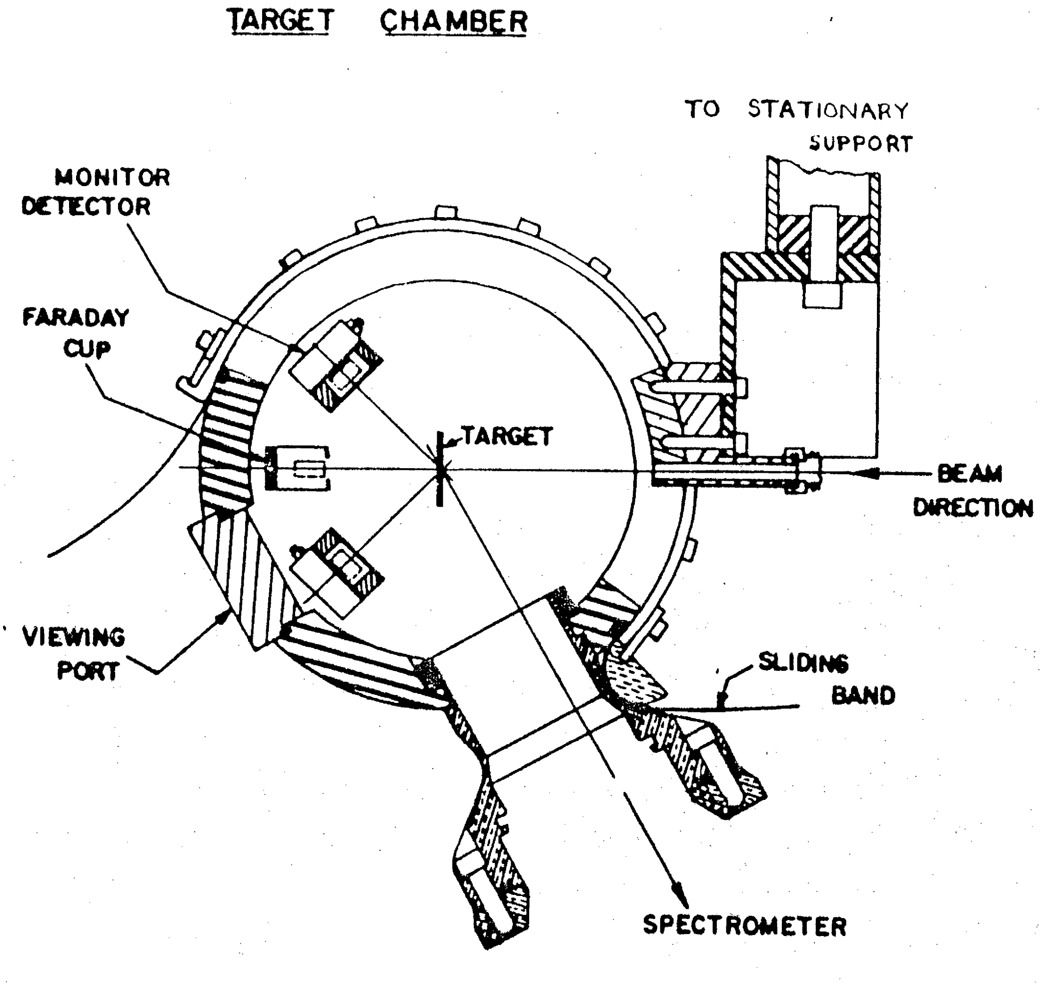

Fig.3.1 Top elevation of the spectrometer scattering chamber.

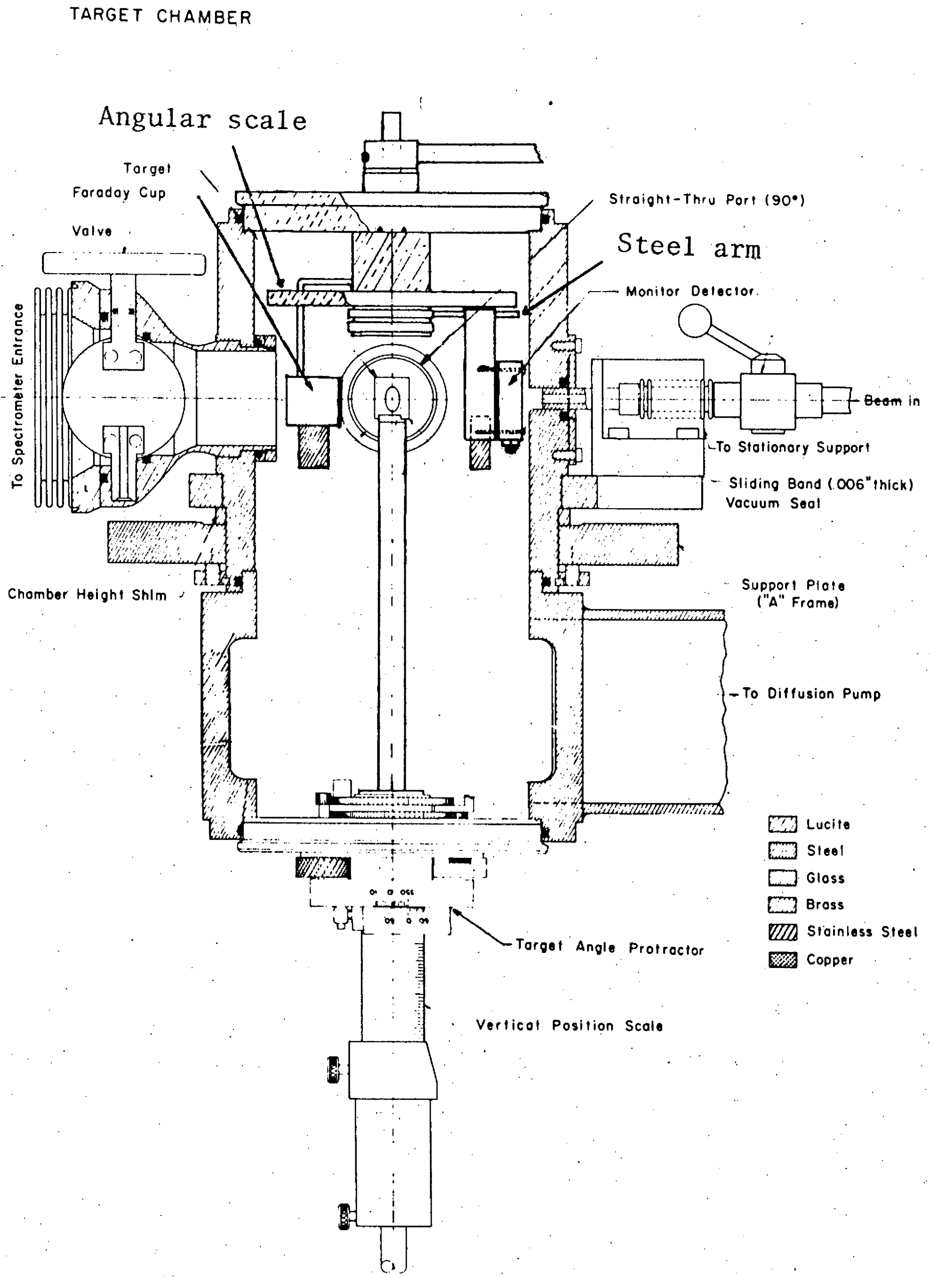

Fig.3.2 Vertical cross-section of the spectrometer sliding band type chamber.

3.5 SPECTROMETER

The spectrometer, designed by Ikegami (Ik58) is a double focussing ($n=\frac{1}{2}$), large solid angle (13 mstr) magnet with target and focal plane outside the magnetic field. Documentation of the tests and properties of this instrument are described by Elliot (E168). The spectrometer has a total bending angle of 188° with a 61 cm radius and could be set between -10° and 155° to the beam axis with an accuracy of ±0.05°. The focal plane is 24.2 cm outside the magnetic field and inclined at an angle $\phi=48°$ (fig.3.3) to the mean ray. The position of the focal plane has been shown to be independent of the energy and momentum of the incident particles. The maximum energy carbon (5^+) and oxygen (6^+) ions which can be focussed on the image plane are 56 MeV and 60 MeV respectively and thus was no limitation on the present experiments.

An ion implanted position sensitive detector (PSD), with a maximum depletion depth of 100 μm and active area 4.8 cm × 0.8 cm, was used in the focal plane.

The dispersion D, is the property of the spectrometer that enables it to spacially separate particles with different momenta p and p+ δp, and is defined by (E168)

$$D = \frac{\delta y}{R} \cdot \frac{p}{\delta p} = \frac{\delta y}{R} \cdot \frac{2E}{\delta E} = 3.58 \pm 0.07 \qquad 3.1$$

where R=61 cm and δy is the change, induced by δp, in the position at the focal plane, perpendicular to the mean ray. Using equation (3.1) the energy spanned by the PSD at the focal plane for 8 MeV ^{12}C is 240 keV, where $\delta y = \ell \cos 48°$ cm and $\ell=4.8$ cm is the length of the PSD. When using oxygen beams the PSD was rotated so that it was normal to the mean ray. This resulted in a slight degradation of the position resolution (E168), however was offset by a 33% increase in kinematic range to 480 keV

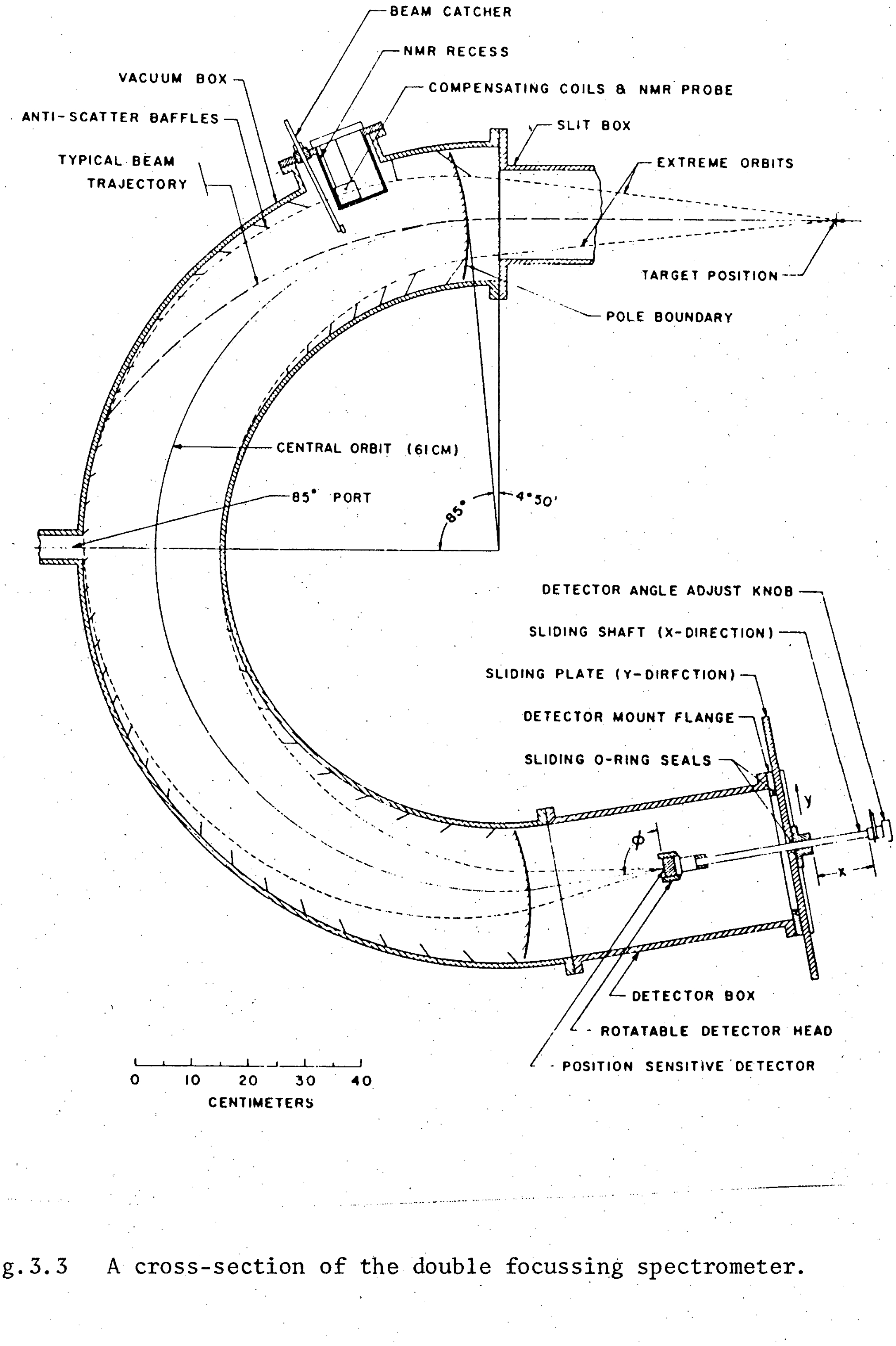

Fig.3.3 A cross-section of the double focussing spectrometer.

for 11. MeV ^{16}O. Thus for the elastic or inelastic peaks to be well on the counter the energy spread had to be considerably less than 240 keV and 480 keV for carbon and oxygen respectively. These values placed the limit on the maximum target thickness and horizontal slit settings.

The solid angle defining slits for the spectrometer are positioned at the boundaries of the inhomogeneous magnetic field. The horizontal and vertical slit settings used for carbon and oxygen scattering were ±0.5°, ±4.5° and ±0.25°, ±4.0° respectively. This resulted in kinematic broadening of approximately 80 and 50 keV respectively.

3.6 CHARGE STATE FRACTION

The measured 5^+, 6^+ and 7^+ charge state (CS) distributions for ^{16}O on ^{54}Fe as a function of emitted ^{16}O energy are shown on fig.3.4. The distributions were obtained by using the elastic scattering yield for the various CS's with the spectrometer at 120° for the low energy points. For emitted energies larger than 12.5 MeV the spectrometer was set at 90°. The measured CS fractions were corrected for small contributions for the 4^+ and 8^+ CS using equilibrium CS distributions published by D.L. Bach *et al* (Ba65) obtained for ^{16}O on relatively thick Ni targets (580 μgms/cm^2). It was shown that these corrections were appropriate by measuring the 4^+ and 8^+ CS fractions at two energies. The more prolific charge state (6^+) was used to measure all the oxygen cross-sections. For carbon scattering the charge state distributions measured on ^{54}Fe targets were available from previous work done at ANU (Pa74) (fig.3.5).

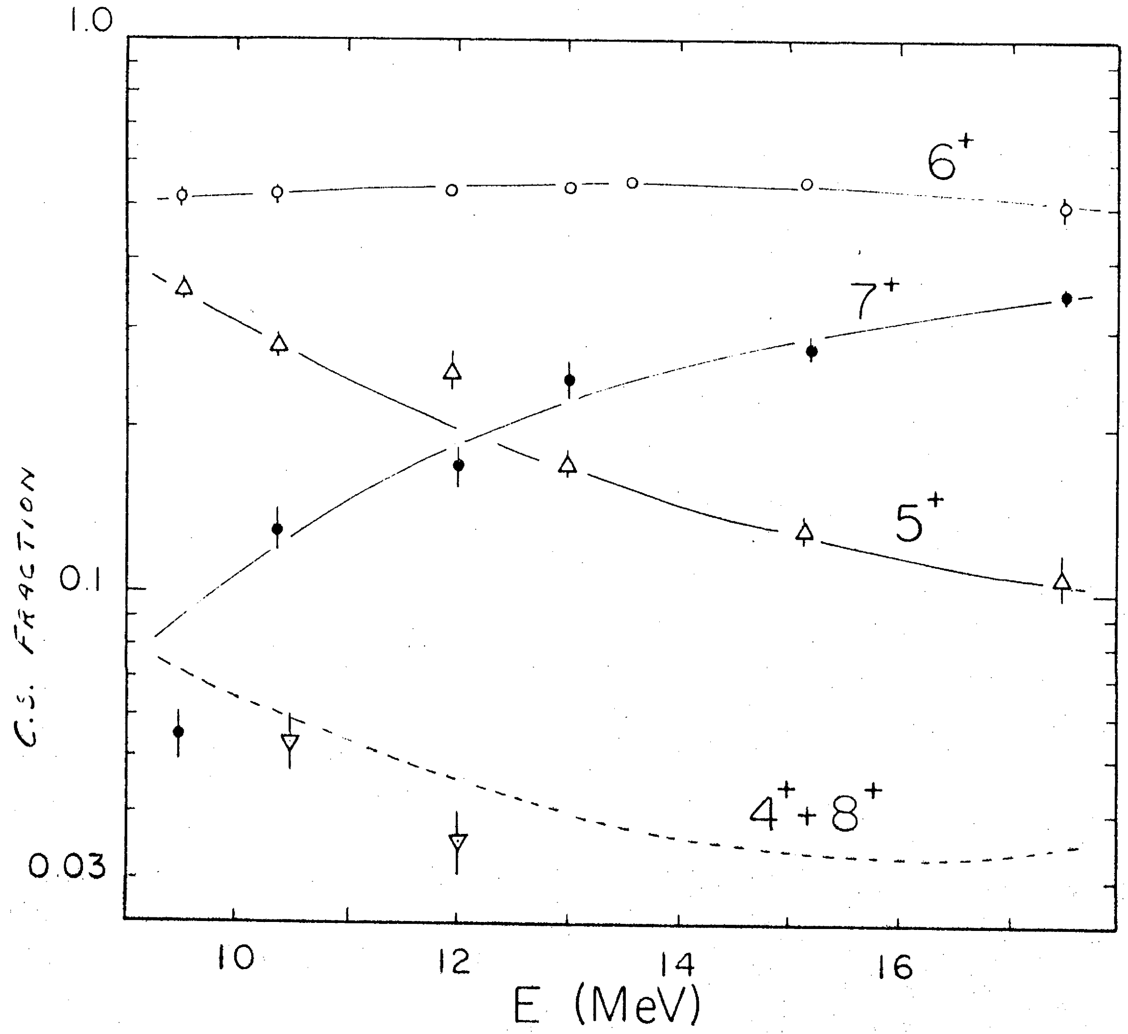

Fig. 3.4 Charge state fractions for ^{16}O on ^{54}Fe as a function of emitted ^{16}O energy. The dashed curve is the 4^+ plus 8^+ correction to the distributions (Ba65). The solid lines are to guide the eye.

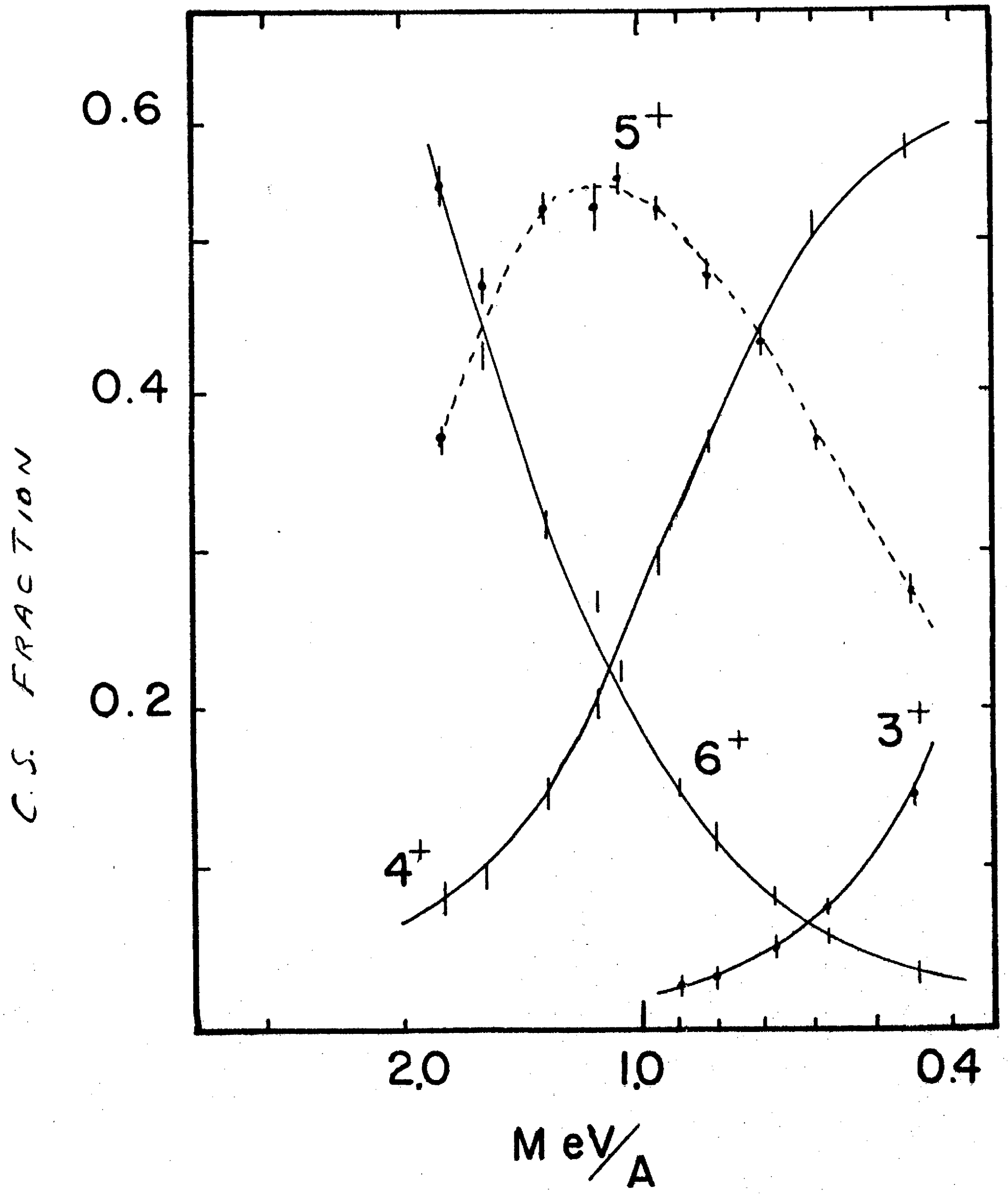

Fig.3.5 Charge state fractions for ^{12}C as a function of emitted energy/nucleon. The curves are to guide the eye.

3.7 DATA STORAGE

The electronic configuration used to collect the data is shown in fig.3.6. For the PSD the energy and energy × position signals were amplified and shaped, then both pulses were passed through an Ortec 464 PSD analyser which divided the signals and removed low energy noise. The output pulses were then proportional to the incident energy and position. The data were stored on disc in event-by-event mode using an IBM 1800, and could be easily sorted on line, to check that the position peak was well centred on the counter.

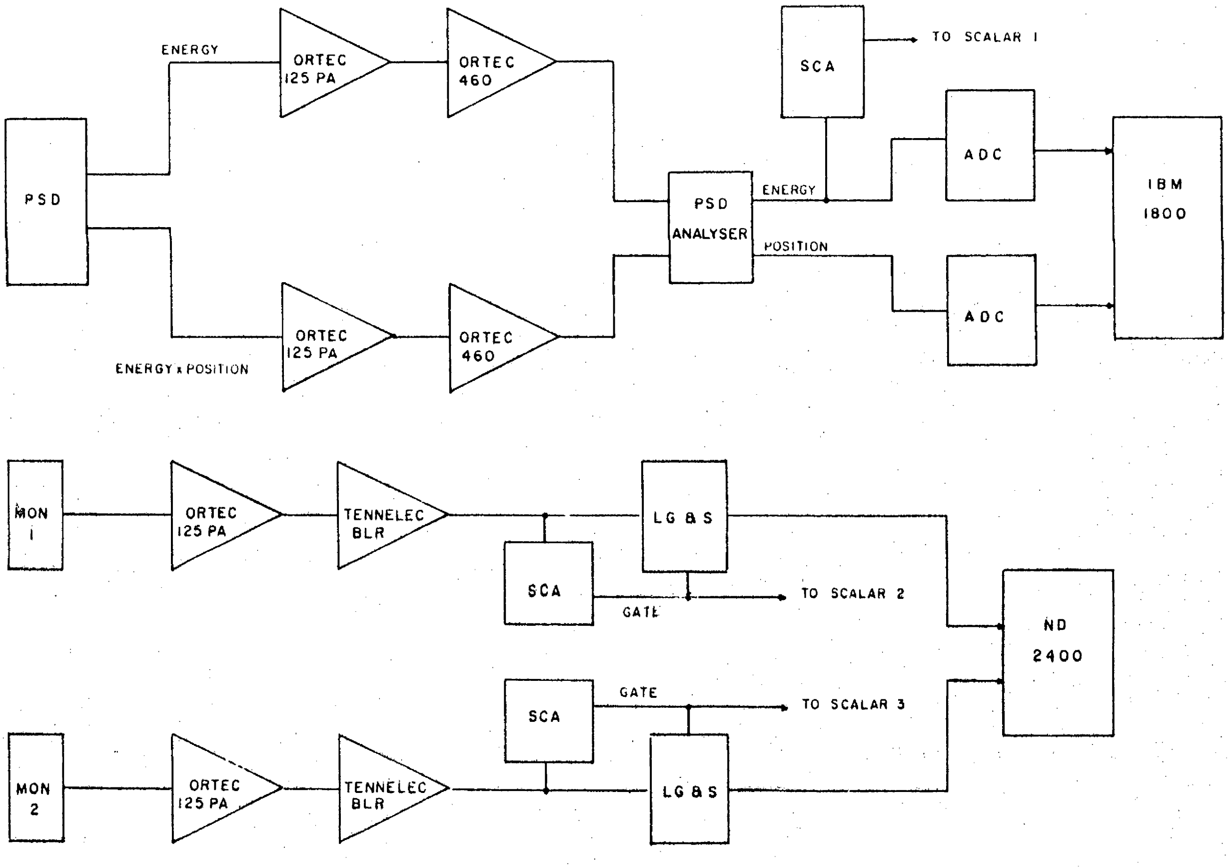

Fig.3.6 Electronic configuration used in the collection of the PSD and monitors spectra.

Energy signals from the monitors were amplified and shaped and discriminators used to remove low energy pulses. The spectra were stored in a ND 2400, which routed the signals from the different detectors to appropriate sections of the total spectrum. The spectra were transferred onto disc (IBM 1800) after each run.

Dead time corrections in the ADC's were done by scaling the number of gate pulses from the PSD and monitors. The difference in the scalar readings and the total number of counts in each spectrum gave the required dead time. Dead time in the computer was very small since the counting rate in the PSD was about three counts a second for elastic scattering. For the multichannel analyser the dead time was typically 0.5%.

3.8 DATA ANALYSIS

The cross-section for elastic scattering at low incident energies were normalised to those of Rutherford scattering. The same normalisation N, was then used for the elastic and inelastic cross-sections at higher incident energies. An alternative of normalisation is to use the physically measured angles and solid angles to calculate N. However the former method eliminates any error in setting the monitor angles (Rutherford cross-section varies very rapidly at forward angles) and measured solid angles. When both methods were used the agreement was excellent.

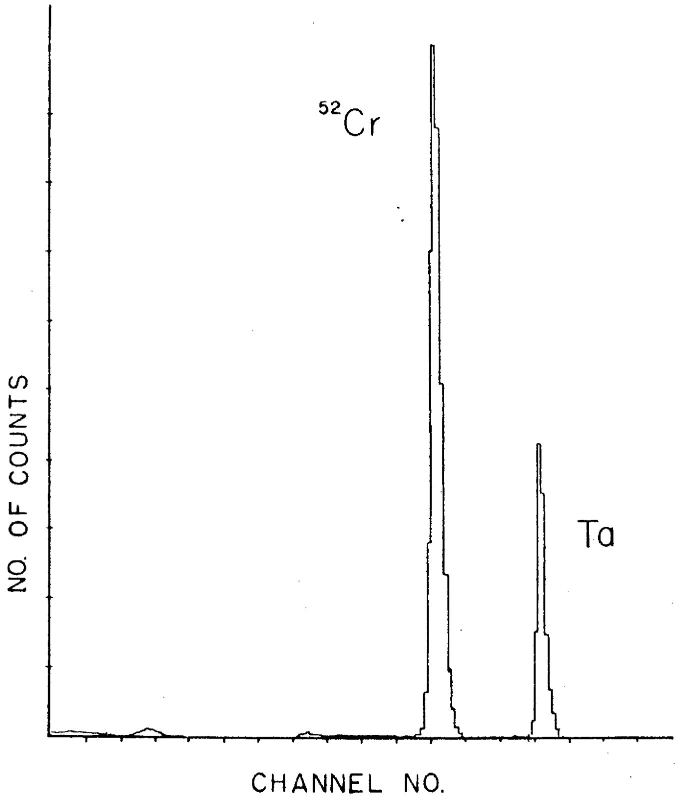

Fig.3.7 Monitor spectrum for 35 MeV (Lab) ^{16}O incident on ^{52}Cr.

The differential cross-section as a function of incident energy E was calculated from:

$$\frac{d\sigma}{d\Omega}(E) = \frac{N}{K_r} \cdot \frac{1}{E^2} \cdot \frac{Y_s}{Y_1+Y_2} \qquad 3.2$$

where K_r is the CS fraction for CS r, Y_s is the elastic or inelastic yield in the spectrometer and Y_1, Y_2 are the elastic scattering yields in the monitors.

The quantities Y_1 and Y_2 were extracted from the monitor spectra (Fig.3.7) by summing between two markers set around the elastic scattering peak of ^{52}Cr or ^{54}Fe. Background between the markers was subtracted by linear interpolation from the average number of counts in a window set below the elastic peak and a window above. The backgrounds under the elastic peaks were typically 1.5% of Y_1 or Y_2. Because of the adopted method of normalisation, it was not necessary to take into account the 3% impurity of ^{56}Fe in the ^{54}Fe targets which was not resolved in the monitor spectra. The elastically scattered oxygen ions from ^{56}Fe detected in the spectrometer were well away in energy from those scattered off ^{54}Fe and not present in the energy spectrum of the PSD.

The energy spectrum from the PSD was calibrated by recording the energy spectra of the elastic peaks at several bombarding energies. The reaction products were then identified by their energy and position. The background under the inelastic peaks was checked with ^{16}O projectile by setting the magnetic field in the spectrometer so that particles with energy 300 keV higher than the inelastic scattered ^{16}O could be detected on the PSD. The background was estimated to be less than 2% and not corrected for in the inelastic yield. The yield Y_s was extracted by setting a window over the elastic or inelastic peak in the energy spectrum and integrating the total projection of the position spectrum, after making sure that the position peak is well centred on the counter. The ^{18}O inelastic data was not as straight forward to analyse because of single nucleon transfer reactions contaminating the ^{18}O peaks. The reactions ^{52}Cr(^{18}O,^{17}O), ^{54}Fe(^{18}O,^{17}O), ^{54}Fe(^{18}O,^{19}F) have small ground state Q-values -0.012 MeV, 1.2228 MeV and -0.86 MeV respectively and for transfer to excited states of the residual nuclei the reaction products are within 300 keV of the inelastic ^{18}O. So for the ^{18}O inelastic scattering thinner targets (≈ 7 μgms/cm^2) were used to increase the energy resolution. By moving a narrow window across the ^{18}O inelastic energy peak, the corresponding projections showed the ^{17}O or ^{19}F to be well separated in position from the ^{18}O group. Thus Y_s was obtained by summing the position peaks of interest for each projection.

The measured elastic and inelastic excitation functions are shown in Chapter 4. The assigned error bars were calculated from the statistical error in the spectrometer yield $\pm\sqrt{Y_s}$ and the error in the charge state distributions, estimated to be 2%. The error in the monitor yield Y_1+Y_2 was very small and not included. The total error was obtained by adding the individual contributions in quadrature. The estimated error in the normalisation (2%) was not included.

Chapter 4

RESULTS OF THE OPTICAL MODEL AND DWBA ANALYSES

4.1 ELASTIC SCATTERING

4.1.1 FOREWORD

In this section the ^{16}O and ^{18}O elastic scattering data are described in a semi-classical framework and parameterised using the optical model (OM). The elastic data for ^{12}C and ^{13}C scattering from ^{48}Ca, ^{50}Ti, ^{52}Cr, ^{53}Cr and ^{54}Fe measured by Parkinson (Pa74) are also studied. The carbon data had not been previously analysed. The purpose of this analysis is to extract optical potentials to be used in the inelastic and transfer DWBA codes. The sets are also used to calculate Coulomb barriers and to determine the variation in the effective potential with target mass numbers for the different projectiles.

4.1.2 Semi-Classical Description of the Elastic Data

The results of the elastic scattering measurements of ^{16}O and ^{18}O on ^{52}Cr and ^{54}Fe are shown on fig.4.1. The excitation functions are structureless and all exhibit the same qualitative features. The general features can be physically understood through a semi-classical description, where the projectile is assumed to travel along a classical trajectory. This treatment is justified since the Sommerfeld parameter $\eta = Z_P Z_T e^2/\bar{\lambda} \approx 18$ (Wi66, Br72) is large (St64). A useful parameter to use in this description is the apsidal distance D for a pure Coulomb orbit:

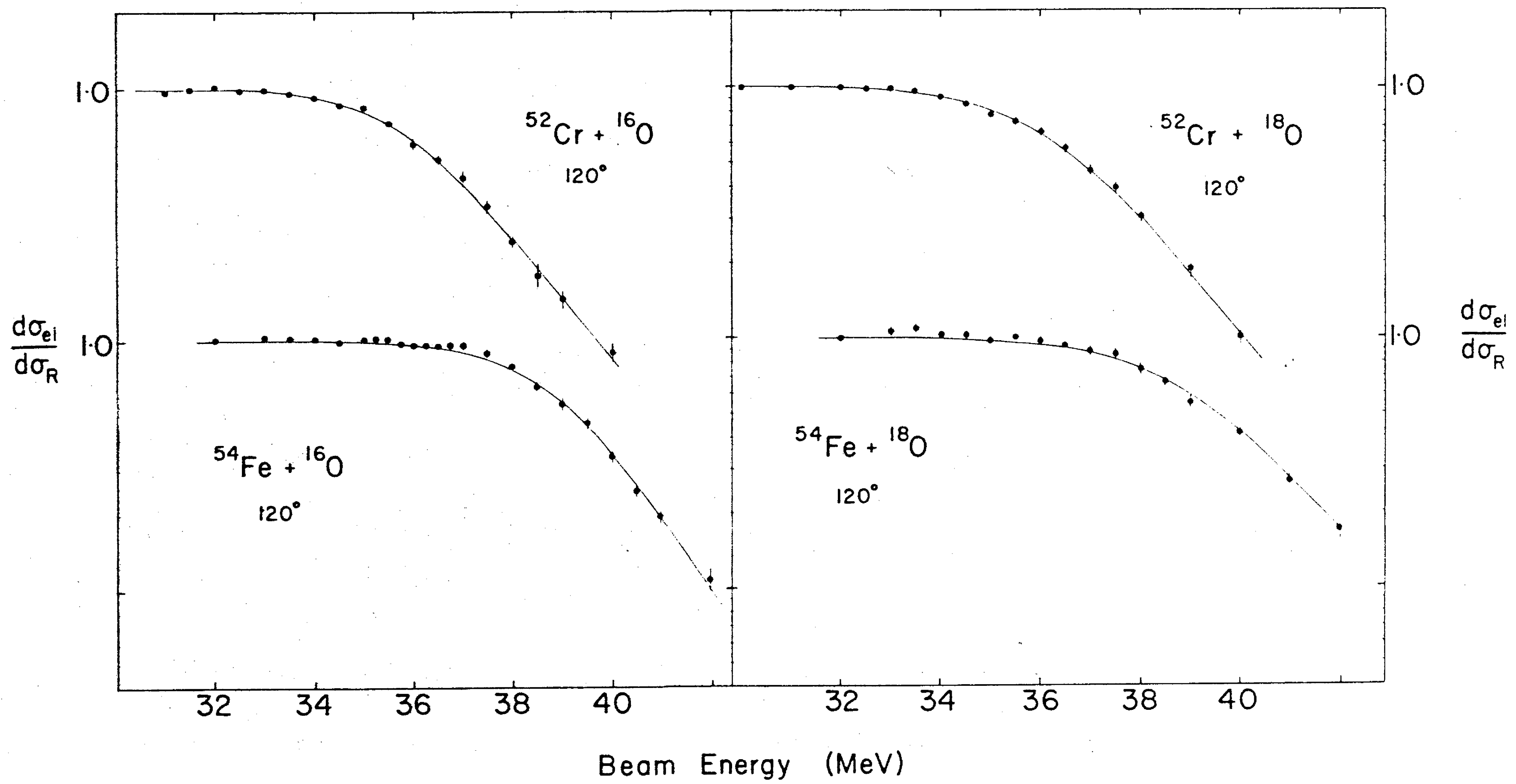

Fig.4.1 ^{16}O and ^{18}O elastic scattering excitation functions at 120° (Lab). The OM fits to the data are obtained using optical parameter sets in table 4.2a.

$$D = \frac{Z_P Z_T e^2}{2E_{CM}} (1 + CSC(\theta/2)) \qquad 4.1$$

where E_{CM} and θ are the centre of mass energy and angle respectively. It is important to note that (4.1) does not take into account the nuclear force (fig.4.2), however since the heavy ion reactions discussed here are peripheral or gentle collisions, this parameterisation is appropriate for a qualitative discussion.

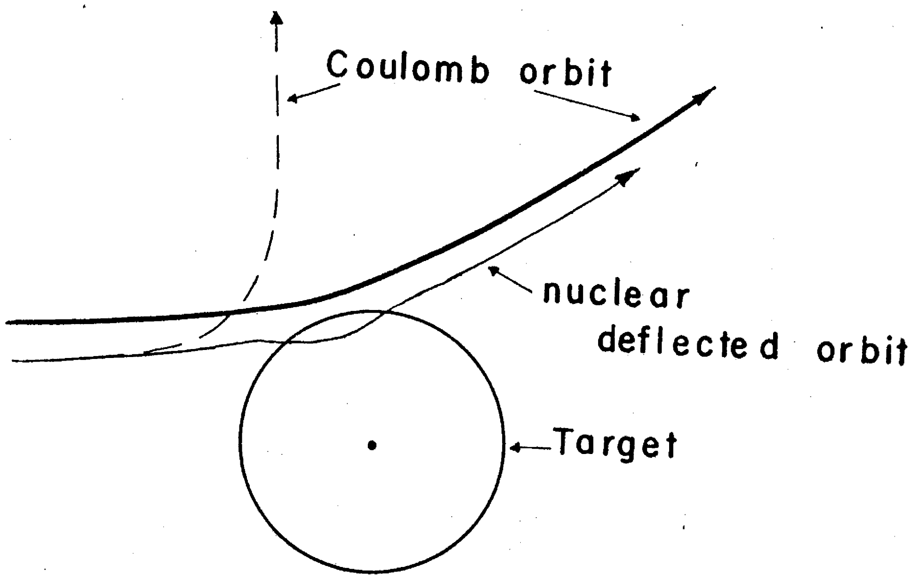

Fig. 4.2

At low incident energy the apsidal distance is large and the nuclei interact only through the long range Coulomb force, therefore the elastic differential cross-section is equal to that for Rutherford scattering. For smaller D, the nuclei start to overlap and the strong nuclear attraction gives rise to a rapid increase in the probability for population of non-elastic channels, namely compound nucleus formation, inelastic and transfer reactions. This results in flux being removed from the elastic channel and an exponential drop in the measured ratio of the elastic to Rutherford cross-sections ($d\sigma_{e\ell}/d\sigma_R$) with decreasing D (fig.4.1).

Similar excitation functions at 176° (Lab.) for $^{52}Cr(^{16}O,^{16}O)^{52}Cr$ and $^{52}Cr(^{18}O,^{18}O)^{52}Cr$ have been reported by Eisen *et al* (Ei72). The

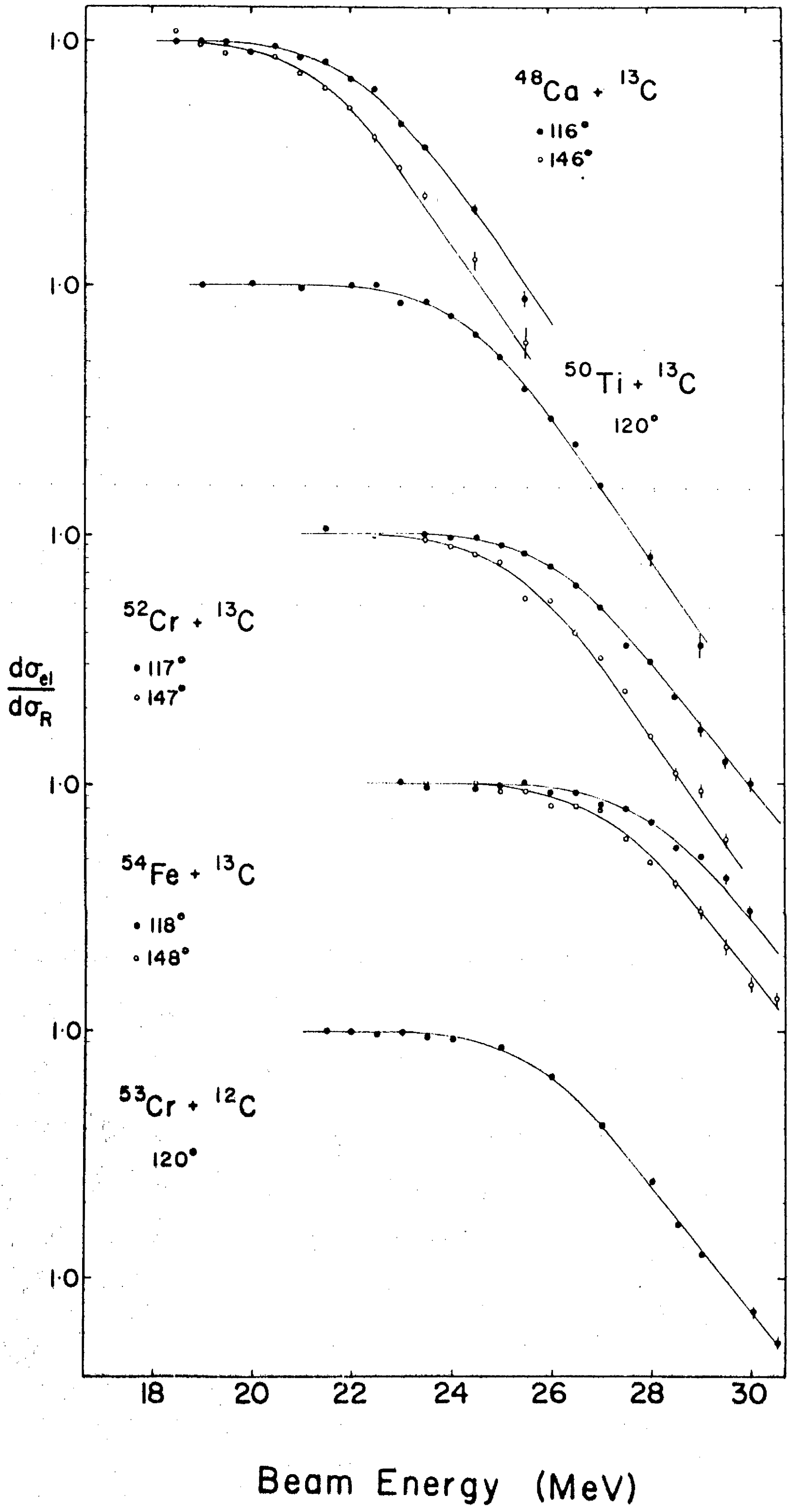
^{48}Ca + ^{13}C
• 116°
◦ 146°
^{50}Ti + ^{13}C
120°
^{52}Cr + ^{13}C
• 117°
◦ 147°
^{54}Fe + ^{13}C
• 118°
◦ 148°
^{53}Cr + ^{12}C
120°
$\frac{d\sigma_{el}}{d\sigma_R}$
1·0
1·0
1·0
1·0
1·0
1·0
18
20
22
24
26
28
30
Beam Energy (MeV)

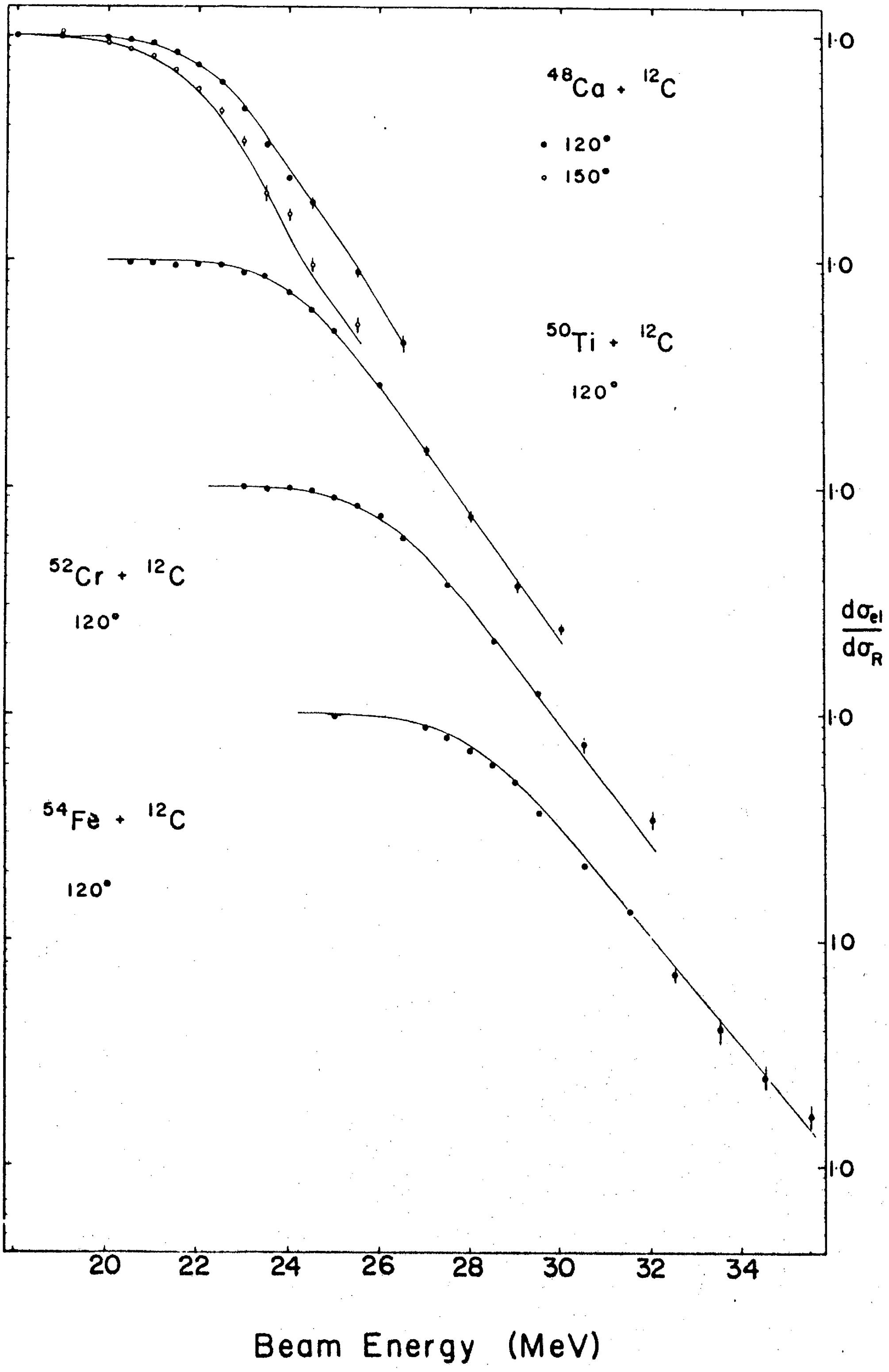

Fig.4.3 ^{12}C and ^{13}C elastic scattering excitation functions at nominally 120° (Lab). The OM fits to the data are obtained using optical model parameter sets in table 4.1a.

elastic scattering of ^{12}C and ^{13}C on ^{48}Ca, ^{50}Ti, ^{52}Cr, ^{53}Cr and ^{54}Fe (Pa74) also show the same qualitative behaviour (fig.4.2). Unlike angular distributions or excitation functions measured at forward angles (Vi72, Ba75), the data does not exhibit any oscillations or rise in $(d\sigma_{e\ell}/d\sigma_R)$ before the final fall off. These oscillations are attributed to interference between two or more orbits which have the same scattering angle but different impact parameters (Ma73). Such a phenomenon has not been observed for back angle scattering.

Several important features can be pointed out by plotting the experimental $(d\sigma_{e\ell}/d\sigma_R)$ as a function of D. The plots for both ^{12}C and ^{13}C scattering are indistinguishable between ^{48}Ca, ^{50}Ti, ^{52}Cr, ^{53}Cr and ^{54}Fe (fig.4.4). Indeed only a close examination of the data reveals differences between the ^{12}C and ^{13}C scattering. The ^{13}C data have a slightly faster initial drop in $(d\sigma_{e\ell}/d\sigma_R)$ with increasing energy, around D=10.5 fm. This small difference can be explained by noting that ^{13}C, with a loosely bound neutron has a larger number of open transfer channels for the same centre of mass energy. On the other hand, the ^{16}O and ^{18}O scattering on a common target are clearly different (fig.4.5). For ^{18}O scattering, the ratio $(d\sigma_{e\ell}/d\sigma_R)$ has a gradual deviation from unity, starting at a relatively large apsidal distance, while for ^{16}O the deviation is very sudden and occurs at a smaller D. This difference is attributed to the prolific number of open channels available in the ^{18}O case, particularly the inelastic and the low Q-value transfer reaction which are strongly populated at relatively large D. Also the two neutrons attached to the ^{16}O core make ^{18}O physically larger (Si70) and hence the nuclear ion-ion interaction becomes measurable for a relatively large D.

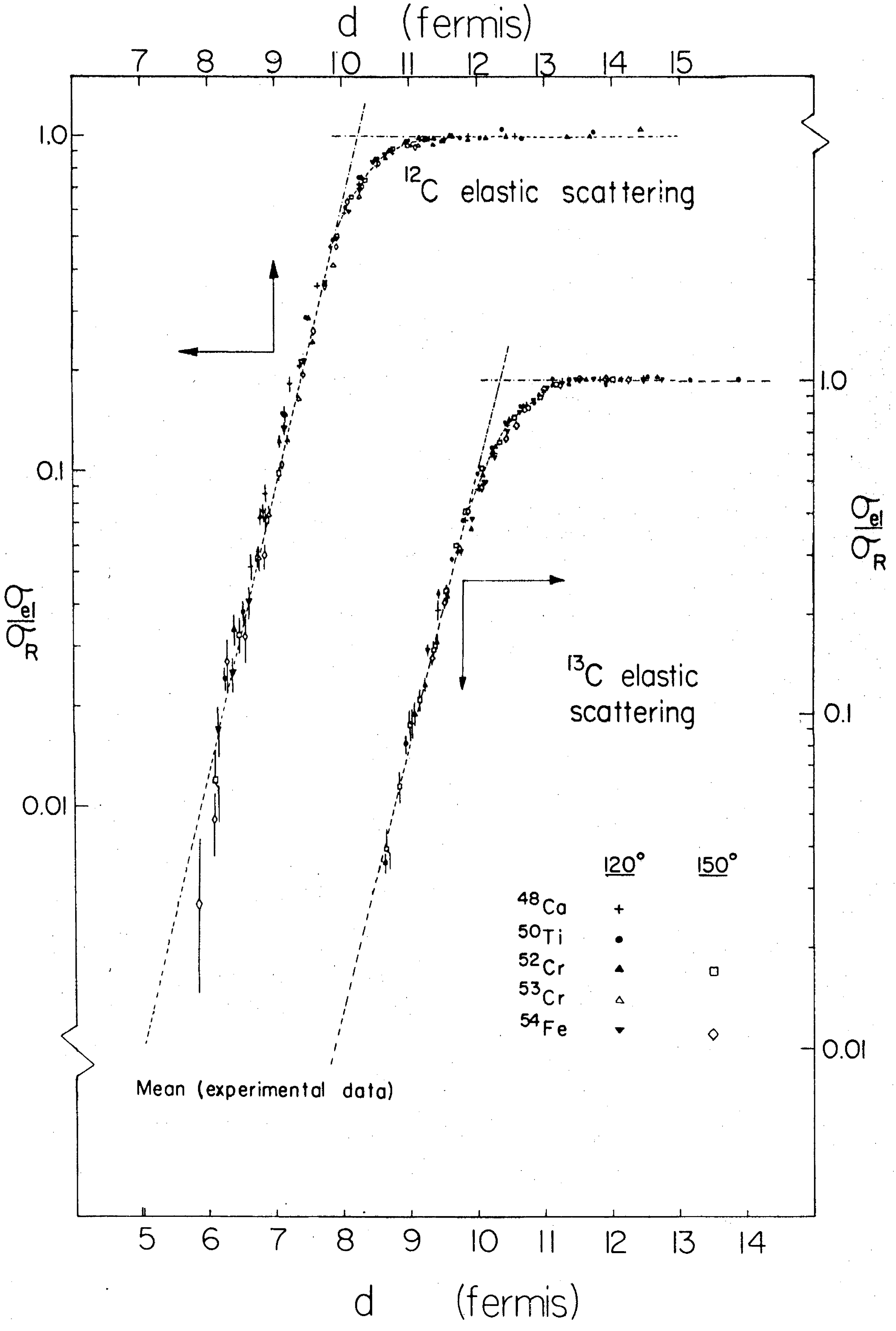

Fig.4.4 Ratio of elastic to Rutherford cross-section as a function of D.

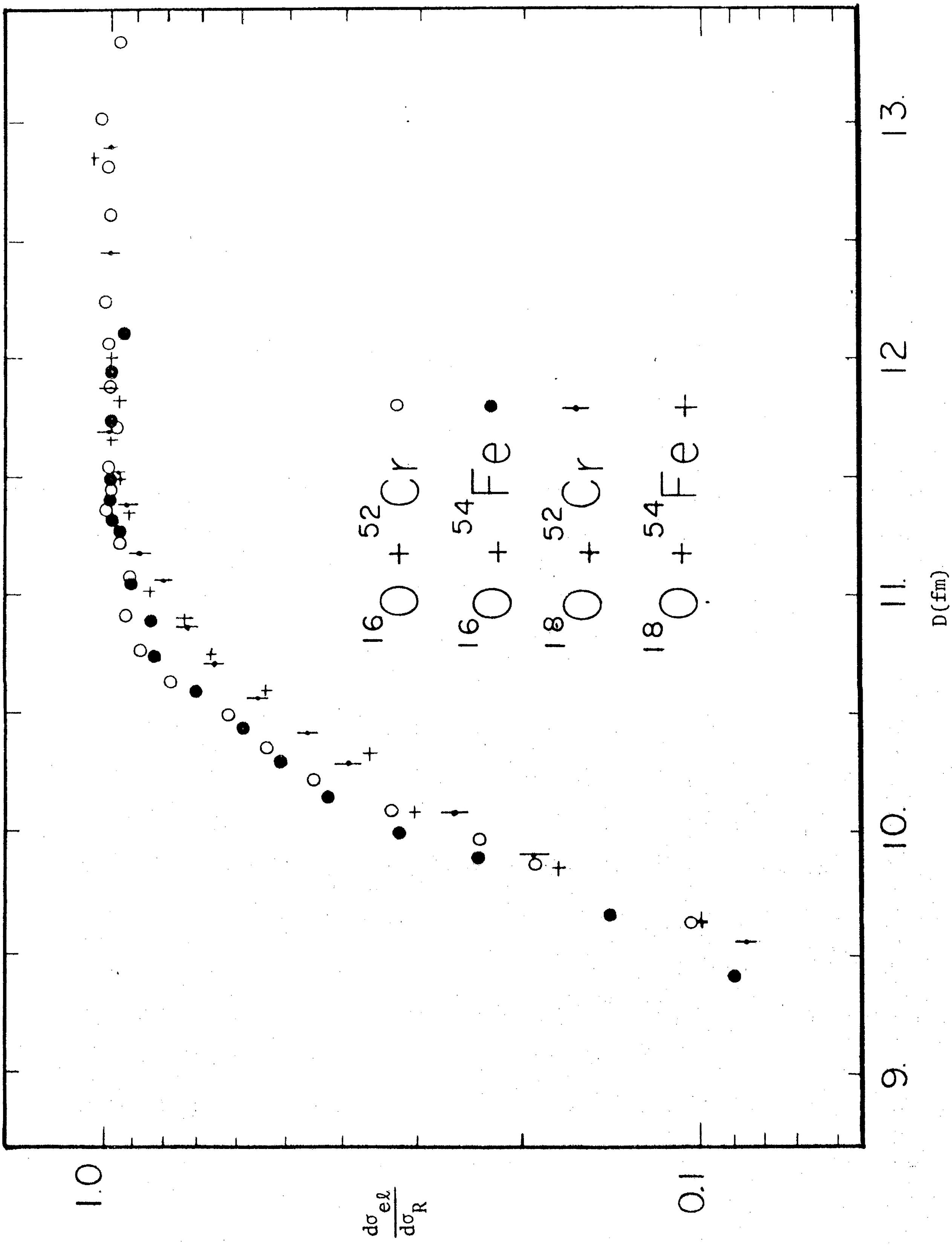

Fig.4.5 Ratio elastic to Rutherford cross-section as a function of D.

4.1.3 Optical Model

The effective potential $\tilde{V}(r)$ used in the OM analysis was the sum of the Coulomb $\tilde{V}_c(r)$ (2.1) and nuclear potential $\tilde{V}_N(r)$ (2.5). For $\tilde{V}_N$ there are six parameters (V_o, r_o, a, W_o, r'_o, a'), whilst only one is necessary for $\tilde{V}_c$, namely r_c. With this parameterisation the occurrence of ambiguities is well recognised. Often continuous as well as discrete sets of parameters will give equally good fits to the data. The most familiar of these is the depth versus radius continuous ambiguity, otherwise known as Igo ambiguity (Ig58).

It is interesting to discuss the Igo ambiguity since it demonstrates an important aspect of heavy ion scattering. Consider the real potential $\mathbb{R}e\ \tilde{V}_N$, displayed in fig.4.6 together with its evaluated ($d\sigma_{e\ell}/d\sigma_R$), both plotted as a function of apsidal distance D. As shown, the region which primarily determines the elastic cross-section is the extreme tail of the nuclear potential.

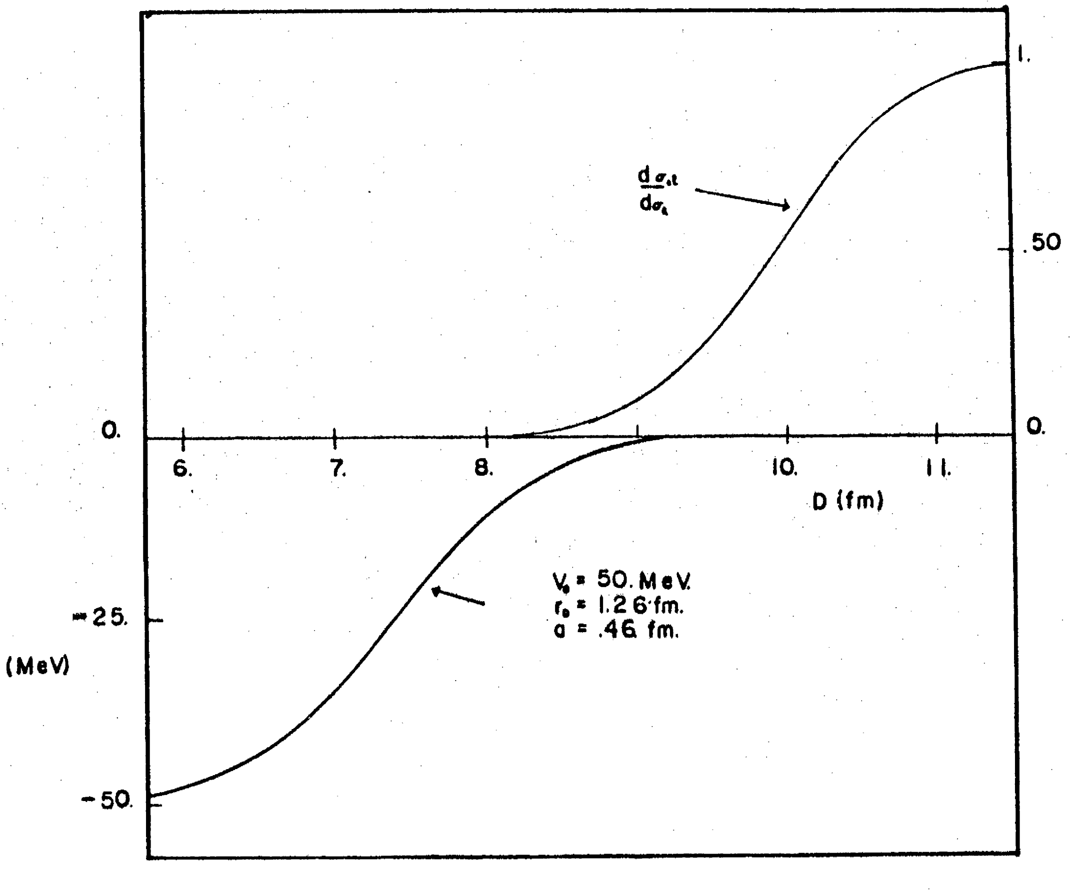

Fig.4.6

Obviously this happens because of strong absorption; projectiles which venture into distances of separation smaller than $\simeq 8$ fm are effectively absorbed into the compound nucleus and non-elastic channels. For such large r, $\tilde{V}_N$ is well approximated by

$$V_N(r) \simeq V_0 \exp(R/a) \exp(-r/a) + i\, W_0 \exp(R'/a') \exp(-r/a') \qquad 4.2$$

So with fixed values of a, a' and a wide range of values for (V_0,R), (W_0,R') such that $K = V_0 \exp(R/a)$, $K' = W_0 \exp(R'/a')$ are constant, the potentials will have the same tail and hence reproduce the same elastic scattering.† Excitation functions calculated for two such potentials are shown in fig.4.7. The difference at high incident energy occurs because the lower ℓ partial waves do sample the potentials where they are significantly different. Thus measurement of elastic scattering to small values of $(d\sigma_{e\ell}/d\sigma_R)$ is desirable to narrow the range of Igo ambiguities. Continuous ambiguities involving the diffuseness parameter a also occur. Acceptable fits to the elastic data can be obtained for different pairs (a,V_0) as demonstrated by Obst *et al* (Ob72). The point to be stressed from the above is that elastic scattering at energies about the Coulomb barrier are sensitive only to the potential tail.

Detailed studies (Sa74, Mo76) of the OM for heavy ions have shown that elastic scattering measurements can only determine the magnitude of the real potential in a narrow region ($\simeq 1$ fm) about the strong absorbing radius $D_{\frac{1}{2}}$. ($D_{\frac{1}{2}}$ can be defined as the apsidal distance for a classical Coulomb orbit which has the same angular momentum $L_{\frac{1}{2}}$ as the partial wave for which the transmission coefficient $T_{L_{\frac{1}{2}}}$ is ½.) The value of $D_{\frac{1}{2}}$ is approximately 1.5 $(A_T^{\frac{1}{3}} + A_P^{\frac{1}{3}})$ fm (Sa74). These

---

†The parameters K, K' are called Igo Constants.

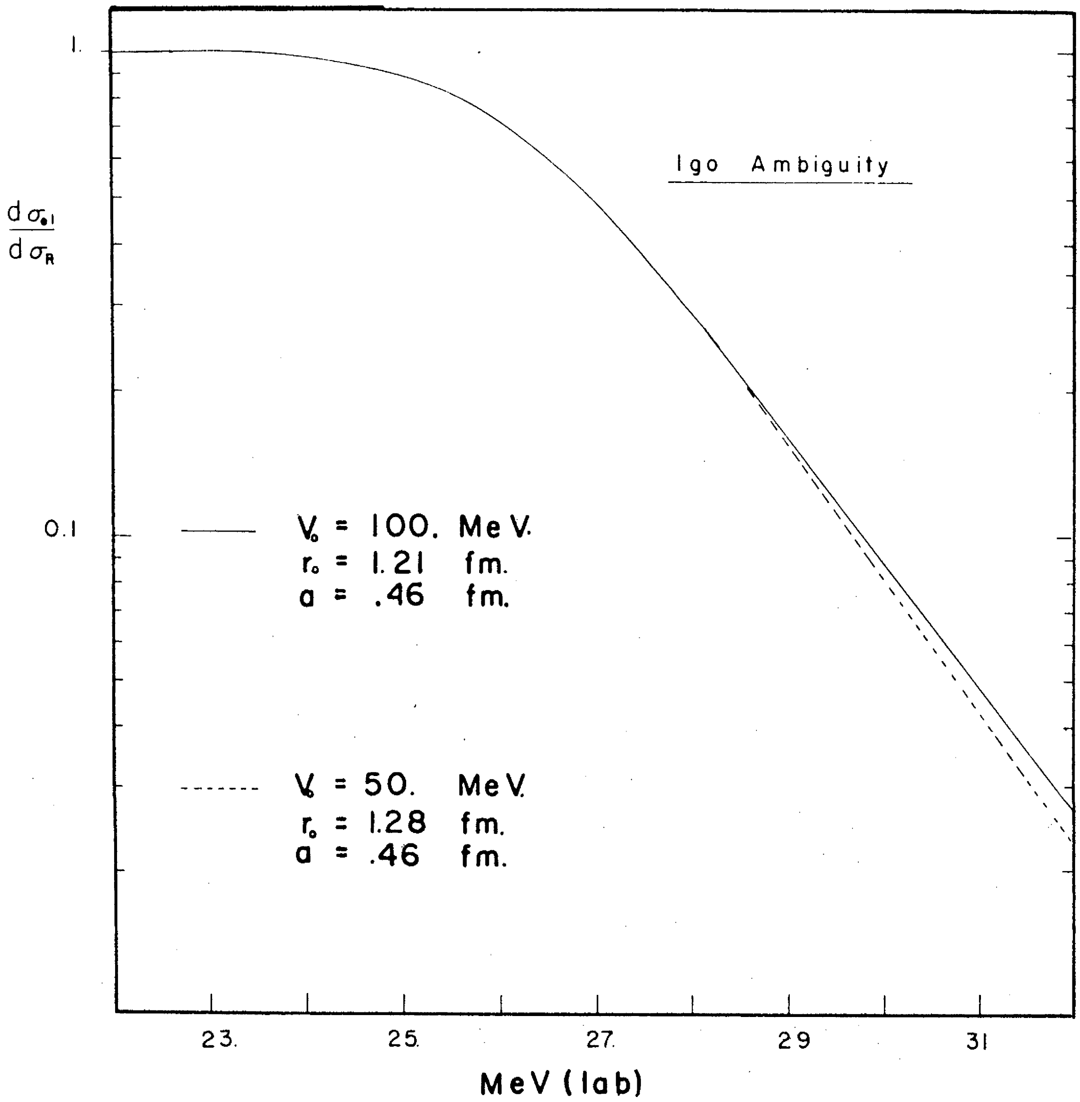

Fig.4.7 Two optical model sets with the same Igo constants and imaginary potentials (W_o = 5 MeV, r_o' = 1.21 fm, a' = 0.46 fm) for ^{12}C + ^{52}Cr.

studies also indicate that only broad limits can be placed on the values of the diffuseness parameters.

4.1.4 The Nuclear Potential $\tilde{V}_N$

In this section an attempt is made to give a physical insight into the effects of using a complex nuclear potential. In a classical description, the effect of $\mathbb{R}_e\ \tilde{V}_N$ on a pure Coulomb orbit is demonstrated in fig.4.2. Particles which have a sufficiently high bombarding energy are pulled in by the attractive nuclear force, and thus sample a larger part of the imaginary potential. Clearly, therefore, increasing the strength of $\mathbb{R}\mathrm{e}\ \tilde{V}_N$ or $\mathrm{Im}\ \tilde{V}_N$ about $D_{\frac{1}{2}}$ will reduce the elastic cross-section. This result can be expressed using the semi-classical equation (Br72)

$$\left(\frac{d\sigma_{e\ell}}{d\sigma_R}\right) \equiv P_{ABS} = \exp\left[-\frac{2}{\hbar}\int_{-\infty}^{\infty}\mathrm{Im}\ \tilde{V}_N(r(t))dt\right] \tag{4.3}$$

where r(t) is the separation between centres of the ions at time t, and is determined by solving the classical equations of motion for a particle moving in a field $\tilde{V}_c(r) + \mathbb{R}\mathrm{e}\ \tilde{V}_N(r)$. From the above equation, a strong $\mathbb{R}\mathrm{e}\ \tilde{V}_N$ results in a closer collision, hence P_{ABS} is small and for a larger $|\mathrm{Im}\ \tilde{V}_N|$ the same effect is produced. This indicates that the parameters which define the real and imaginary potentials are coupled (La74).

In the quantum mechanical description the calculated excitation functions are very sensitive to changes in V_o, r_o or a and depend only slightly on changes in W_o, r'_o and a' (fig.4.8). Thus the real potential is well determined by the elastic scattering while the imaginary potential is poorly defined. Also increasing any of the parameters is accompanied by an increase in the magnitudes of $\mathbb{R}\mathrm{e}\ \tilde{V}_N$ or $\mathrm{Im}\ \tilde{V}_N$ at $D_{\frac{1}{2}}$ and

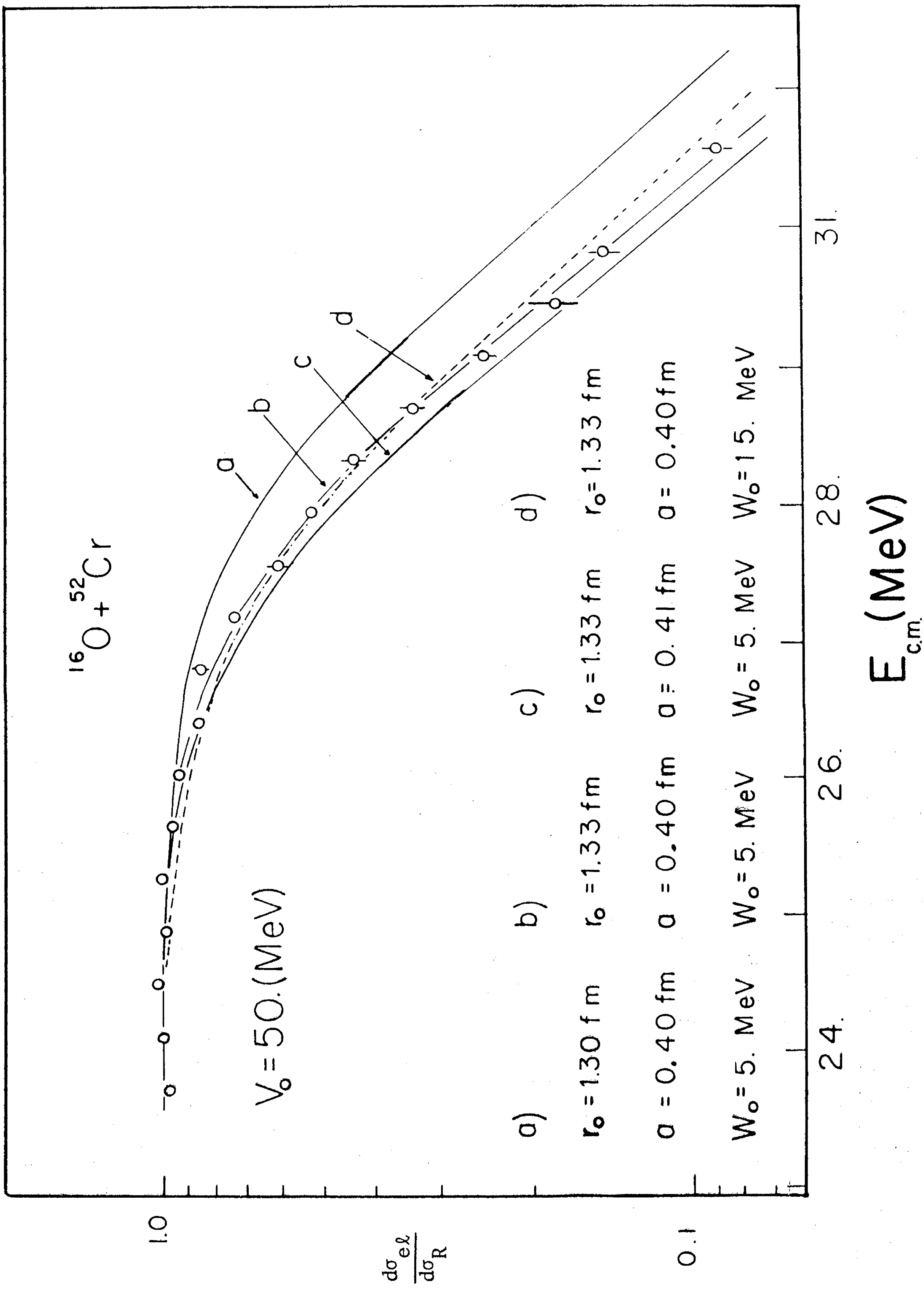

Fig.4.8 Sensitivity of the calculated ($d\sigma_{e\ell}/d\sigma_R$) to changes in the optical parameters using the code GENOA. ($r_o' = 1.33$ fm for all cases).

results in a lowering of $(d\sigma_{e\ell}/d\sigma_R)$, as predicted by the semi-classical model. A quantum mechanical effect not taken into account by the semi-classical description is that the imaginary potential not only absorbs but reflects flux (La74). The reflective part is generally small and can simulate the repulsive component of the ion-ion potential due to Pauli's exclusion principle.[†] Also, in the quantum mechanical description, when the imaginary potential is removed or made very small, the resultant excitation functions or angular distributions have very large and rapid oscillations. Since the elastic data is structureless, an imaginary component in $\tilde{V}_N$ is therefore necessary.

4.1.5 Optical Model Analysis

The OM analysis of the elastic data consisted in systematically varying the optical potential parameters until a minimum value of χ^2 is obtained;

$$\chi^2 = \frac{1}{\sum_j n_j} \sum_{i,j}^{\substack{j=n \\ i=n_j}} \left(\frac{\sigma_{exp}(E_i,\theta_j) - \sigma_t(E_i,\theta_j)}{\Delta\sigma_{exp}(E_i,\theta_j)} \right)^2 \qquad 4.4$$

where $\sigma_t(E_i,\theta_j)$ and $\sigma_{exp}(E_i,\theta_j)$ are the theoretical and experimental elastic cross-sections at an angle θ_j and energy E_i, $\Delta\sigma_{exp}(E_i,\theta_j)$ is the absolute error, n_j is the number of experimental points in the excitation function at an angle θ_j and n is the number of angles. The OM global search code Genoa (Pe) was used to generate the fits. Fifty partial waves were used for all the calculations and increasing the number to 80 did not make any significant difference to the final result. It is worth noting that the computing time necessary to fit excitation functions is considerably greater than that for angular distributions since the phase

---

[†] although the real potential has a large reflective component.

shifts have to be generated for each energy.

Most heavy ion elastic data is analysed using a fixed geometry for the real and imaginary potentials, i.e. $r_o = r'_o$ and $a = a'$ (Ba75, Th76, Wi75). Imposing these conditions leaves four free parameters (V_o, r_o, a, W_o) and since V_o and r_o are related by the Igo relationship (4.2) one of them is generally fixed. There is no theoretical justification for using this prescription, however preliminary studies using different geometries for the real and imaginary potentials did not give better values of χ^2.

Two types of fixed geometry searches were conducted:

(a) V_o was fixed and (r_o, a, W_o) varied, and

(b) (V_o, W_o) were fixed and (r_o, a) varied.

The starting parameters for each search were V_o = 50 MeV, r_o = 1.2 fm, a = 0.55 fm and W_o = 5 MeV (or 45 MeV). These parameters are average sets obtained from the literature for projectile and targets in the same mass region. To justify fixing V_o at 50 MeV for all the searches a study was conducted, where V_o was increased in 10 MeV steps between 20 MeV and 180 MeV and for each value of V_o, (r_o, a, W_o) were allowed to vary to obtain a minimum χ^2. Because of the large amount of computer time required to perform such a study, only the elastic scattering of ^{12}C and ^{13}C on ^{50}Ti were so analysed. The minimum χ^2 changed insignificantly for V_o between 30 and 130 MeV. Values of V_o outside this range resulted in an increased value of the minimum χ^2.

The Coulomb parameter r_c was varied between 1.1 and 1.3 with insignificant change in the value of χ^2 and was therefore set at 1.2 fm.

The results of searches (a) are given in tables 4.1(a) and 4.2(a), and the graphical variation of the parameters with mass number are shown in fig.4.9y. The fits to the ^{12}C and ^{13}C elastic scattering data using parameter sets in table 4.1(a) are shown on fig.4.2. There are three striking features about the optical parameters;

(i) r_o increases and a decreases with target mass number A_T (fig.4.9y),

(ii) the imaginary potential is weak relative to the real potential, $W_o/V_o \approx 0.12$ and

(iii) there is no distinct difference between the parameters for ^{12}C and ^{13}C scattering.

The OM fits to the oxygen elastic scattering data are shown in fig.4.1 and the parameters used are given in table 4.2(a). Unlike the sets for ^{12}C and ^{13}C scattering, the ^{18}O parameters have a large imaginary potential relative to those for ^{16}O.

The optical parameters obtained from searches (b) are given in tables 4.1(b) and 4.2(b). This search is very similar to the previous one except that the imaginary depth W_o was also fixed. For the carbon analysis W_o was set at 5 MeV. The extracted parameters for r_o and a (table 4.1(b)) show similar variation with A_T as in search (a) (fig.4.9x) except for ^{48}Ca + ^{13}C where fixing W_o = 5 MeV has made r_o relatively large and a relatively small. Comparing the minimum χ^2 with those of search (a) showed that they are not significantly different, hence the additional constraint of fixing W_o does not change the quality of the fits. This result is attributed to the insensitivity of the data to the strength of the imaginary potential. The values of r_o and a vary from those obtained in search (a) and indicate that the real and imaginary potentials are coupled.

TABLE 4.1(a)

Optical Model Parameters from the Three Free Parameter Searches

		V_o(MeV)	r_o(fm)	a(fm)	W_o(MeV)
1a	$^{12}C + ^{48}Ca$	50.0	1.24	0.50	3.4
2a	$^{13}C + ^{48}Ca$	50.0	1.23	0.54	22.3
3a	$^{12}C + ^{50}Ti$	50.0	1.23	0.51	7.9
4a	$^{13}C + ^{50}Ti$	50.0	1.25	0.49	7.0
5a	$^{12}C + ^{52}Cr$	50.0	1.28	0.45	2.9
6a	$^{13}C + ^{52}Cr$	50.0	1.30	0.42	3.5
7a	$^{12}C + ^{53}Cr$	50.0	1.28	0.45	3.2
8a	$^{12}C + ^{54}Fe$	50.0	1.28	0.43	3.0
9a	$^{13}C + ^{54}Fe$	50.0	1.30	0.43	3.2

TABLE 4.1(b)

Optical Model Parameters from the Two Free Parameter Searches

		V_o(MeV)	r_o(fm)	a(fm)	W_o(MeV)
1b	$^{12}C + ^{48}Ca$	50.0	1.21	0.53	5.0
2b	$^{13}C + ^{48}Ca$	50.0	1.33	0.41	5.0
3b	$^{12}C + ^{50}Ti$	50.0	1.25	0.49	5.0
4b	$^{13}C + ^{50}Ti$	50.0	1.25	0.49	5.0
5b	$^{12}C + ^{52}Cr$	50.0	1.27	0.46	5.0
6b	$^{13}C + ^{52}Cr$	50.0	1.30	0.43	5.0
7b	$^{12}C + ^{53}Cr$	50.0	1.28	0.46	5.0
8b	$^{12}C + ^{54}Fe$	50.0	1.28	0.44	5.0
9b	$^{13}C + ^{54}Fe$	50.0	1.32	0.41	5.0

TABLE 4.2(a)

Optical Model Parameters from the Three Free Parameter Searches

		V_o(MeV)	r_o(fm)	a(fm)	W_o(MeV)
1a	$^{16}O + ^{52}Cr$	50.0	1.26	0.50	8.3
2a	$^{18}O + ^{52}Cr$	50.0	1.30	0.45	22.5
3a	$^{16}O + ^{54}Fe$	50.0	1.25	0.52	2.0
4a	$^{18}O + ^{54}Fe$	50.0	1.37	0.35	9.5

TABLE 4.2(b)

Optical Model Parameters from the Two Free Parameter Searches

		V_o(MeV)	r_o(fm)	a(fm)	W_o(MeV)
1b	$^{16}O + ^{52}Cr$	50.0	1.33	0.40	5.0
2b	$^{18}O + ^{52}Cr$	50.0	1.25	0.50	45.0
3b	$^{16}O + ^{54}Fe$	50.0	1.24	0.54	5.0
4b	$^{18}O + ^{54}Fe$	50.0	1.33	0.39	45.0

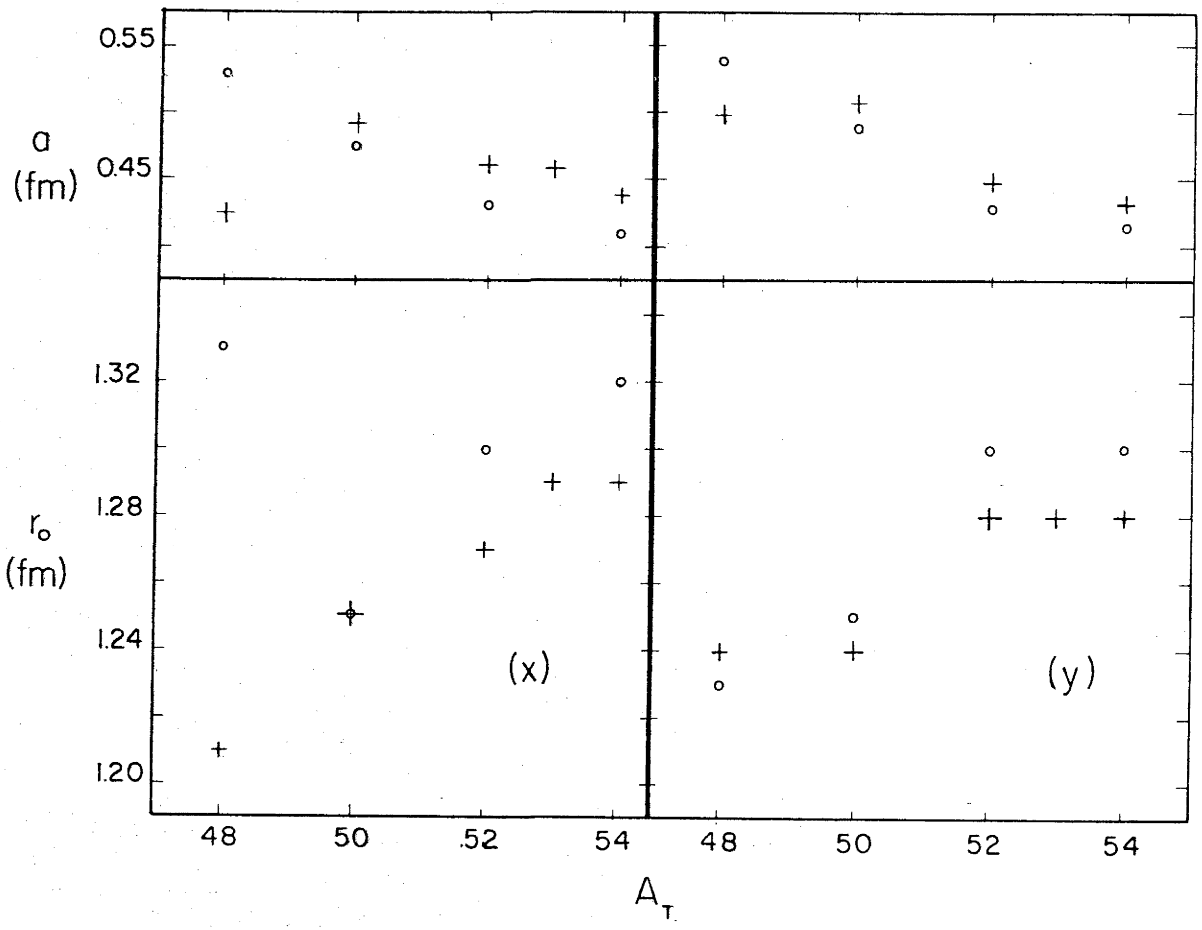

Fig.4.9 Variation of the parameters r_o and a with A_T for (x) two parameter searches and for (y) three parameter searches (+, ^{12}C) (o, ^{13}C).

For the analysis of the ^{18}O scattering data, unlike that of ^{16}O, fits could not be obtained with W_o = 5 MeV. However by setting W_o at a relatively large value of 45 MeV good fits were obtained. Once again the χ^2 for the oxygen scattering are as good as for the previous search and the parameters (r_o, a) are similar to the ones in table 4.2(a).

The results of these fits are indistinguishable from those of figures 4.1 and 4.3.

4.2 INELASTIC SCATTERING

4.2.1 Foreword

In the following section the inelastic data is described in a semi-classical context and analysed using DWBA calculations with collective form factors. The principle aim of this study is to determine if the calculations can reproduce the excitation functions induced by the carbon and oxygen isotopes. The success of the theory is judged by how well it can reproduce the different shapes of the excitation functions and if the extracted deformation strengths β_N are consistent with those obtained for other reactions. Also, below the Coulomb barrier model independent B(E2)'s are extracted.

4.2.2 Semi-Classical Description of the Inelastic Data

The results of the inelastic scattering measurements to the first 2^+ states of ^{52}Cr (1.434 MeV) and ^{54}Fe (1.409 MeV) induced by ^{12}C, ^{13}C, ^{16}O and ^{18}O are shown in figs.4.10. The excitation functions have similar gross structure; for low incident energies, the cross-section increases with energy and is well described by pure Coulomb excitation. The

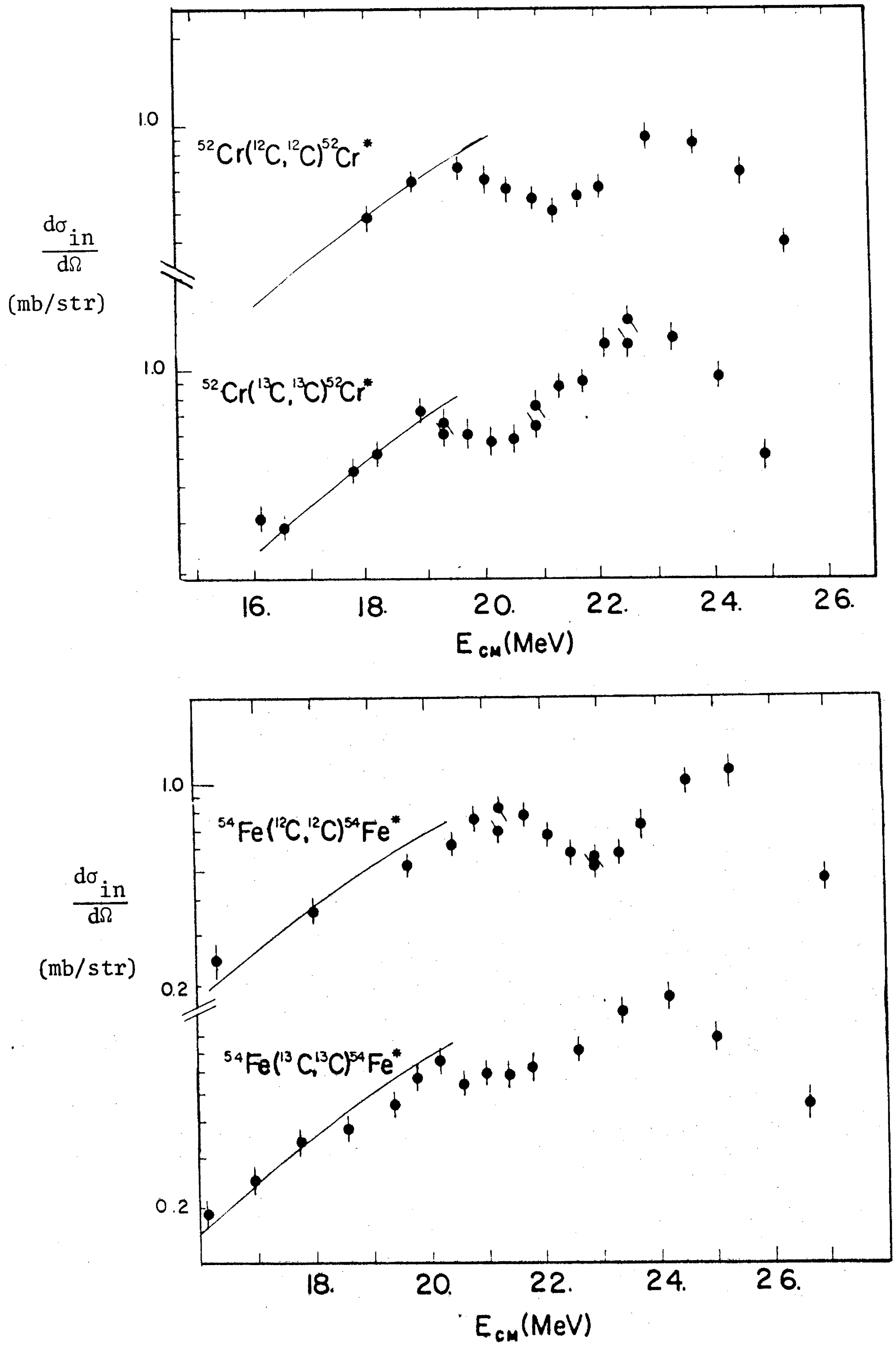

Fig.4.10a Inelastic excitation functions at 120° (Lab). The fully drawn curves are pure Coulomb excitation cross-sections calculated using the code COULEX (Wi66).

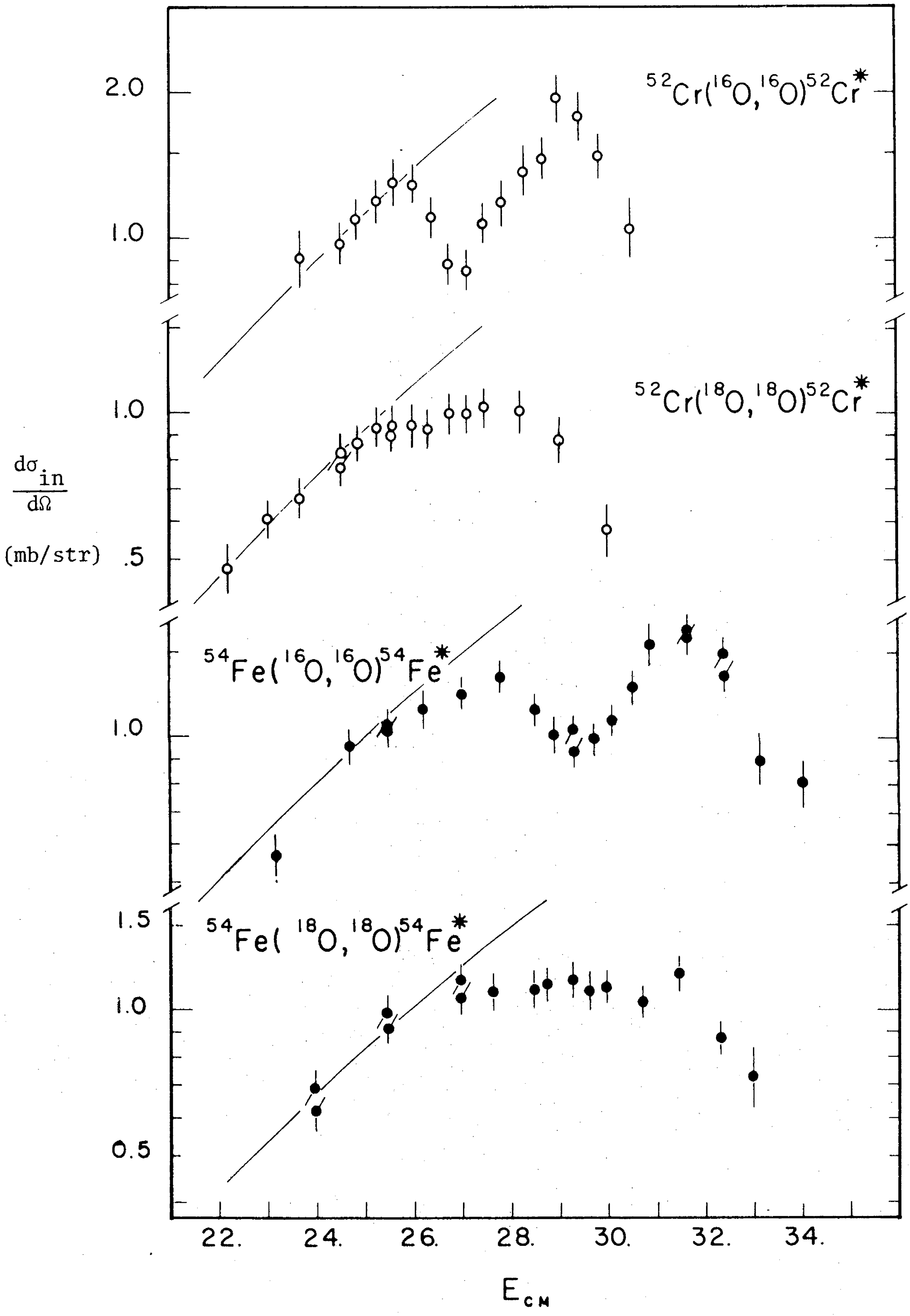

Fig.4.10b Inelastic excitation functions at 120° (Lab). The fully drawn curves are pure Coulomb excitation cross-sections calculated using the code COULEX (Wi66).

curves shown in figures 4.10 are calculated using the code COULEX (written by Winter and de Boer (Wi66)) which calculates the pure Coulomb excitation cross-sections. For higher bombarding energies the cross-section goes through a minimum, rises to a second maximum and finally drops rapidly with energy. The dip in the excitation functions is called *the Coulomb-nuclear interference minimum.* This interference phenomenon has been observed with projectiles as light as protons (Le68) and as heavy as ^{32}S (Re75) on a large range of targets. Published measurements are either in the form of angular distributions at forward angles (Co76, Be76, Sa68) or excitation functions (Ch73, Re75, Vi72). As with elastic scattering, forward angle measurements at high incident energies generally exhibit complex interference patterns apart from the nuclear-Coulomb minimum (Re75, Vi76). This arises because inelastically scattered particles travelling along different classical trajectories are deflected by the combined Coulomb and nuclear fields, to the same angle of observation (fig.4.2).

The ^{18}O induced inelastic scattering data have an interference minimum which is not as pronounced as for the other reactions. Such flat distributions in the region of the minimum have been reported by Rehm *et al* (Re75) for the reactions ^{60}Ni(^{18}O,^{18}O)^{60}Ni* (2^+, 1.434 MeV) and ^{90}Mo(^{18}O,^{18}O)^{90}Mo* (2^+, 1.148 MeV) and by Ulfine *et al* (Ul72) for ^{70}Ge(^{18}O,^{18}O)^{70}Ge* (2^+, 1.04 MeV). These measurements were performed at back angles and for energies close to the Coulomb barrier. Further, this is to be compared with the excitation functions at back angles for ^{70}Ge(^{16}O,^{16}O)^{70}Ge* (2^+, 1.04 MeV) (Ul72), ^{58}Ni(^{16}O,^{16}O)^{58}Ni* (2^+, 1.45 MeV) (Ch73) and the ^{12}C, ^{13}C and ^{16}O inelastic data presented here, where the minimum is well pronounced. Thus the shape of the ^{18}O induced inelastic scattering is independent of target and can only be associated with the ^{18}O projectile.

In first order perturbation the semi-classical amplitude for inelastic scattering is proportional to

$$\int_0^{\infty} dt(A_\ell^c F_\ell^c(r(t)) + A_\ell^N F_\ell^N(r(t)))\cos(\frac{\Delta Et}{\hbar} + m\phi(t)) \qquad 4.6a$$

where $A_\ell^c F_c^\ell$ and $A_\ell^N F_N^\ell$ are the Coulomb (2.44) and nuclear (2.35) reduced matrix elements. $(r(t), \phi(t))$ describe the Coulomb trajectory in the focal co-ordinate system with time t, ℓ is the angular momentum transfer with z-projection m and ΔE is the excitation energy. Equation (4.6a) can be written as

$$(a_c(D) + a_N^R(D)) + i\, a_N^I(D) \qquad 4.6b$$

where a_c is the corresponding Coulomb amplitude and a_N^R and a_N^I are the real and imaginary components of the nuclear amplitude. Plots of the various amplitudes as a function of D are shown in fig.4.11 and are very similar to the variation with r for corresponding form factors. The amplitudes a_c and a_N^R are of opposite sign because the Coulomb potential is repulsive while the nuclear potential is attractive. Also a_N^R varies exponentially with D while a_c varies like $1/D^3$, and this reflects the short and long range nature of the two interactions. Further, a_N^I decreases exponentially with D but generally has a much smaller magnitude than a_N^R, since $W_o/V_o \ll 1$. The probability P_m for excitation a particular substate m is proportional to

$$(a_c(D) + a_N^R(D))^2 + (a_N^I(D))^2 \qquad 4.7$$

and the inelastic differential cross-section given by (Br74)

$$\frac{d\sigma_{in}}{d\Omega} = \sum_m P_m(D) \frac{d\sigma_{e\ell}}{d\Omega} = \sum_m P_m(D) \frac{d\sigma_R}{d\Omega} P_{ABS} \qquad 4.8$$

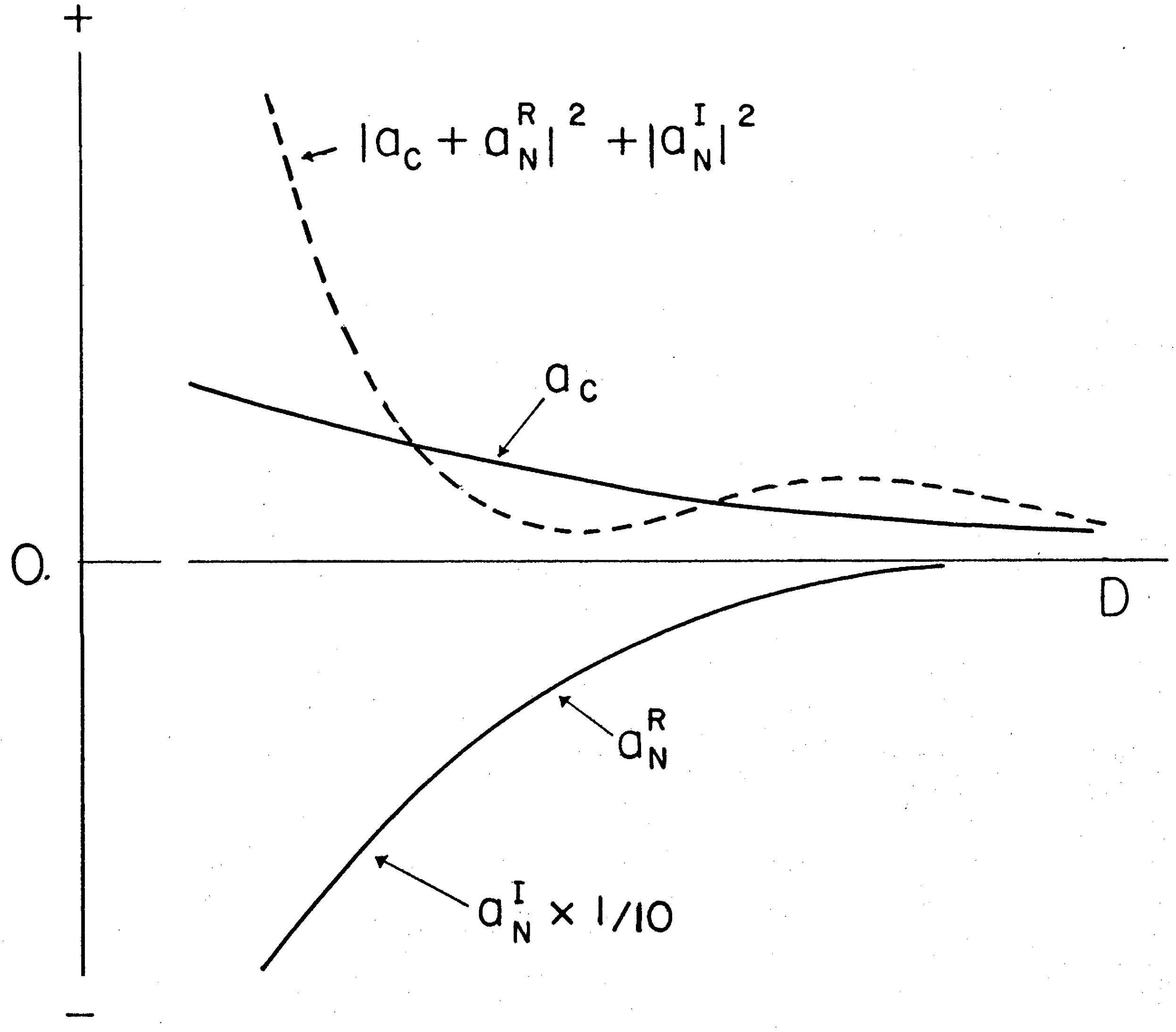

Fig.4.11 a_c, a_N^R, a_N^I and probability for excitation (4.7) as a function of D.

Thus, for large $D \simeq 12$ fm (fig.4.11), the nuclear amplitudes are relatively small, so the excitation process is dominantly through the long range electromagnetic interaction. Since P_{ABS} is essentially unity for large D, $(d\sigma_{in}/d\Omega)$ follows pure Coulomb excitation, as observed experimentally. At smaller D, $(a_c + a_N^R)^2$ goes through a sharp minimum then rises rapidly with D. The corresponding minimum in $\sum_m P_m(D)$ is less pronounced since the amplitude from the different substates do not reach their minimum at the same D and because of the incoherent contribution from $(a_N^I(D))^2$. The absorption probability P_{ABS} does not vary rapidly in the region of the dip, so the semi-classical calculated cross-section displays the experimentally observed minimum, hence the name, "Coulomb-nuclear interference". The final monotonic drop in the experimental cross-section arises because the elastic and inelastic flux is mostly channelled into multistep processes or compound nucleus formation for small D. This effect is taken into account in the semi-classical model by P_{ABS}.

By plotting the inelastic data as a function of D, interesting similarities and differences in the excitation functions are displayed. The inelastic scattering data of ^{12}C or ^{13}C from ^{52}Cr is essentially the same as that for ^{54}Fe (fig.4.12). A similar effect is observed for the oxygen scattering (fig.4.13). This implies that the shape of the excitation functions are not strongly dependent on the target (Ch73).

Of particular interest is the difference between the plots for ^{12}C and ^{13}C scattering (fig.4.14), and even more so for ^{16}O and ^{18}O (fig.4.15) The minima for ^{12}C and ^{13}C occur at D = 10.2 fm and D = 10.7 fm respectively and while the ^{12}C minima are well defined, those for ^{13}C are shallow. What is surprising about this result is that the optical potentials for the corresponding elastic scattering are very similar

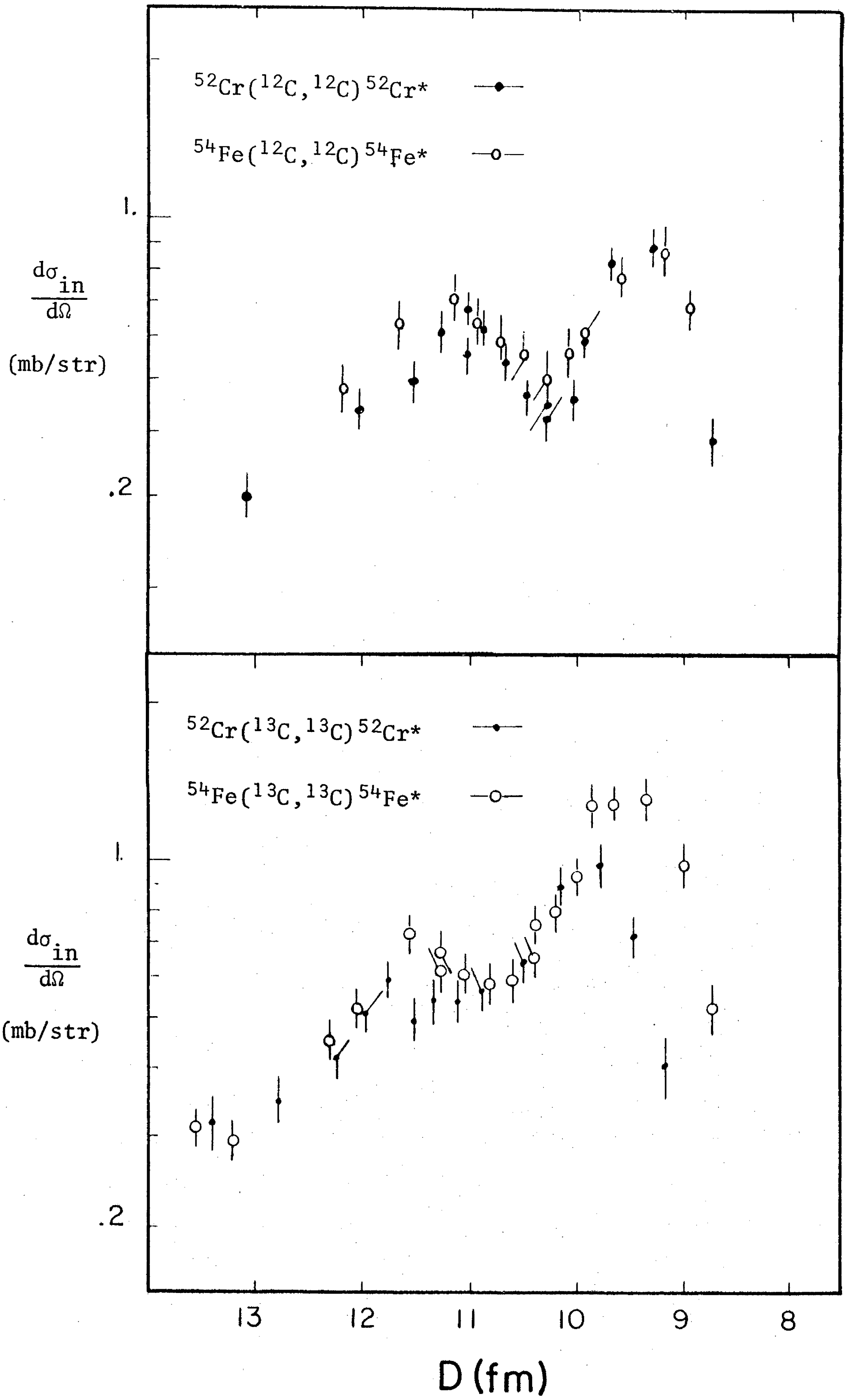

Fig.4.12 Carbon inelastic scattering data plotted as a function of D.

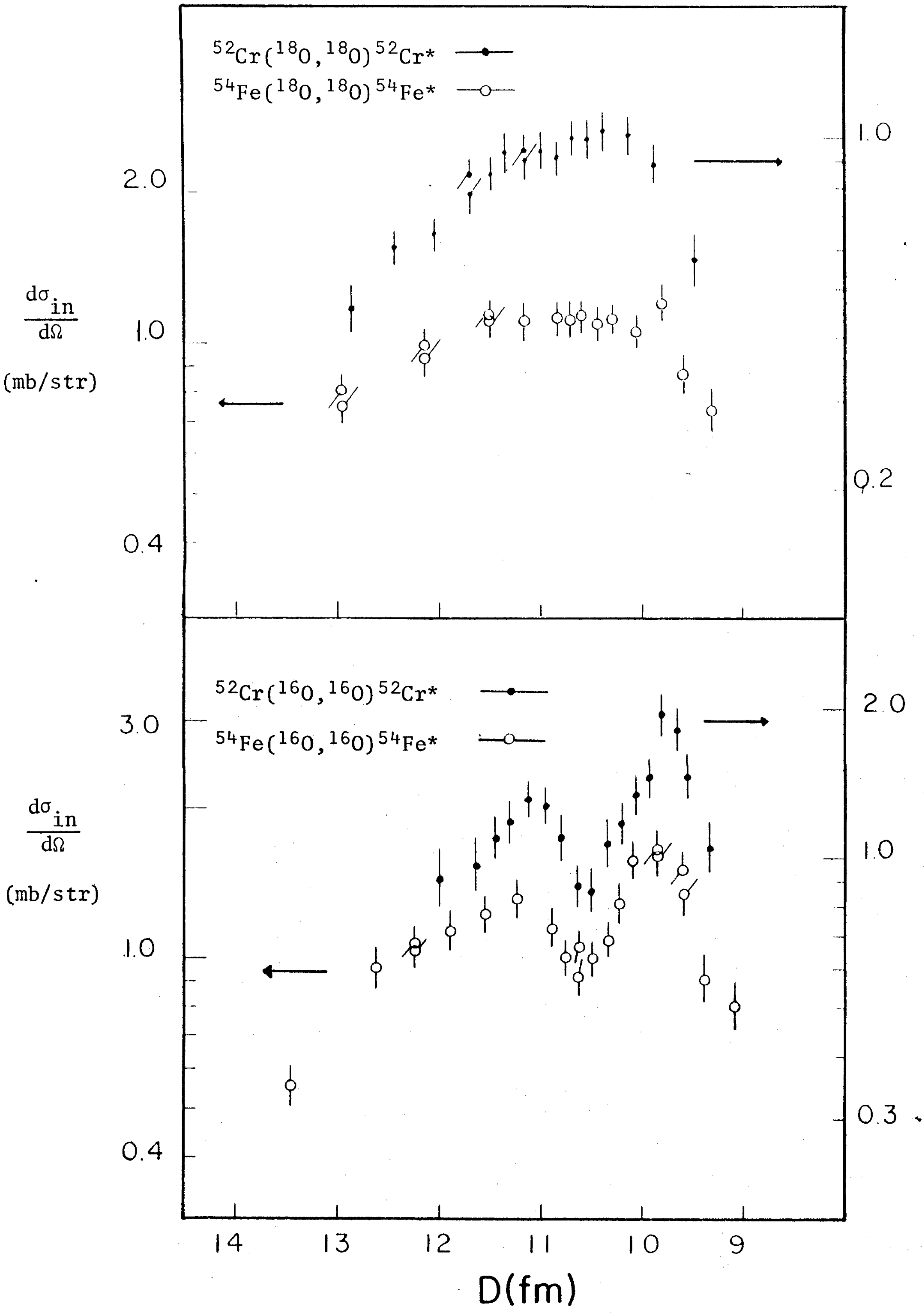

Fig.4.13 Oxygen inelastic scattering data plotted as a function of D.

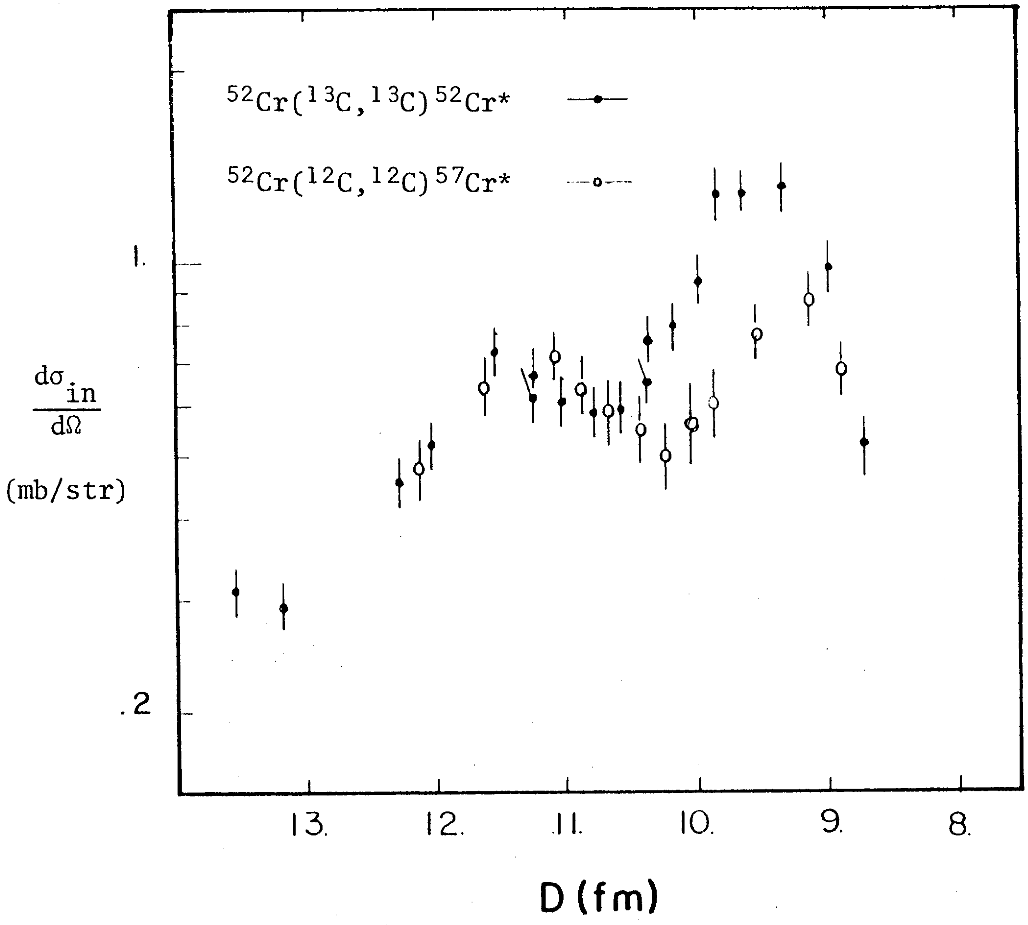

Fig.4.14

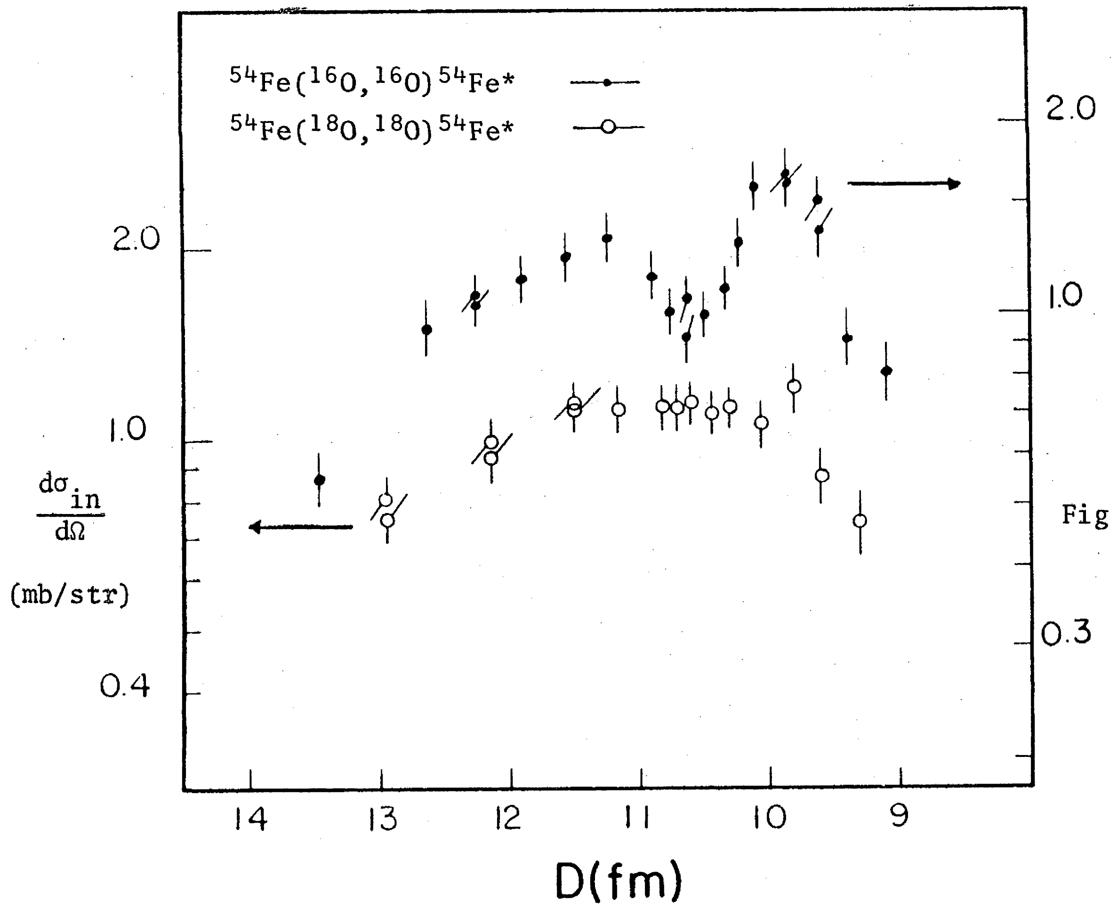

Fig.4.15

Fig.4.14 & 4.15 Inelastic scattering data plotted as a function of D.

(table 4.1). Since these effects are independent of the target and the Coulomb interaction is not sensitive to the charge distributions of the projectiles (†), then these differences can only be attributed to different reaction mechanisms for ^{12}C and ^{13}C scattering. Alternatively, since inelastic scattering is very sensitive to the effective ion-ion potential (Ch73), the interference patterns reflect very different OM potentials.

The differences in the inelastic excitation functions induced by ^{16}O and ^{18}O are clearly demonstrated in fig.4.15. The very shallow minimum observed for ^{18}O scattering can be ascribed to the large absorptive potential required to fit the elastic data (table 4.2). For $W_o \approx V_o$, a_N^I contributes very strongly to $\sum_m P_m$, hence the interference minimum becomes less pronounced, but $(d\sigma_{in}/d\Omega)$ (4.8) still retains the characteristic rise and fall at low and high incident energy.

Finally it must be stressed that the nuclear ion-ion interactions occur far beyond the nuclear surface $R \approx 1.25\ (A_T^{\frac{1}{3}} + A_P^{\frac{1}{3}}) \approx 8$ fm. Thus these reactions can be called peripheral or gent-le collisions.

4.2.3 DWBA Analysis

The principle difficulty in evaluating the inelastic scattering cross-sections is the long range behaviour of the Coulomb form factor. This implies that to evaluate the transition amplitude (2.26b) the integration has to be performed to about 100 fms and many partial waves (≈200) have to be included. These calculations were performed with the code NUCSCAT (Sa73) which computes the contributions from the first Lc partial waves using conventional methods. For higher partial waves, where the nuclear contributions are negligible, the amplitudes are computed using a recursion relation (Sa73). The code was shown to

---

† Chapter 2

reproduce the results from COULEX (Wi66) to better than 3% for pure Coulomb excitation.

A necessary condition which must be satisfied by the data for the first order Born approximation to be applicable is that the ratio of measured inelastic to elastic cross-sections $(d\sigma_{in}/d\sigma_{e\ell})_{EXP}$ must be small (He75). This condition is sometimes overlooked in the literature (Ch73), although it is difficult to assign an upper bound for $(d\sigma_{in}/d\sigma_{e\ell})_{EXP}$, for which the approximation is justified, without performing laborious coupled-channel calculations. The data presented here partially fulfills this condition. For bombarding energies above about 25 MeV (cm) for carbon and 30 MeV (cm) for oxygen, $(d\sigma_{in}/d\sigma_{e\ell})_{EXP}$ are high (fig.4.16) and the DWBA results are considered doubtful.

Another consideration is whether the first excited states of ^{52}Cr and ^{54}Fe have a large enough collective component to justify the use of a collective form factor. This is verified by noting that the B(E2) values have a large single particle (sp) strength (11.7 sp units for ^{52}Cr (2^+, 1.434 MeV) and 8.7 sp units for ^{54}Fe (2^+, 1.409 MeV)) and that the energy spacings of the first few excited states show a strong vibrational character. Also the angular distributions for ^{52}Cr$(\alpha,\alpha)^{52}$Cr* (2^+, 1.434 MeV) and ^{54}Fe$(\alpha,\alpha')^{54}$Fe* (2^+, 1.409 MeV) (Br70) have been successfully analysed using collective form factors.

To calculate DWBA inelastic cross-sections with a collective form factor the following parameters are required; the optical potential set (V_o,r_o,a,W_o,r_o', a') (2.5), the Coulomb potential charge radius R_c (2.1), the target charge radius $R_T^{c'}$ (2.46), B(E2) and S defined by

$$S = \beta_N/\beta_c \qquad 4.9$$

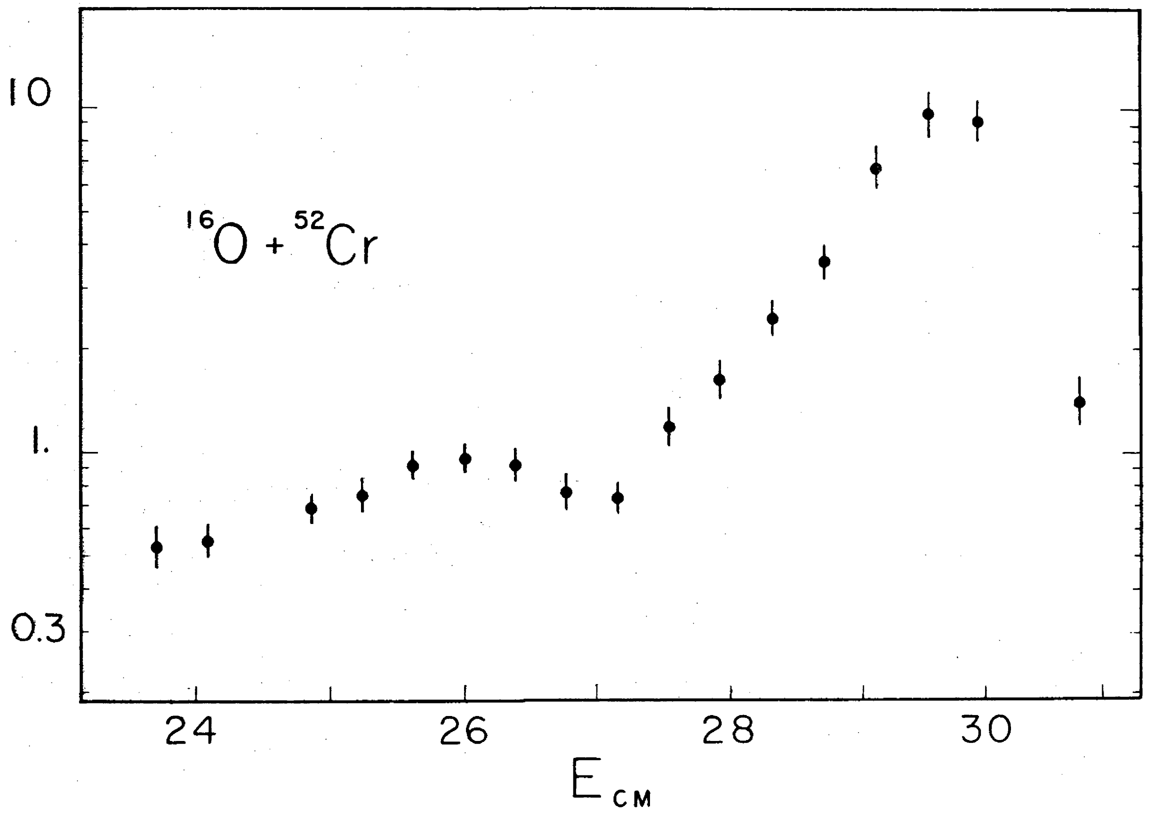

Fig.4.16 Ratio of inelastic to elastic cross-sections as a function of energy (cm).

where $\beta_N = \beta_\ell$ (2.34) and $\beta_c = \beta_\ell^c$ (2.44a) are the root mean square deformations of the optical potential and charge distribution. For easy reference the collective form factor for quadrupole excitation $F_2(r)$ is restated below

$$A_2F_2(r) = A_2^cF_2^c(r) + A_2^NF_2^N(r) \qquad 4.10$$

where

$$A_2^cF_2^c(r) = \frac{-\beta_c i^\ell 3Z_PZ_Te^2}{5^{3/2}}\begin{cases}(R_T^{c'})^2/r^3, & r \geqslant R_T^{c'}\\ r^2/(R_T^{c'})^3, & r < R_T^{c'}\end{cases}$$

and

$$A_2^NF_2^N(r) = \frac{-\beta_N}{5^{\frac{1}{2}}}\, i^\ell \left(\frac{-V_o}{a}\frac{R_T\ \exp(\chi)}{(1+\exp(\chi))^2}\ \ \frac{-i\ W_o}{a'}\frac{R'_T\ \exp(\chi')}{(1+\exp(\chi'))^2}\right)$$

$$\chi = (r-R)/a\ , \qquad R_T = r_oA_T^{\frac{1}{3}}$$

$$\chi' = (r-R')/a'\ , \qquad R'_T = r'_oA_T^{\frac{1}{3}}$$

$$\beta_N = \beta_cS = \frac{4\pi(B(E2))^{\frac{1}{2}}}{3\ Z_Te\ R_T^{c'2}}\,S$$

Theoretically to obtain fits to the inelastic data there are only two free parameters, the B(E2) and S. The optical potential $(V_o, r_o, a, W_o, r_o', a')$ is determined from the corresponding elastic scattering. The B(E2) is easy to determine since the DWBA differential cross-section is proportional to this parameter. S is extracted by systematically varying it until an optimum fit to the data is obtained. In the following two subsections the parameters which appear in (4.10) are discussed.

4.2.4 Determination of the B(E2), $R_T^{c'}$ and R_c

To extract a model independent value of the B(E2) (Chapter 2) the theory is compared with the experimental points only at low energies, where the nuclear contributions are less than 3%. The nuclear contribution is estimated with optical parameters which fit the elastic and inelastic excitation functions. The quoted B(E2) values (table 4.4, p.96) are given by the weighted mean for the considered data points and have assigned errors of typically 8%.

The values of $R_T^{c'}$ (table 4.3) for ^{52}Cr and ^{54}Fe are evaluated from expression (2.46), where $\rho_T^c(r)$ have a Wood-Saxon form with parameters from electron scattering measurements.

TABLE 4.3

Target	$R_T^{c'}$ (fm)	Wood-Saxon Parameters		Ref.
		R (fm)	a (fm)	
Cr	4.283	3.975	0.53	(Be64)
Fe	4.322	4.012	0.533	(Li72)

Varying R_c by ±10% about $R_c = 1.2\ (A_T^{\frac{1}{3}} + A_P^{\frac{1}{3}})$ produced insignificant changes (<0.1%) in the calculated inelastic cross-sections. So the value of R_c is fixed at the same value used in the OM analysis of the elastic data, $R_c = 1.2\ (A_T^{\frac{1}{3}} + A_P^{\frac{1}{3}})$ fm.

4.2.5 Sensitivity of the Inelastic Excitation Functions to S and the Optical Potential

The parameter S is introduced because the nuclear vibrational parameter β_N is not necessarily equal to that of the charge β_c (Ch73). In fact, attempts to fit the data with $\beta_N = \beta_c$ were unsuccessful. The shape of the calculated excitation functions are strongly dependent on S and (V_o, r_o, a), but only weakly so on (W_o, r_o', a') (fig.4.17).

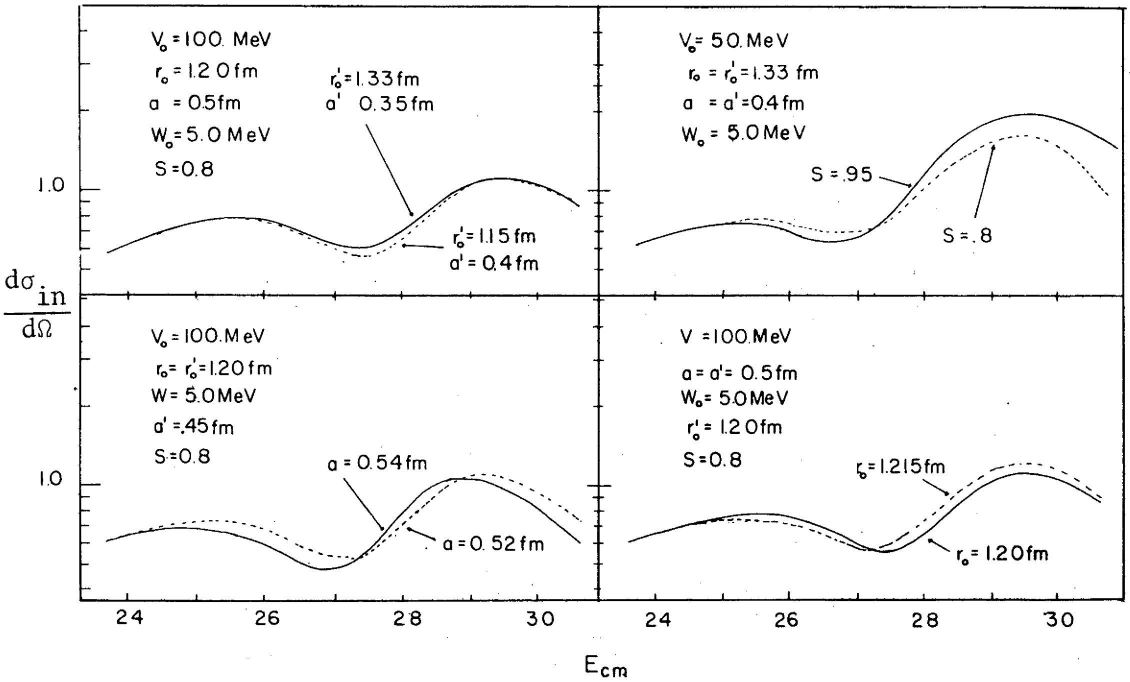

Fig.4.17 Sensitivity of the calculated ($d\sigma_{in}/d\Omega$) to changes in the optical parameters and S using the code NUCSCAT.

Thus the imaginary potential is not well determined by inelastic scattering and conversely for S and the real potential.

The parameter S scales the nuclear form factor (4.10) and hence the nuclear contributions to be calculated cross-sections. Increasing S shifts the interference minimum to a lower energy making it more pronounced, and also increases the magnitude of the second maximum (fig.4.17). A rough guide to the effects of varying the real or imaginary potential is given by the semi-classical model (4.7, 4.8). As in the case of elastic scattering, the calculated inelastic cross-sections exhibit strong oscillations when the imaginary potential is made too small.

Two optical parameter sets which are related through the Igo relationship and give equally good fits to the elastic data do not necessarily give the same results for the calculated inelastic cross-sections. Consider $\mathbb{R}\mathrm{e}\, F_N(r)$ (4.10) for large r

$$\mathbb{R}\mathrm{e}\, F_N(r) \approx \frac{-V_o\, \beta_N}{a} R_T \exp(R/a)\, \exp(-r/a) \qquad 4.11$$

Thus two sets which have a common Igo constant $K = V_o \exp(R/a)$ will not necessarily have the same magnitude for $\mathbb{R}\mathrm{e}\, F_N(r)$. A similar result is obtained for $\mathrm{Im}\, F_N(r)$. However, if S is adjusted by the ratio of the product of the depth and radius parameters of the two sets, then the ambiguity is still retained for the calculated inelastic scattering. Hence the extracted value of S can depend on the choice of optical parameters and the inelastic scattering is only sensitive to the tail of the optical potential (Mo76).

4.2.6 Analysis of the $^{52}Cr(^{13}C,^{13}C)^{52}Cr^*$ and $^{54}Fe(^{13}C,^{13}C)^{54}Fe^*$ Data

The DWBA calcuations for ^{13}C inelastic scattering with OM parameters which gave an optimum fit to the elastic data (table 4.1a) are shown in figs. 4.18 and 4.19. In both cases the low energy data is reproduced and so is the position and depth of the interference minima. However the theoretical curves overestimate the high energy points. The calculations with OM sets from the three and two free parameter searches give almost indistinguishable results. The B(E2)'s and S values extracted are shown in table 4.4 and are discussed in Chapter 5.

4.2.7 Analysis of the $^{52}Cr(^{12}C,^{12}C)^{52}Cr^*$ and $^{54}Fe(^{12}C,^{12}C)^{54}Fe^*$ Data

The DWBA predictions with appropriate OM (table 4.1) parameters for the ^{12}C inelastic data show an overall disagreement with the data

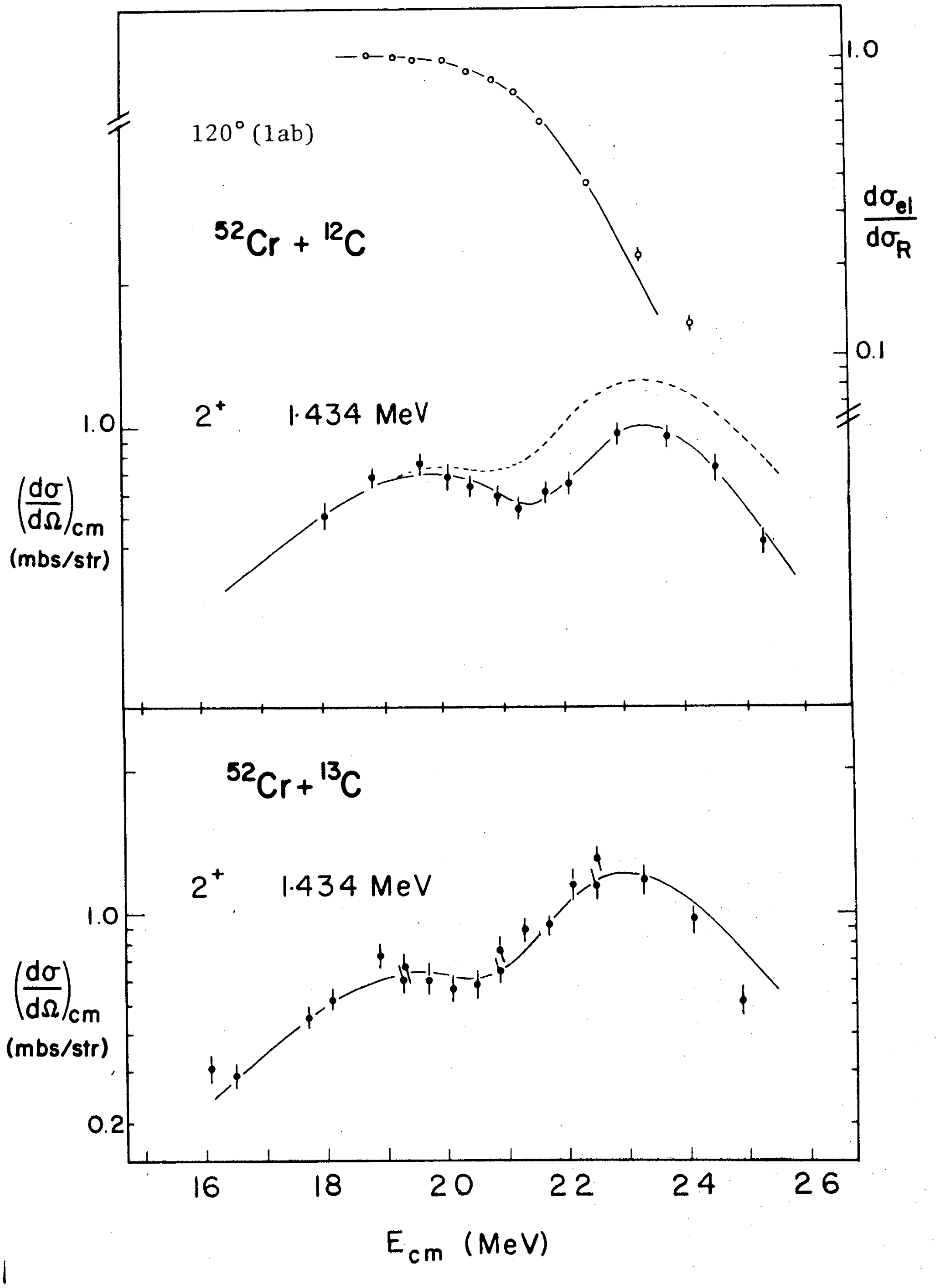

Fig.4.18 The full curves are OM and DWBA fits to the elastic and inelastic data using parameters given in table 4.4. The dashed curve was calculated with optical model set 5a (table 4.1).

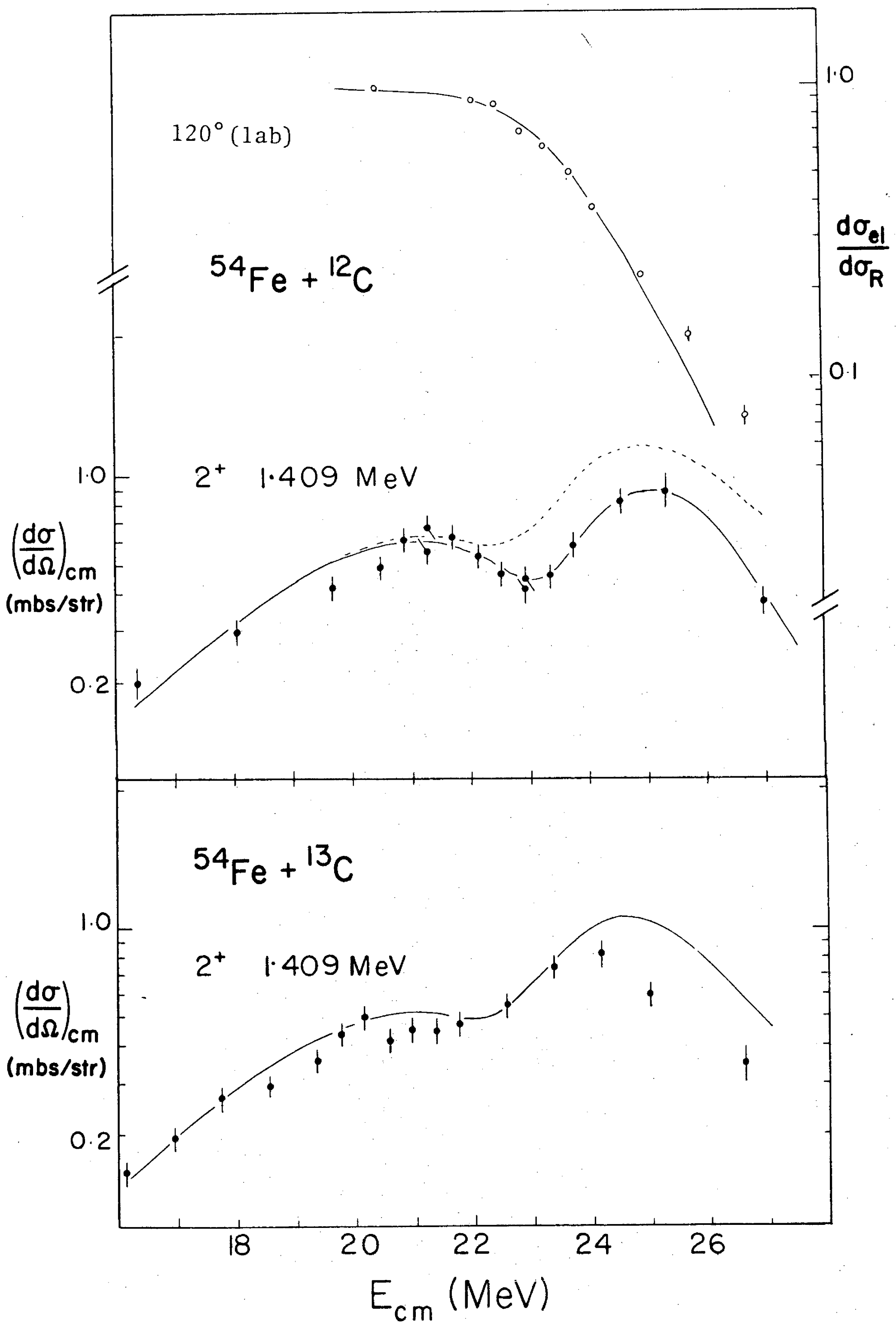

Fig.4.19 The full curves are OM and DWBA fits to the elastic and inelastic data using parameters given in table 4.4. The dashed curve was calculated with optical model set 8a (table 4.1).

where the nuclear potential plays an important role. The theoretical curves (dashed in figs. 4.18 and 4.19) were calculated with B(E2)'s and S values used for the corresponding ^{13}C inelastic scattering and reproduce only the low energy data. The discrepancy at higher energies could not be removed by varying S. This result is not surprising however, since the ^{12}C and ^{13}C inelastic excitation functions are so different in shape, yet the extracted optical parameters for the elastic scattering are very similar.

In a successful attempt to find parameter sets which reproduce both the elastic and inelastic data a grid search was conducted. For the ^{52}Cr data, r_o and a were varied in 0.03 fm step between 1.14-1.32 fm and 0.4 and 0.64 fm respectively, while the remaining parameters were fixed at V_o = 50 MeV, W_o = 5 MeV, r_o' = 1.2 fm, a' = 0.5 fm and S = 0.75. When a relatively good fit was obtained to both reactions small adjustments were made in r_o, a and a'. The optimum optical potential obtained (table 4.4), have a smaller r_o and larger a compared to the appropriate parameter sets in table 4.1. The same parameter set resulted in good fits to the ^{54}Fe(^{12}C,^{12}C)^{54}Fe and ^{54}Fe(^{12}C,^{12}C)^{54}Fe* excitation functions when S was adjusted to the value used for the ^{54}Fe(^{13}C,^{13}C)^{54}Fe* reaction.

The results of the grid search are shown by the solid curves in figures 4.18 and 4.19. The DWBA calculations reproduce the inelastic data very well for all the energy range. The fits to elastic excitation functions are relatively poor at high incident energy, however for the lower, more important energies the agreement is still quite good. The B(E2)'s used for ^{13}C scattering were found to give excellent fits to the low energy data for ^{12}C.

TABLE 4.4

Summary of Optical Potentials and Parameters Used for Inelastic Scattering Analysis

	V_o	r_o	a	W_o	r_o'	a'	B(E2) e^2 b^2	S	β_N	β_c	$\frac{\beta_N R_T}{\beta_c R_T^{c'}}$
^{52}Cr + ^{12}C	50.0	1.18	0.59	5.0	1.20	0.43	0.061 ±0.0048	0.69	0.16	0.25	0.66
^{52}Cr + ^{13}C	50.0	1.30	0.42	3.5	1.30	0.42	0.061 ±0.0048	0.69	0.16	0.25	0.72
^{54}Fe + ^{12}C	50.0	1.18	0.59	5.0	1.20	0.43	0.064 ±0.0036	0.76	0.17	0.22	0.79
^{54}Fe + ^{13}C	50.0	1.30	0.43	3.2	1.30	0.43	0.064 ±0.0036	0.76	0.17	0.22	0.88
^{52}Cr + ^{16}O	50.0	1.26	0.50	8.3	1.26	0.50	0.059 ±0.0047	0.74	0.17	0.23	0.81
^{52}Cr + ^{18}O	50.0	1.22	0.56	43.0	1.22	0.50	0.054 ±0.005	0.55	0.12	0.22	0.58
^{54}Fe + ^{16}O	50.0	1.24	0.54	5.0	1.24	0.54	0.064 ±0.0051	0.73	0.16	0.22	0.79
^{54}Fe + ^{18}O	50.0	1.22	0.56	43.0	1.22	0.50	0.060 ±0.0048	0.56	0.12	0.21	0.61

4.2.8 Analysis of the ^{52}Cr(^{16}O,^{16}O)^{52}Cr* and ^{54}Fe(^{16}O,^{16}O)^{54}Fe* Data

The DWBA calculations for these reactions reproduce the data (figs. 4.20, 4.21). The optical potentials used were 1a and 3b (table 4.2) for ^{52}Cr and ^{54}Fe respectively. The other appropriate potentials did not give as good a fit to the inelastic data. It is noticeable that for ^{52}Cr(^{16}O,^{16}O)^{52}Cr* the first maximum is underestimated by the theory and an attempt to fit this region using a grid search was unsuccessful. The extracted values of the B(E2)'s and S's are in agreement with the ones used for the corresponding carbon scattering (table 4.4).

4.2.9 Analysis of the ^{54}Fe(^{18}O,^{18}O)^{54}Fe* Data

For this reaction the optimum optical potential sets (table 4.2) only partially reproduced the inelastic data (fig.4.21, dashed curve, set 4a) (table 4.2a). So a grid search similar to the one conducted for ^{12}C scattering was performed. As demonstrated by the solid curve, the final fit to the inelastic data is superior, with only a marginal increase in the value of χ^2, from 1.4 to 1.6 for the elastic scattering data. As in the case of ^{12}C scattering, the resulting parameter set has a large a and small r_0, (table 4.4) compared to the appropriate sets in table 4.2.

The B(E2) extracted from the low energy data is in agreement with that extracted for ^{16}O scattering, however S = 0.56 is considerably smaller. Such a small value was necessary to suppress the second maximum and the filling-in of the interference minimum. In an attempt to find a value of S consistent with that for the ^{16}O data, S was varied throughout the grid search without success.

4.2.10 Analysis of the ^{52}Cr(^{18}O,^{18}O)^{52}Cr* Data

The solid curve in fig.4.20 is the DWBA calculation using the parameter set 2a (table 4.2a). Set 2b did not give a good fit. The

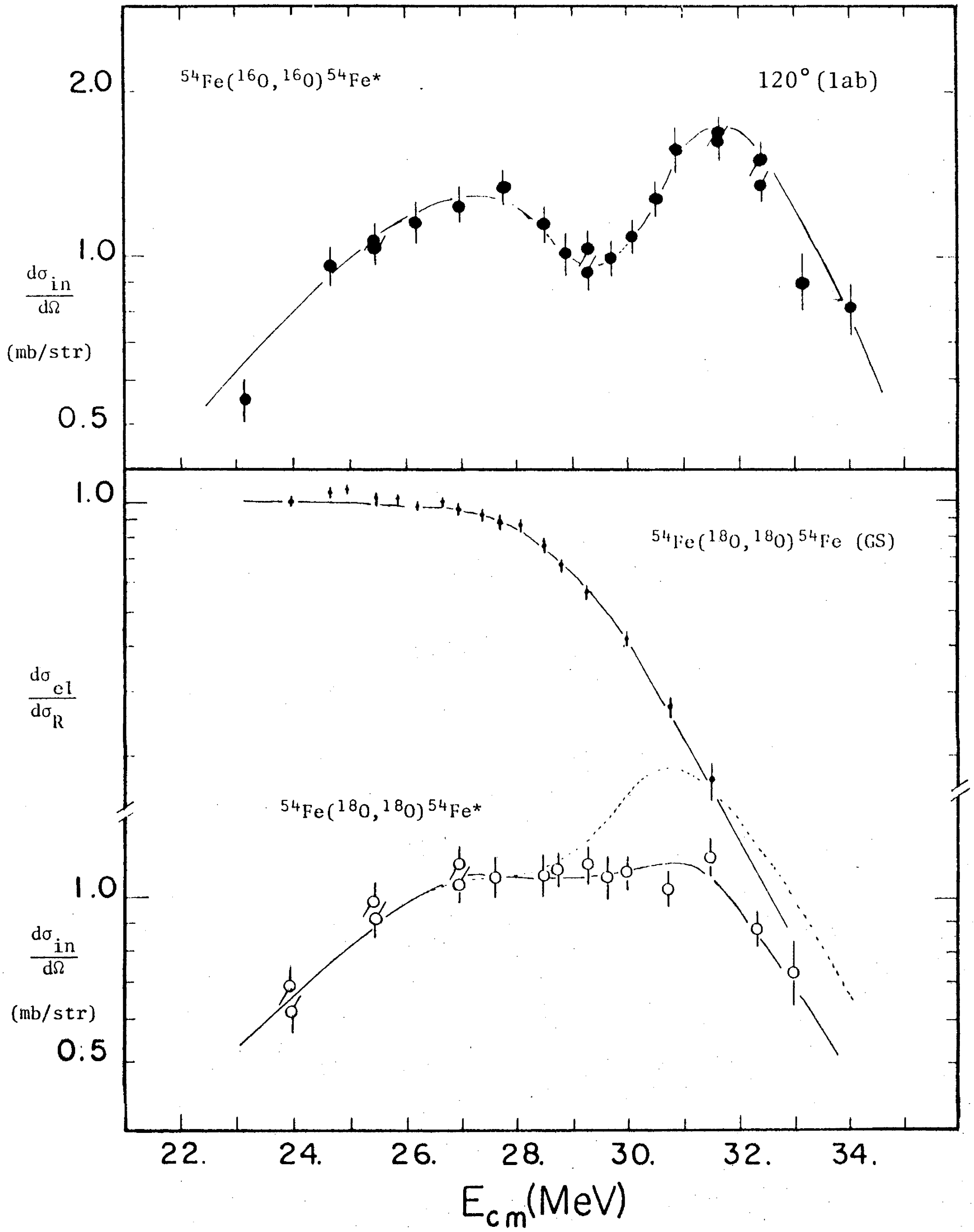

Fig.4.20 The full curves are OM and DWBA fits to the elastic and inelastic data using parameters given in table 4.4. The dahsed curve was calculated with parameter set 4a (table 4.2a).

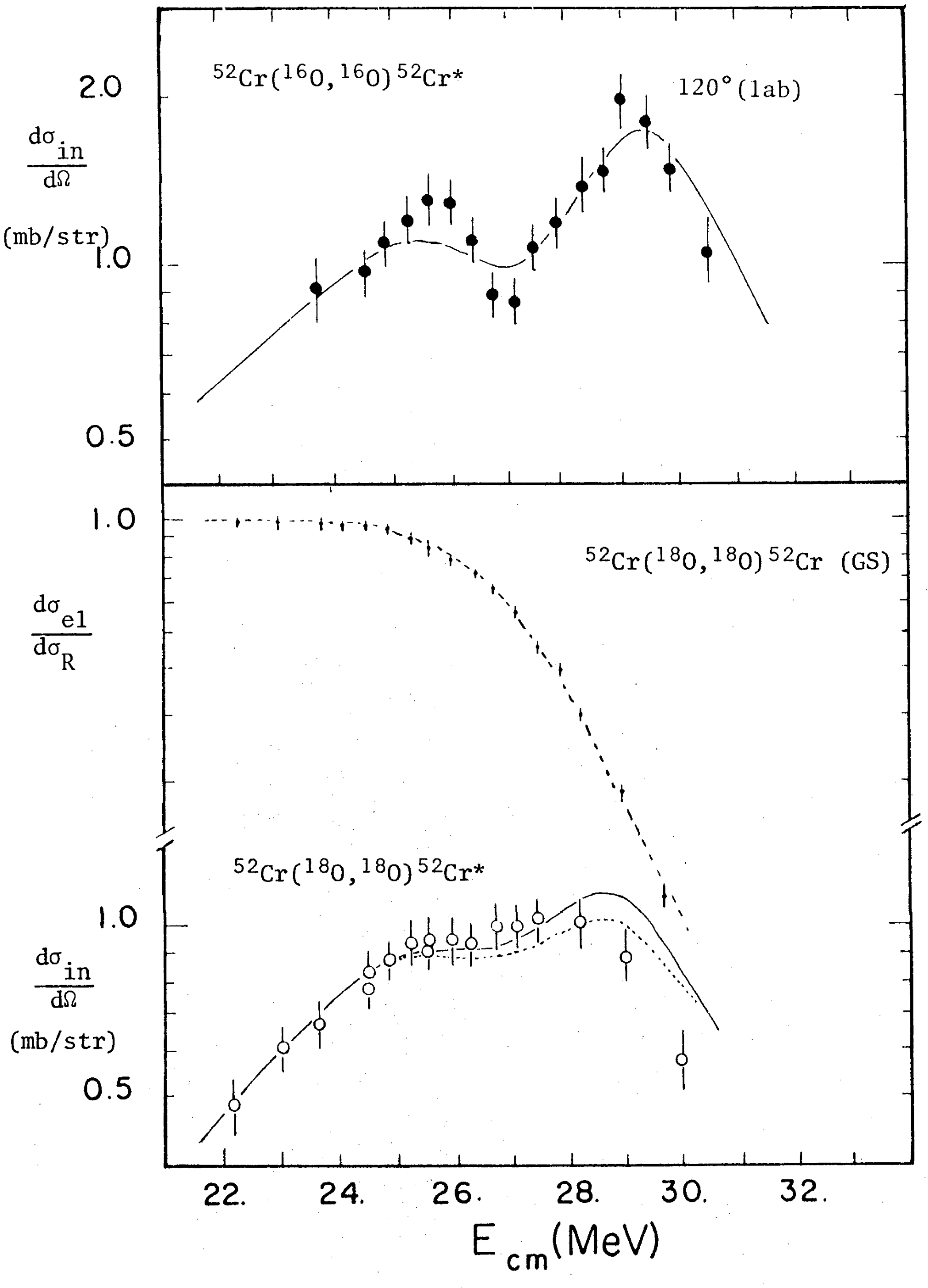

Fig.4.21 The full curves are OM and DWBA fits to the elastic and inelastic data using parameters given in table 4.4. The dashed curve was calculated with the same parameter set as for ^{18}O + ^{54}Fe (table 4.4).

TABLE 4.5

B(E2) and β_N Values from Other Work

	B(E2) $e^2\ b^2$	β_N	Reaction	Ref.
^{52}Cr	0.048±0.002		Coulex, ^{16}O	Si65
	0.061±0.015		Coulex, ^{16}O	Ad60
	0.080±0.020		Coulex, ^{16}O	Of60
	0.067±0.007		Coulex, ^{32}S	To60
		0.17	(p,p')	Fu64
		0.19	(p,p')	Be69
		0.14±0.028	(α,α')	Bu72*
^{54}Fe	0.051±0.002		Coulex, ^{16}O	Si65
	0.061		Coulex, ^{16}O	A168
		0.14	(p,p')	Fu64
		0.17	(p,p')	St64b
		0.11±0.022	(α,α')	Bu72*
		0.15	(^{16}O, ^{16}O')	Be72

*Analysed with Austern-Blair model

B(E2) used is within values extracted from the other reactions on ^{52}Cr, however the value of S = 0.55 is low compared to that for ^{16}O scattering. S had to be small, as in the case of ^{54}Fe(^{18}O,^{18}O)^{54}Fe*, to reproduce the featureless excitation function.

The dashed curves are calculated with optical parameters used for the ^{54}Fe + ^{18}O reaction and S = 0.55. The elastic and inelastic data are almost as well reproduced by this set as with set 2a.

4.2.11 The Folding Model Predictions

In this section the real part of the phenomenological potentials, $\mathbb{R}e\ \tilde{V}_N$ which give fits to the elastic and inelastic data are compared with the predictions of the folding model (Chapter 2).

The short ranged nucleon-nucleon interaction v, for simplicity, is approximated by a δ-function with adjustable strength U_o. Thus the folded potential (2.6) is given by:

$$\tilde{V}_N^F(r) = U_o \int d^3r_T\ \rho_T(r_T)\ \rho_P(|\underline{r}-\underline{r}_T|)$$

The mass distributions ρ_T (2.4) and ρ_P (2.3) are assumed to have the same shape as the charge distributions obtained from electron scattering experiments (De74) and U_o is adjusted so that $\tilde{V}_N^F(D_{\frac{1}{2}}) = \mathbb{R}_e\ \tilde{V}_N(D_{\frac{1}{2}})$.

In fig.4.22 the folding model predictions are compared with the real part of the optical potentials (table 4.4). The values of U_o used (table 4.6) vary mainly with projectile type by about 30%. This variation is expected since U_o varies rapidly with the parameters for ρ_P and ρ_T which are not accurately determined by electron scattering at the extreme tails (Jo76). Similar results for U_o were obtained by Vary *et al* (Va73). The shape of the calculated folded potentials for ^{12}C and oxygen

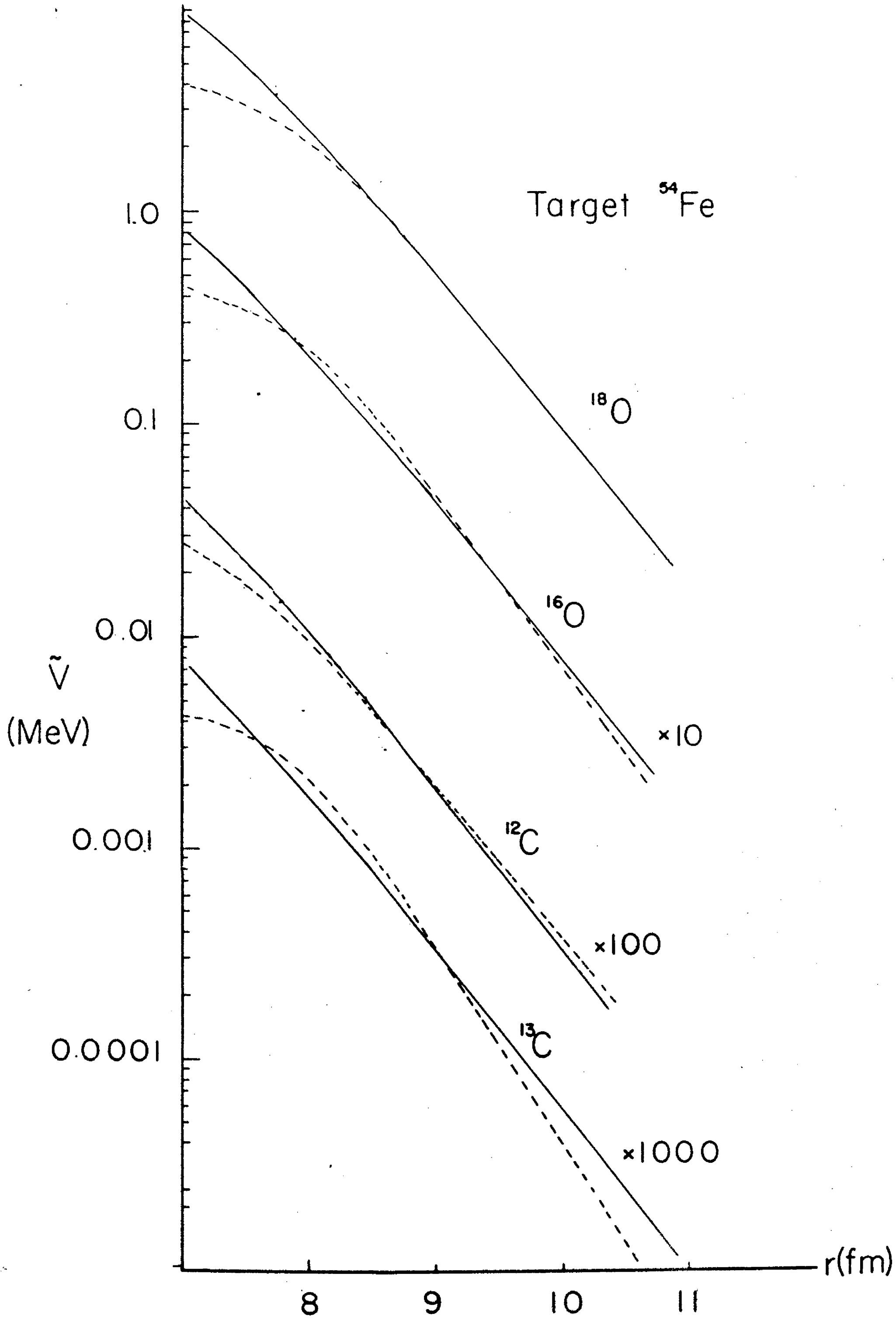

Fig.4.22 Folded potentials (solid curves) are compared to the real part of the phenomenological Wood-Saxon potentials (dashed curves). The potentials for ^{52}Cr are essentially the same.

scattering are in fair agreement with the real phenomenological potentials. However for ^{13}C, $\tilde{V}_N^F$ has a relatively small gradient, corresponding to a $\approx$ 0.58 for a Wood-Saxon potential. Also for ^{13}C scattering U_o's are abnormally high. This discrepancy would imply that ρ_p for ^{13}C is very different from that of ^{12}C. However, varying the parameters for ρ_p, through a large range of values, the folded potentials still did not reproduce the steep gradient of $\mathbb{R}e\ \tilde{V}_N$ for ^{13}C. In another attempt to correct for this inconsistency, the ^{13}C elastic and inelastic data were reanalysed with fixed $a = a' = 0.58$ and $V_o = 50$ and varying $r_o = r_o'$ and W_o, but no successful description of the data could be obtained.

An interesting result emerges when calculating the inelastic form factors F_ℓ^{FOLD} (2.37). With different values for U_o and parameter sets for ρ_p, such that the $\tilde{V}_N^F$'s have the same magnitude and gradients at $D_{\frac{1}{2}}$ as a given Wood-Saxon potential, the resulting F_2^{FOLD} have the same gradient as that given by the Wood-Saxon potential $\mathbb{R}e\ F_2^N$ (4.10) but differ in magnitude. The ratio $F_2^{FOLD}(D_{\frac{1}{2}})/\mathbb{R}e\ F_2^N(D_{\frac{1}{2}})$ varies with the different parameters and are less than unity. Clearly this implies that the deformation amplitude $R_T\beta_N$ extracted by Wood-Saxon effective potential will depend upon the shape of the incident particle. Assuming that the folded potentials overlap the real Wood-Saxon potentials in the tail, then the $R_T\beta_N/R_T^{c'}\beta_c$ (table 4.4) can be corrected for the projectile size. It is important to note that the corrected $R_T\beta_N$ refers to the amplitude of the mass deformation (†). The corrected values of $R_T\beta_N/R_T^{c'}\beta_c$ are given in table 4.6 and show better consistency with $\mathbf{R}_T\boldsymbol{\beta}_N/R_T^{c'}\beta_c$

In conclusion it is seen that in spite of the crude choice of v and mass distributions, the folded potentials approximate the real phenomenological potentials in the tail with only one free parameter. The only exception is the ^{13}C scattering.

---

† Chapter 2, p.31.

TABLE 4.6

Reaction	$D_{\frac{1}{2}}$ (fm)	U_o (MeV)	F_N^F/F_N	$\beta_N R_T/\beta_c R_T^{c'}$	Corrected $\beta_N R_T/\beta_c R_T^{c'}$
$^{12}C + ^{52}Cr$	9.4	947	0.91	0.71	0.79
$^{12}C + ^{54}Fe$	9.4	931	0.91	0.79	0.86
$^{13}C + ^{52}Cr$	9.6	1148	0.64	0.72	1.13
$^{13}C + ^{54}Fe$	9.7	1098	0.63	0.88	1.40
$^{16}O + ^{52}Cr$	9.8	882	0.71	0.81	1.14
$^{16}O + ^{54}Fe$	10.0	955	0.72	0.79	1.09
$^{18}O + ^{52}Cr$	10.0	890	0.82	0.59	0.72
$^{18}O + ^{54}Fe$	10.0	884	0.81	0.61	0.75

Also it is shown, that for a legitimate comparison to be made between mass and charge deformations, the projectile mass distribution has to be explicitly taken into account. It must be emphasised however, that this fair agreement might be fortuitous, since if a finite range nucleon-nucleon interaction (such as a Yukawa or Gaussian) were to be used a much more diffused folded potential will result (Sa74, Ba75). This, as well as the discrepancy for ^{13}C indicates that the ion-ion effective interaction might be also a function of the internal structure of the combined target and projectile system (Ei72).

4.3 SINGLE NEUTRON TRANSFER

4.3.1 Semi-Classical Description of the Transfer Data

In this section the single neutron transfer (SNT) reactions (table 4.7) measured by Parkinson (Pa74) are analysed using the full finite range (FFR) DWBA code LOLA (De73).

TABLE 4.7

Reaction	Ground State Q-value	Projectile Energy Range (MeV)
^{48}Ca(^{13}C,^{12}C)^{49}Ca (GS)	0.197	18.0 - 25.5
^{50}Ti(^{13}C,^{12}C)^{51}Ti (GS, 1.16 MeV, 2.16 MeV)	1.432	17.5 - 27.5
^{52}Cr(^{13}C,^{12}C)^{53}Cr (GS, 2.32 MeV, 3.58 MeV)	2.995	19.0 - 29.5
^{53}Cr(^{12}C,^{13}C)^{52}Cr (GS)	-2.995	25.0 - 30.0
^{54}Fe(^{13}C,^{12}C)^{55}Fe (GS)	4.353	23.5 - 31.5

The aim of this analysis is to extract spectroscopic factors and to determine if the theory is able to reproduce the transfer data for energies about the Coulomb barrier with optical parameters which reproduce the corresponding elastic and available inelastic data. The experimental technique used was similar to the one described in Chapter 3 and as documented by Parkinson (Pa74).

Each of the transfer excitation functions has the same 'bell' shape, characteristic of measurements at large angles and energies around the Coulomb barrier (Mo72, Na73). For low incident energies, where $\left(\frac{d\sigma_{e\ell}}{d\sigma_R}\right) \approx 1$, the transfer cross-section rises exponentially with energy (fig.4.23). The excitation functions peak at an energy corresponding approximately to the strong absorption radius in the elastic scattering. At higher incident energies the cross-section falls monotonically. Unlike measurements taken at more forward angles (Bo74) the excitation functions do not exhibit any fine structure. The peak cross-sections vary systematically with Q-value (fig.4.23) and occur at higher energies as

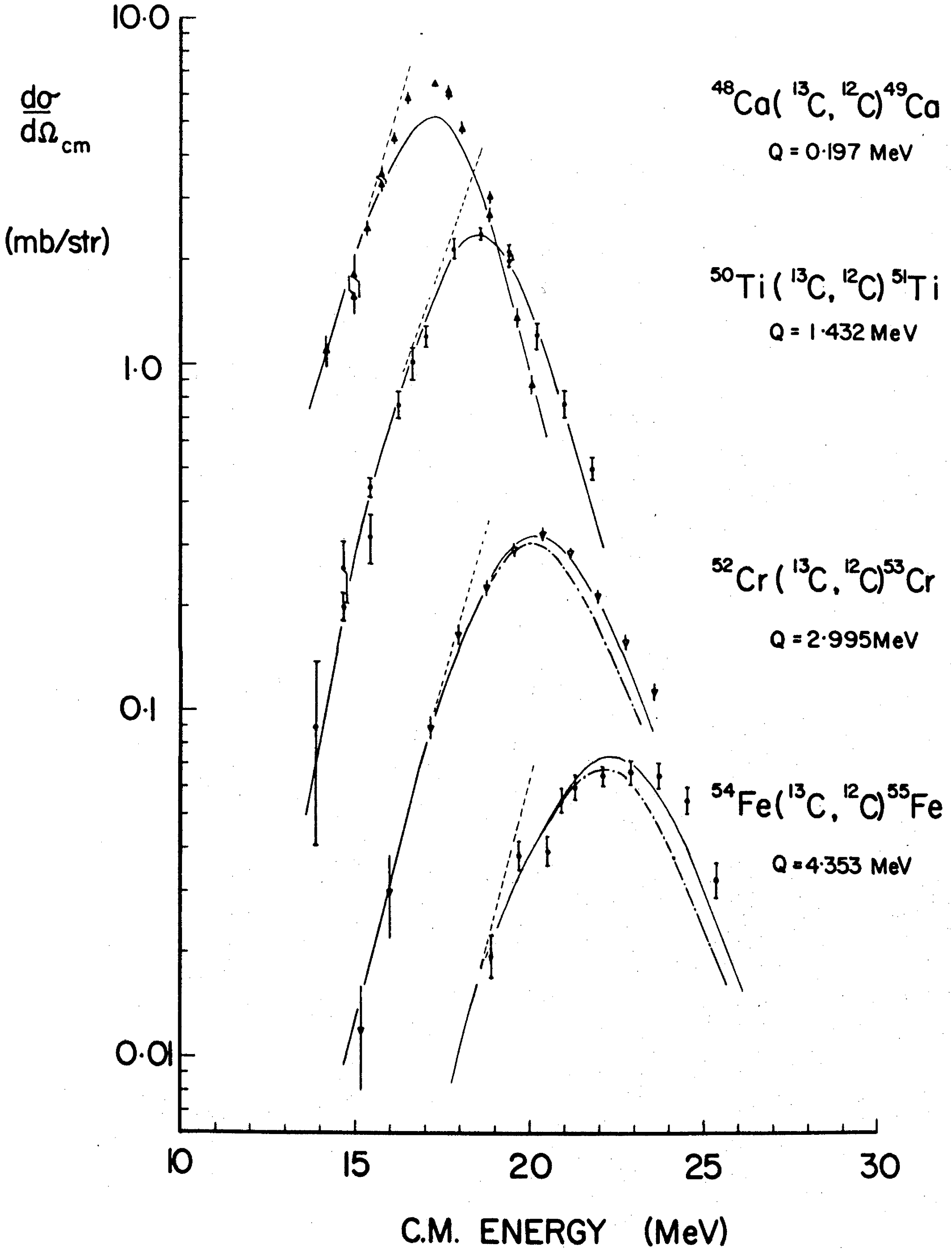

Fig.4.23 Single neutron transfer to the ground states of N=29 nuclei. The solid curves are calculated with parameter from tables 4.8 and 4.9. The dashed curves were calculated with $V_o=0$ and $W_o=0$. For the dash-dot curves see text.

the Z of the target increases. There are no strong characteristic changes in the 'bell' shapes associated with the different angular momentum transfers.

The physical process and general features of the excitation functions can be qualitively understood using the semi-classical description. In this treatment the incident particle is assumed to approach the target along a Rutherford orbit. At about the apsidal distance D, there is a relatively large probability that the neutron tunnels through the projectile's potential well into that of the target. Following the transfer, the residual projectile emergies along another Rutherford orbit with the appropriate energy and angular momentum. The transfer probability P_t, in the first order perturbation is related to the overlap of the bound state wave functions of the neutron in the projectile and target with the potential ΔV (2.48) and integrated over an average orbit. Clearly, therefore, P_t increases with smaller apsidal distance and with wave functions which extend further from the nuclear interior. Thus P_t depends upon the incident energy and on the configurations occupied by the neutron. The transfer cross-section in the semi-classical description is written as (Br72):

$$\frac{d\sigma_t}{d\Omega} = P_t\left(\frac{d\sigma_{e\ell}}{d\Omega}\right) \qquad 4.12$$

where $(d\sigma_{e\ell}/d\Omega)$ is given by (4.8) and takes into account the absorption above the Coulomb barrier. Christensen *et al* (Ch72b) have shown empirically, using (4.12), that P_t rises exponentially with decreasing D. A near exponential rise is also predicted by the semi-classical calculations of Alder *et al* (Al72). Thus the observed rise in the experimental cross-section reflects the increasing overlap of the bound state wave functions of the neutron, while the fall in cross-section is attributed to the incident and outgoing flux being absorbed into compound nucleus formation or other direct reactions.

4.3.2 DWBA Analysis of the Single Neutron Transfer Measurements

The calculations for the transfer reactions assume that the neutron is transferred from a $1p_{\frac{1}{2}}$ orbit in ^{13}C into a single orbit in the residual nucleus. Hence for each reaction there are two possible angular momentum transfers (normal and non-normal) which can populate a given state in the target (2.56). The non-normal contribution will be shown to be negligible for these reactions, and therefore the calculated cross-section can be written as (Chapter 2)

$$\frac{d\sigma_t}{d\Omega} = S_a S_B \frac{d\sigma_L^{DWBA}}{d\Omega} \qquad 4.13$$

where L refers to the normal angular momentum transfer. This decomposition of $d\sigma_t/d\Omega$ into a nuclear structure part $S_a S_B$ (product of the spectroscopic factors) and the part which describes the dynamics of the reaction is of great value, enabling $S_a S_B$ to be readily extracted by comparison with experiment. The reliability of the value $S_a S_B$ however, depends on the validity of the assumption for the reaction mechanism.

The differential cross-sections ($d\sigma_L^{DWBA}/d\Omega$) were computed using the FFR-DWBA code LOLA in the post representation. The calculations were performed using 55 partial waves and a 0.3 fm integration step length. Increasing the number of partial waves to 80 and decreasing the integration step length to 0.15 fm for $^{48}Ca(^{13}C,^{12}C)^{49}Ca$ (GS) reaction did not change the results. The width of the kernel bond (De73) was set at 3.0 fm for all cases.

The product of the spectroscopic factors $S_a S_B$ was extracted by fitting the theoretical curves to the low incident energy data. The spectroscopic factors thus obtained are independent of any ambiguities in the optical potentials. In fact setting V_o and W_o to zero does not change the value of S_aS_B (fig.4.23). Furthermore, with this procedure of scaling the theoretical curves to the data, it is possible to critically determine whether the reaction model can be extrapolated to higher incident energies.

To perform a DWBA analysis it is necessary to examine the ratio of the transfer to elastic cross-section. For large values of this ratio the Born approximation is considered dubious (He75). Because of the small Q-value and large spectroscopic factor for ^{48}Ca(^{13}C,^{12}C)^{49}Ca (GS) the ratio is quite high at the peak cross-section (0.15 at 18 MeV). Therefore it is debatable whether the DWBA calculations are valid beyond the peak cross-section, however for lower energies the ratio is acceptably low (0.02 at 15 MeV).

4.3.3 Optical Potentials for the Transfer Reactions

The calculation of ($d\sigma_L^{DWBA}/d\Omega$) requires the knowledge of the optical potentials in both the incident and outgoing channels. For the incident channels the OM parameters which reproduce the elastic and available inelastic data are used. However the outgoing channel parameters are only obtained for ^{52}Cr(^{13}C,^{12}C)^{53}Cr and ^{53}Cr(^{12}C,^{13}C)^{53}Cr since ^{49}Ca, ^{51}Ti and ^{55}Fe are unstable to β decay or electron capture. The prescription adopted by most authors (Mo72, Bo73) is to use the same parameters sets for both channels. However, for the present analysis the optical parameters for ^{12}C scattering on the N = 28 are used for the outgoing channel, except for the reactions on ^{52}Cr and ^{53}Cr. This choice should provide a closer representation than the incident channel parameters, since it is only the N = 29 nuclei which are not taken into account precisely.

4.3.4 Bound State Wave Functions (BSWF)

The code LOLA evaluates the radial part of the BSWF for the neutron $R_{n\ell}(r)$ numerically. The potential well for the target and the core of the projectile are assumed to have Wood-Saxon forms. For a given n,ℓ and set of BS parameters (r_o,a), which define the well, the depth of each potential is adjusted by the code to reproduce the known neutron binding energy.

Varying r_o and a by ±5% about $r_o = 1.25$ fm and a = 0.65 fm for the target has shown that the excitation functions only change slightly at high incident energies. No difference in shape occurs when varying the BS parameters of the projectile. Therefore the BS parameters cannot be determined from the shape of experimental excitation functions. However the overall normalisations are a strong function of r_o and a (fig.4.24).

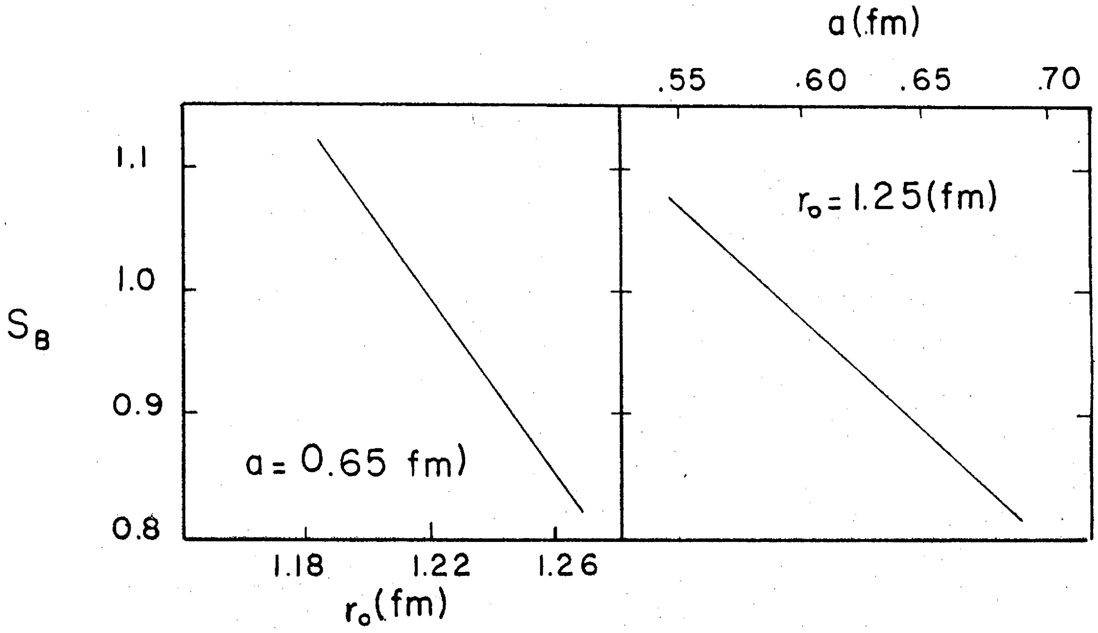

Fig.4.24 The extracted spectroscopic factor for Ca (GS) S_B as a function of bound state parameters.

Therefore, since the product of the spectroscopic factors S_aS_B are determined by fitting the theoretical cross-sections to the data, S_aS_B cannot be extracted accurately without a precise knowledge of r_o and a. This dependence is well known for heavy ion transfer (Go74, Jo74) and also present in sub-Coulomb (d,p) reactions (Ra72).

It has been shown by (Go74) that for values of r_o and a, such that the root mean square radius $<r^2>^{\frac{1}{2}}$ of the BSWF is constant, will give identical results for the extracted S_aS_B. That is S_aS_B depend only on the $<r^2>^{\frac{1}{2}}$ for both the projectile and target. Parkinson (Pa74) has shown, using the DWBA code of Buttle and Golfarb, that a similar result is obtained if the root mean square radius of the potential well of the neutron $<r^2>_p^{\frac{1}{2}}$ is kept fixed. For a Wood-Saxon potential

$$<r^2>_P = \frac{3}{5} R^2 \left[1 + \frac{7}{5} (\frac{\pi a}{R})^2\right] \qquad 4.14$$

where $R = r_o A_{T(P)}^{\frac{1}{3}}$. Parkinson's result has also been confirmed with the program LOLA.

Since accurate values of $<r^2>^{\frac{1}{2}}$ for neutron orbits are not available (Ko71) the BS parameters were fixed at r_o = 1.25 and a = 0.65 for all the targets. These values were chosen from published $^{48}Ca(d,p)^{49}Ca$ (Ra72) and $^{52}Cr(d,p)^{53}Cr$ (Ra68) reactions studies. The spectroscopic factor for ^{12}C + n was fixed at the theoretical value of Cohen and Kurath(Co67), S_a = 0.61. This is in good agreement with measured values of S_a = 0.66 (De73) and S_a = 0.59 (Be76) both using the reaction $^{13}C(^{12}C,^{13}C)^{12}C$ and S_a = 0.83 from the (d,p) reaction (Mi72). The BS parameters for ^{12}C were fixed at r_o = 1.220 fm and a = 0.60 fm, which were chosen to give S_B = 1.0 (Ra72, Be68) for ^{49}Ca (GS) when the theoretical curve was fitted to the data points at low incident energy. This procedure was adopted because when the set r_o = 1.25 fm and a = 0.65 fm (De73) was used the extracted spectroscopic factors were 33% low. All the spectroscopic factors were normalised to the ^{48}Ca + n value because of its experimental reliability. The $^{48}Ca(d,p)^{49}Ca$ experiment (Ra72) was performed below the Coulomb barrier and thus the spectroscopic factor is independent of optical potential ambiguities. Further, the large single particle strength for ^{49}Ca (GS) is acceptable because the ^{48}Ca core is doubly magic.

The SNT data has been previously analysed by Parkinson (Pa74) using the DWBA code written by Buttle and Golfarb (Bu71). Unlike LOLA, this code uses a no-recoil (zero-range) approximation and the BSWF's are replaced by Hankel functions, which together make the calculations much simpler. These approximations have been shown to be valid for transfer at energies below the Coulomb barrier, but are poor for higher incident energies (De73, Bu71). Moreover, the no-recoil approximation used does not give the same results in the post and prior representation and therefore violates the basic theory (Chapter 2, Section 2.4.1).

Parkinson analysed the SNT data using optical parameters which did not give a good description of the elastic scattering measurements. Clearly for incident energies where the Coulomb wave functions are significantly disturbed by the nuclear field, the comparison between theory and experiment is not acceptable. Indeed Parkinson did not claim validity at these energies. However for energies below the barrier the use of an approximate effective potential is justified (Pa74), in fact, the theory reproduces the low energy data very well.

4.3.5 Transfer to the Ground States of the N = 29 Nuclei

The ground states of ^{49}Ca, ^{51}Ti, ^{53}Cr and ^{55}Fe all have a closed neutron shell N = 28 with an extra neutron predominantly in the $2p_{3/2}$ orbit (Ve66), while ^{13}C has a GS spin assignment of $J^{\pi} = \frac{1}{2}^{-}$. Thus for each of these reactions the angular momentum transfer L (2.53) is either L = 1 (non-normal) or L = 2 (normal).

The normal and non-normal L contributions to the cross-sections of ^{48}Ca(^{13}C,^{12}C)^{49}Ca (GS) and ^{54}Fe(^{13}C,^{12}C)^{55}Fe (GS) are shown in fig.4.25. Clearly, the cross-sections for L = 1 are negligible and are therefore ignored. Similar results were obtained for the ^{50}Ti and ^{53}Cr targets.

The computed differential cross-sections are compared to the data in fig.4.23. The optical potentials, BS parameters and spectroscopic factors used are shown in tables 4.8 and 4.9. The DWBA calculations reproduce the experimentally measured rise in cross-section with energy for all the excitation functions. For the ^{54}Fe(^{13}C,^{12}C)^{55}Fe case however, the data does not extend to low enough energy and hence the steep gradient is not well defined. At higher incident energies the ^{50}Ti(^{13}C,^{12}C)^{51}Ti (GS) data is very well reproduced and to a less extent the ^{52}Cr(^{13}C,^{12}C)^{53}Cr (GS) and ^{54}Fe(^{13}C,^{12}C)^{55}Fe (GS) reactions. For the latter two reactions when the appropriate OM potentials (table 4.1) were used in the incident channels, discrepancies occur at high energy (dashed-dot curves, fig.4.23). Better agreement was obtained (solid curves, 4.23) when the imaginary potential for ^{52}Cr(^{12}C,^{12}C)^{52}Cr* (table 4.6) was used in the incident channels for ^{52}Cr(^{13}C,^{12}C)^{53}Cr and ^{54}Fe(^{13}C,^{12}C)^{55}Fe. Further, the quality of the fits for ^{52}Cr(^{13}C,^{13}C)^{52}Cr* and ^{54}Fe(^{13}C,^{13}C)^{54}Fe* with these potentials (table 4.8) change insignificantly, and similarly for the corresponding elastic data.

The inverse reaction ^{53}Cr(^{12}C,^{13}C)^{52}Cr (GS) is reproduced by the calculation (fig.4.26) using the same parameters used for ^{52}Cr(^{13}C,^{12}C)^{53}Cr (GS) (tables 4.8, 4.9). The errors associated with ^{53}Cr(^{12}C,^{13}C)^{52}Cr (GS) are large and a detailed comparison is not possible.

The ^{48}Ca(^{13}C,^{12}C)^{49}Ca (GS) data is not well fitted by the theory. The energy of the peak cross-section is reproduced but the calculation underestimates it's magnitude by 20%. This discrepancy could be attributed to the large $(d\sigma_t/d\sigma_{e\ell})_{EXP}$, although it is not clear whether this effect

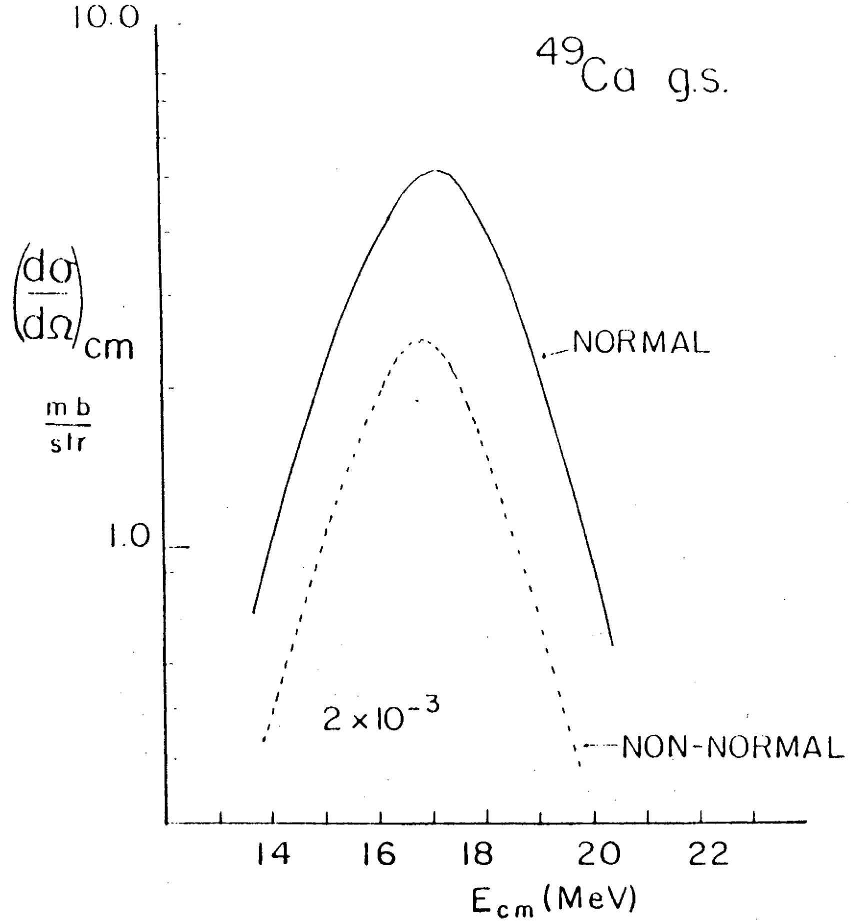

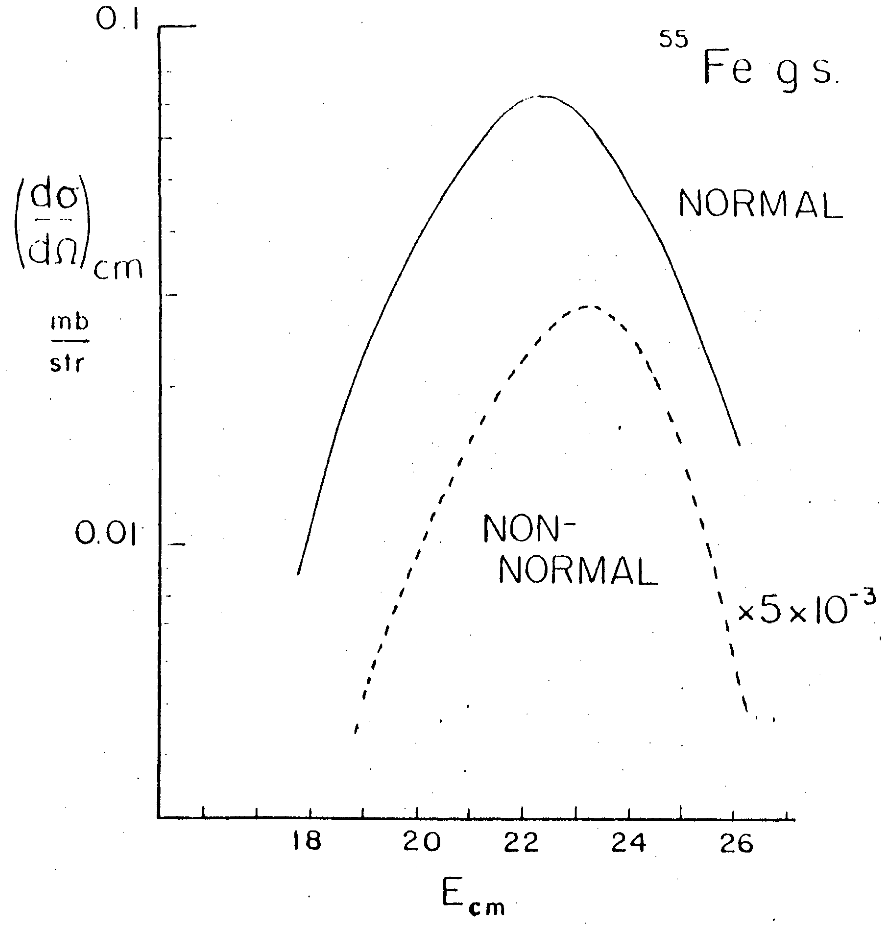

Fig.4.25 Normal and non-normal contributions to the cross to the cross-sections. The curves are calculated with parameters from tables 4.8 and 4.9.

TABLE 4.8

Optical Potentials Used for the SNT Calculations

Reactions	Channel	V_o(MeV)	r_o(fm)	a(fm)	W_o(MeV)	r_o'(fm)	a'(fm)	Set*
$^{48}Ca(^{13}C,^{12}C)^{49}Ca$	in	50.0	1.33	0.41	5.0	1.33	0.41	2b
	out	50.0	1.24	0.50	3.4	1.24	0.50	1a
$^{50}Ti(^{13}C,^{12}C)^{51}Ti$	in	50.0	1.23	0.51	7.9	1.23	0.51	4a
	out	50.0	1.24	0.49	7.0	1.24	0.49	3a
$^{52}Cr(^{13}C,^{12}C)^{53}Cr$	in	50.0	1.30	0.42	5.0	1.2	0.43	(5a)†
	out	50.0	1.28	0.45	3.2	1.28	0.45	7a
$^{53}Cr(^{12}C,^{13}C)^{52}Cr$	in	50.0	1.30	0.42	5.0	1.2	0.43	(5a)†
	out	50.0	1.28	0.45	3.2	1.28	0.45	7a
$^{54}Fe(^{13}C,^{12}C)^{55}Fe$	in	50.0	1.30	0.43	5.0	1.2	0.43	(8a)†
	out	50.0	1.28	0.43	3.0	1.28	0.43	9a

*The sets refer to tables 4.1(a) and 4.1(b)

†Imaginary poten not as in table 4.1(a)

TABLE 4.9

Spectroscopic Factors

	J^{π}	S_B 1)	S_B 2)	S_B
^{49}Ca (GS)	$3/2^-$	1 3)		1.0 4)
^{50}Ti (GS)	$3/2^-$	0.84	0.91 ±0.09	0.82 5)
(1.16 MeV)	$1/2^-$	0.62	0.86 ±0.08	0.58 5)
(2.14 MeV)	$5/2^-$	0.51	0.39 ±0.04	0.24 5)
(2.19 MeV)	$3/2^-$	0.11	0.085±0.01	0.06 5)
^{53}Cr (GS)	$3/2^-$	0.60	0.63 ±0.13	0.72 6)
(2.32 MeV)	$3/2^-$	0.30	0.30 ±0.06	0.40 6)
(3.59 MeV)	$3/2^-$	—	0.15 ±0.003	
(3.61 MeV)	$1/2^-$	—		0.45 6)
(3.71 MeV)	$9/2^-$	—	0.52 ±0.2	0.52 6)
^{55}Fe (GS)	$3/2^-$	0.56	0.65 ±0.11	

The BS parameters for ^{12}C where r_o = 1.22 fm, a = 0.60 fm and those of the targets r_o = 1.25 fm, a = 0.65 fm

1) Present work, assuming S_a = 0.61 (Co66)

2) (Ve66)

3) BS parameters for ^{13}C were adjusted to make this spectroscopic factor unity

4) (Ra72)

5) (G168)

6) (De69)

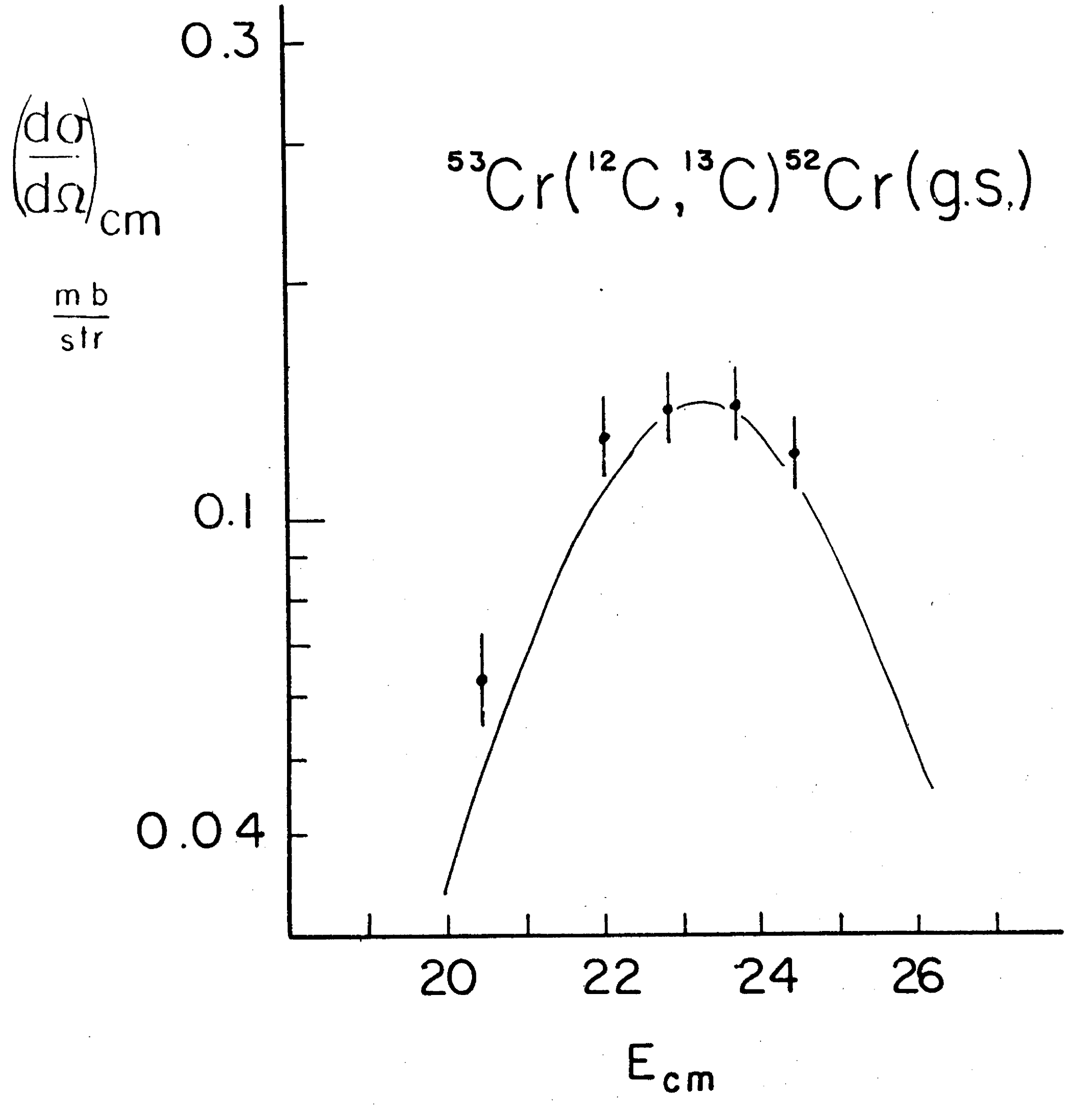

Fig.4.26 Fit to the $^{53}Cr(^{12}C,^{13}C)^{52}Cr$ with parameters from tables 4.8 and 4.9.

might be caused by a poor choice of optical potential. When the OM set 2a (table 4.1a) was used in the incident channel, the fit above 20 MeV (Lab) was totally unacceptable, because the relatively large imaginary potential W_o = 22 MeV, absorbed too much flux.

It is important to note that the optical potentials used in the incident and outgoing channels are predominantly from the three parameter searches on the elastic data (see table 4.8). The sets from the two parameter searches generally gave a larger discrepancy at high incident energy.

The extracted spectroscopic factors from these reactions are compared to published values in table 4.9.

4.3.6 Single Neutron Transfer to Excited States of ^{51}Ti

The SNT data to the 1.16 MeV and unresolved 2.136-2.189 MeV excited states of ^{51}Ti are shown together with the DWBA predictions in fig.4.27. The optical potentials and BS parameters used for the calculations are the same as the ones used for the transfer to the ground state.

The 1.16 MeV level is a strong single particle $2p_{\frac{1}{2}}$ state (S_B = 0.86 (Ve66)). The non-normal contribution to the cross-section (L = 1) is a factor of 100 smaller than for the normal component (L = 0). The data to this state are restricted to low bombarding energies, hence a detailed comparison with the theory is not possible. However the extracted spectroscopic factor is in good agreement with the value from (d,p) work (G168).

With the experimental energy resolution it was not possible to resolve the 2.136 MeV and 2.189 MeV levels. Therefore an attempt was made to reproduce the data by a simple addition of the calculated cross-

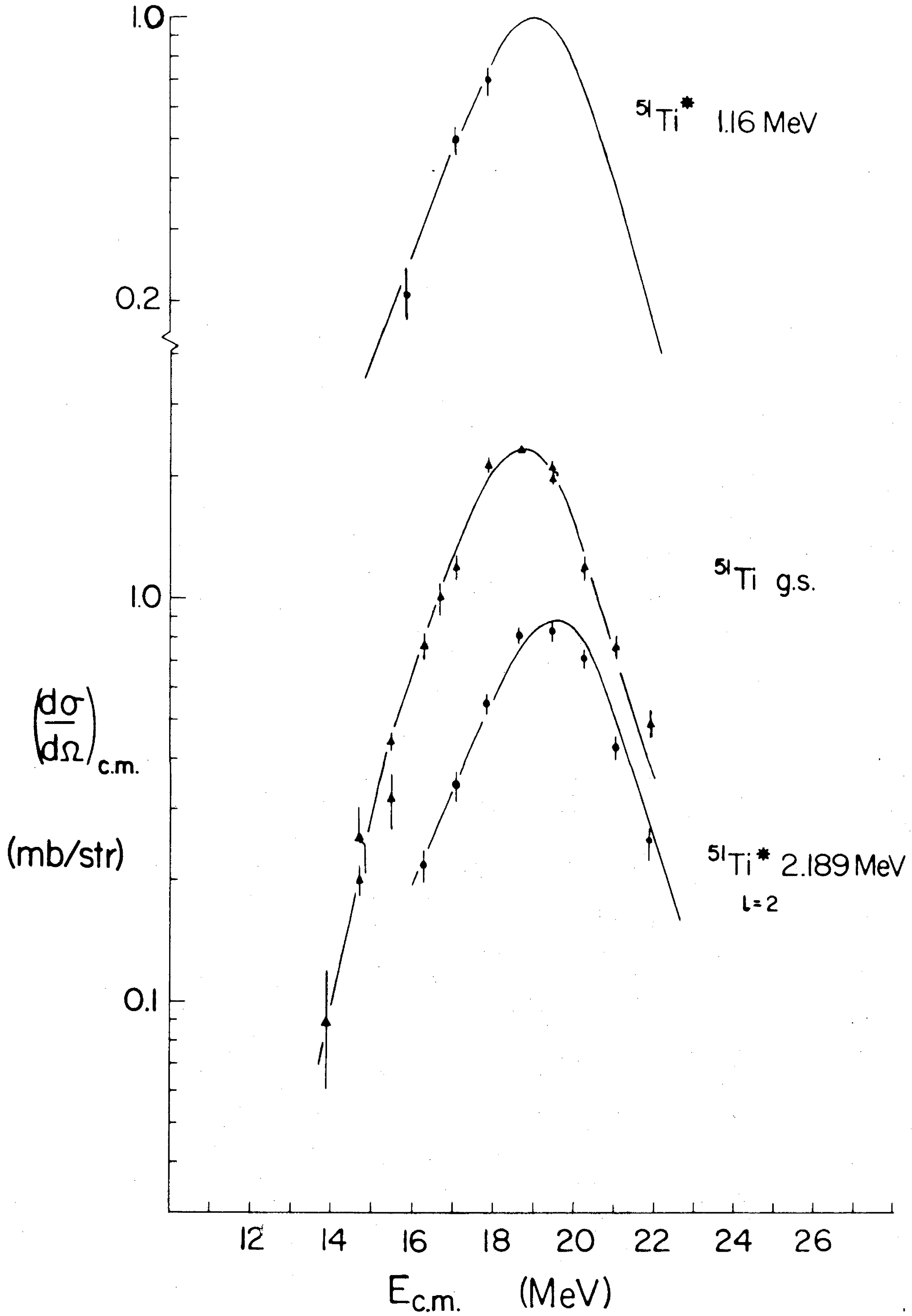

Fig.4.27 Single neutron transfer to the ground state and excited states of ^{51}Ti. The fits to the curves are calculated with parameters from tables 4.8 and 4.9.

sections from the individual states. The spectroscopic factors used in the calculation were in the ratio of $S_B(2.136)/S_B(2.189) = 4.6$ (G168, Ve66).

The 2.136 MeV and 2.189 MeV levels have configurations $1f_{5/2}$ and $2p_{3/2}$ respectively (G168, Ve66), therefore the normal angular momentum is $L = 2$ in each case. The fit to the data is shown in fig.4.27. The cross-section for the 2.189 MeV level is approximately a factor of 3 larger than for the 2.136 MeV state, this is inspite of the large ratio for $S_B(2.136)/S_B(2.189)$. This is because the $2p_{3/2}$ BSWF has an extra node and therefore has a relatively large value at large radii.

From this analysis the extracted spectroscopic factors of the 2.136 MeV and 2.189 MeV states are 30% higher than the calculated (Ve66) and measured values (G168) (table 4.9). It is important to note that the extracted spectroscopic factors depend critically on the value of the ratio $S_B(2.136)/S_B(2.189)$, because of the large contribution from the $2p_{3/2}$. Increasing $S_B(2.189)$ from 0.085 to 0.135, the calculation reproduces the magnitude of the experimental cross-section without changing $S_B(2.14)$. Adopting this procedure is not unreasonable since the cross-section for transfer to this state in (d,p) work is small and could have a much larger error than the one quoted in the literature.

4.3.7 Single Neutron Transfer to the Excited States of ^{53}Cr

The 2.32 MeV level in ^{53}Cr has a configuration $2p_{3/2}$ (De69), hence the normal angular momentum transfer to this state is $L = 2$. The measured excitation function is well reproduced by DWBA with optical potentials used for the transfer to the GS (fig.4.28). The extracted spectroscopic factor is in agreement with the values given by (De69, Ve66).

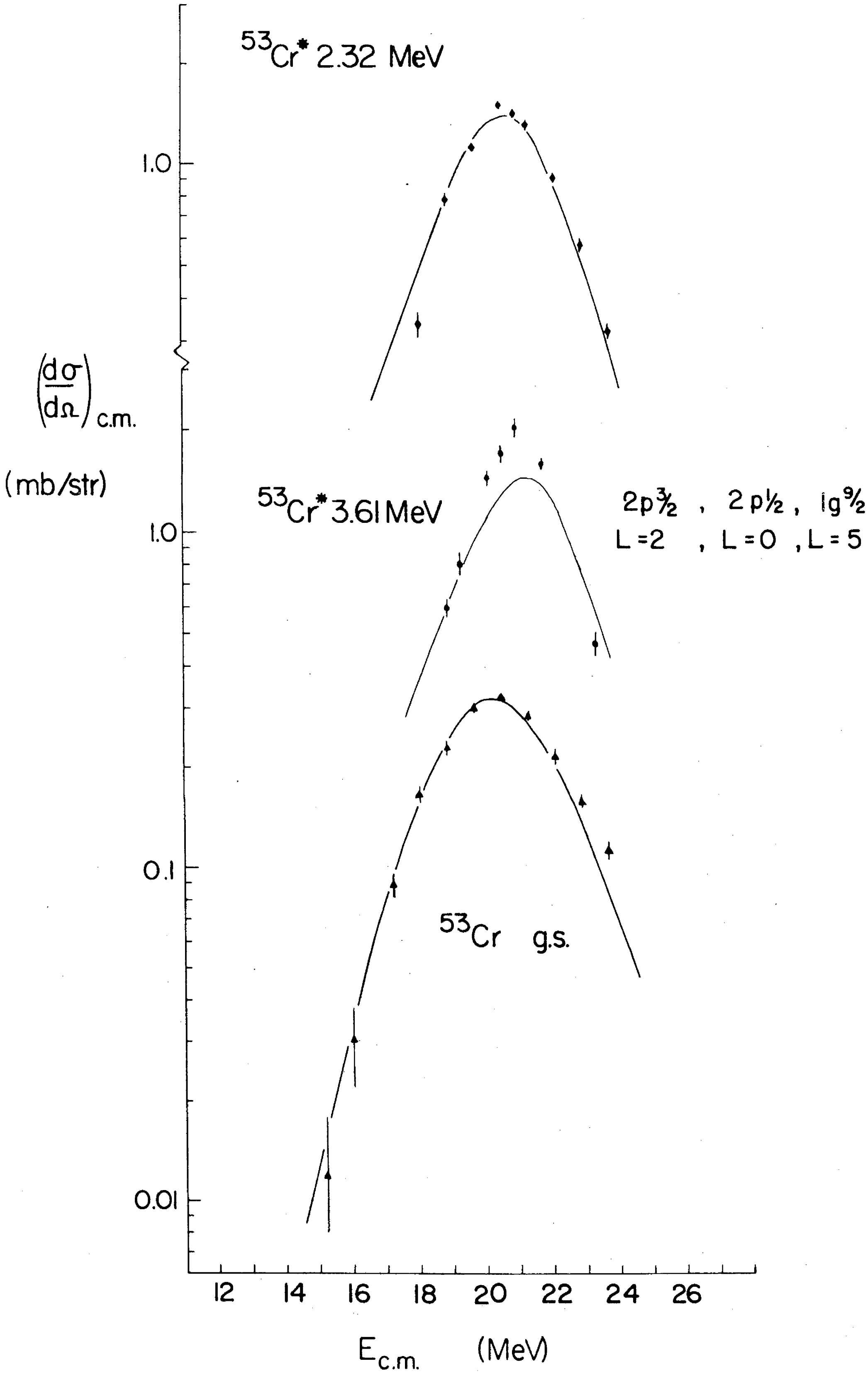

Fig.4.28 Single neutron transfer to the ground state and excited states of ^{52}Cr. The fits to the curves are calculated with parameters from tables 4.8 and 4.9.

The excited state of ^{53}Cr at 3.61 MeV ($2p_{1/2}$) has two other states within 100 keV, namely 3.59 MeV ($2p_{3/2}$)and 3.71 MeV ($1g_{9/2}$) states (De69, Ra68) which are not resolved. Attempts to get fits to the data by adding the calculated cross-sections from the individual states gave unsatisfactory results (fig.4.28). The calculation has the wrong gradient at low energy side of the bell shape which indicates that the disagreement does not stem from inappropriate OM parameters. The disagreement can be traced to the calculated contribution from the $2p_{1/2}$ state which has the largest cross-section but too low a gradient. The $1g_{9/2}$ does have the appropriate gradient but underestimates the data by a factor of 4. Further, the calculated peak cross-section is shifted to higher energy with respect to the data by 300 keV. No satisfactory reason for these discrepancies can be given. However it is important to point out that there is no reason to suspect that theory is inadequate since good fits and spectroscopic factors were obtained for the other two excitation functions on ^{52}Cr.

Chapter 5

DISCUSSION AND CONCLUSIONS

The elastic data has been shown to be reasonably well reproduced by the OM with the same geometry for the real and imaginary Wood-Saxon potentials. The parameters V_o, r_o and a are well determined since the quality of the fits to the elastic and inelastic data are sensitive to small changes in these parameters. On the other hand W_o is poorly determined. The insensitivity to W_o is partially reflected in the fact that the sets from the two and three free parameter searches give equally good fits to the elastic and inelastic data. However, the single nucleon transfer excitation functions are better described with OM parameter sets from the three free parameter searches. This indicates that the imaginary potential might be better defined by the transfer reactions.

The parameters obtained from the OM analysis of the elastic scattering measurements have average values of r_o and a of 1.28 fm and 0.46 fm respectively and are consistent with previously published results (Be73, Ch73, Zi75), for similar projectile-target combinations at incident energies around the Coulomb barrier. However they are in disagreement with sets obtained at higher bombarding energies where r_o and a are typically 1.15 fm and 0.70 fm respectively (Sa75b). This change in the parameter sets with bombarding energy, has been suggested by Satchler (Sa75b), to indicate deficiencies in the Wood-Saxon parameterisation. It should be noted however, that to obtain a good fit to some of the present elastic and corresponding inelastic scattering data, a relatively larger a and smaller r_o are generally required. This is compared to the sets obtained from the analysis of the elastic scattering data alone. This would indicate that the deficiencies suggested by Satchler would not exist if the optical potential is required to give a good representation of both the elastic and inelastic data.

Another feature of the extracted OM potentials is that the ratio of the imaginary to the real potential at the strong absorption radius is small ($\simeq 0.1$) for all the potentials with the exception of those for ^{18}O scattering. Similar results have been reported (Or71, Bo72, Ch73, Cu74) for incident energies about the Coulomb barrier. The large imaginary potential for ^{18}O scattering compared to ^{16}O can be attributed to the two neutrons outside ^{16}O core which have a smaller binding energy than the nucleons in the core. Therefore the number of open inelastic and transfer channels is much larger than for ^{16}O, hence the difference in the imaginary potentials. This conclusion is supported by the OM and coupled channel Born approximation (CCBA) analysis of the ^{58}Ni(^{16}O,^{16}O)^{58}Ni ^{58}Ni(^{18}O,^{18}O)^{58}Ni and ^{64}Ni(^{16}O,^{16}O)^{64}Ni and ^{64}Ni(^{18}O,^{18}O)^{64}Ni performed by Videbæk *et al* (Vi76). When using the OM, the ratio $W_o/V_o \approx 0.2$ for ^{16}O and $W_o/V_o \approx 0.4$ for ^{18}O were obtained but when the inelastic channel (^{18}O,^{18}O*) is explicitly taken into account using the CCBA the ratio W_o/V_o becomes ≈ 0.2 for ^{18}O. Therefore this indicates that an increase in the number of open channels results in a larger imaginary potential.

The optical potentials for ^{12}C and ^{13}C scattering show an increase in r_o and decrease in a with target nucleon number A_T (figs. 4.9a and 4.9b). A similar result is observed for ^{16}O + ^{40}Ca, ^{44}Ca, ^{52}Cr, ^{62}Ni elastic scattering (Ei72). Further, the Coulomb barrier V_B (Equation 1.1) for carbon and oxygen scattering, calculated with parameters from tables 4.1(a) and 4.4 show an almost linear increase with atomic number. This is consistent with extracted values of V_B by Obst *et al* (Ob72) and Williams *et al* (Wi75) and is due to the increase in the Coulomb potential.

In fig.5.1, values of V_B for oxygen scattering are compared with those of Obst *et al* (Ob72). The extracted barrier radii R_B (Equation 1.1) are well parameterised by $r_{oB}(A_T^{\frac{1}{3}} + A_P^{\frac{1}{3}})$ with $r_{oB} \simeq 1.56$ fm for carbon and $r_{oB} \simeq 1.52$ fm for oxygen. The strong absorption radii can also be parameterised in the same way $D_{\frac{1}{2}} = r_{oD}(A_T^{\frac{1}{3}} + A_P^{\frac{1}{3}})$ and give $r_{oD} \simeq 1.58$ fm for both oxygen and carbon scattering.

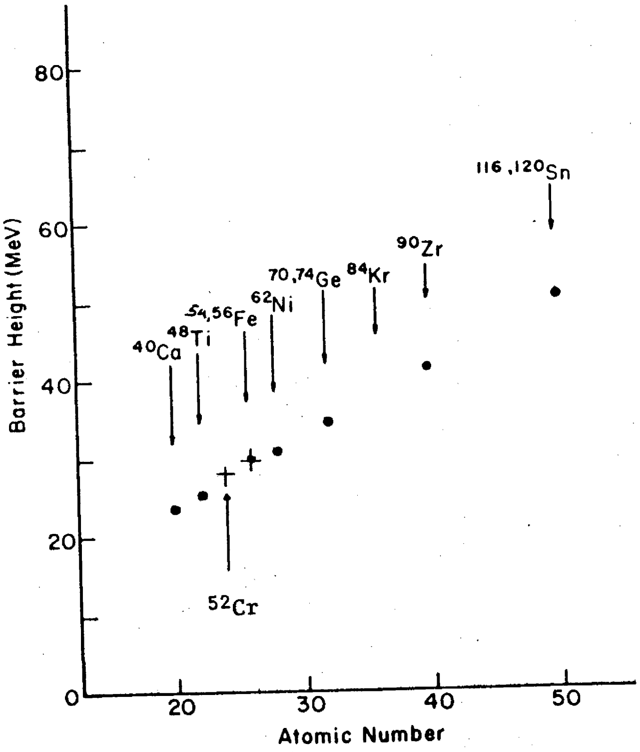

Fig.5.1 Barrier heights for $^{16}O + {}^{52}Cr$ and $^{16}O + {}^{54}Fe$ (+). The other barrier heights (●) are from (Ob72).

Calculating the $\mathbb{R}e\ \tilde{V}_N$ at $D_{\frac{1}{2}}$ shows that it is approximately 1 MeV (table 5.1) which indicates that elastic scattering is dominated by Coulomb scattering because $\tilde{V}_C(D_{\frac{1}{2}}) \simeq 20$ MeV. Also, $D_{\frac{1}{2}} \simeq 9.5$ fm (table 5.1) and since elastic and inelastic scattering and single nucleon transfer have the same localisation (Mo76), the measured reactions occur far out on the nuclear surface, approximately 2 fms beyond the nuclear touching distance $1.28\ (A_T^{\frac{1}{3}} + A_P^{\frac{1}{3}})$ fm. Therefore the reactions studied are indeed peripheral. Furthermore, in almost all instances the extracted values of R_B, V_B, $D_{\frac{1}{2}}$, $\mathbb{R}e\ \tilde{V}_N(D_{\frac{1}{2}})$ and $\mathrm{Im}\ \tilde{V}_N(D_{\frac{1}{2}})$, for ^{12}C and ^{13}C and for ^{16}O and ^{18}O have small, but systematic differences. Particularly, the magnitude

TABLE 5.1

Reaction	R_B(fm)	V_B(MeV)*	$D_{\frac{1}{2}}$ (fm)	$-\mathrm{R_e}\ V_N(D_{\frac{1}{2}})$ (Mev)	$-\mathrm{I_m}\ V_N(D_{\frac{1}{2}})$ (MeV)	r_{oB}
^{48}Ca + ^{12}C	9.25	17.60	9.41	0.799	0.056	1.56
^{48}Ca + ^{13}C	9.30	17.45	9.56	1.048	0.1048	1.55
^{50}Ti + ^{12}C	9.24	19.40	9.45	0.831	0.131	1.55
^{50}Ti + ^{13}C	9.35	19.15	9.54	0.847	0.119	1.55
^{52}Cr + ^{12}C	9.41	20.95	9.47	0.964	0.056	1.56
^{52}Cr + ^{13}C	9.64	20.58	9.62	0.971	0.068	1.59
^{53}Cr + ^{12}C	9.53	20.75	9.56	0.917	0.059	1.58
^{54}Fe + ^{12}C	9.38	22.82	9.48	0.985	0.059	1.55
^{54}Fe + ^{13}C	9.65	22.24	9.65	1.046	0.073	1.57
^{52}Cr + ^{16}O	9.60	27.25	9.80	1.04	0.167	1.53
^{52}Cr + ^{18}O	9.61	27.02	10.02	0.85	0.455	1.51
^{54}Fe + ^{16}O	9.58	29.44	9.97	0.90	0.09	1.52
^{54}Fe + ^{18}O	9.62	29.24	10.02	0.95	0.51	1.50

*Centre of Mass barrier heights

of $\mathrm{Im}\,\tilde{V}_N(D_{\frac{1}{2}})$ and $\mathbb{R}\mathrm{e}\,\tilde{V}_N(D_{\frac{1}{2}})$ are slightly larger for ^{13}C than for ^{12}C. The more absorptive potential for ^{13}C is expected. A larger $|\mathbb{R}\mathrm{e}\,\tilde{V}_N(D_{\frac{1}{2}})|$ for ^{13}C naively suggest that ^{13}C has a mass distribution extending further radially than for ^{12}C. This is contrary to what is expected from electron scattering measurements (fig.5.2) and would imply that ^{13}C has a neutron skin. However, (i) electron scattering is not very sensitive to the tail of the charge distribution (Jo76), and (ii) it is difficult to draw any definite conclusions about the mass distribution of the projectiles from $\mathbb{R}\mathrm{e}\,\tilde{V}_N$, because it might critically depend upon the microscopic properties of the combined system as a whole (Ei72).

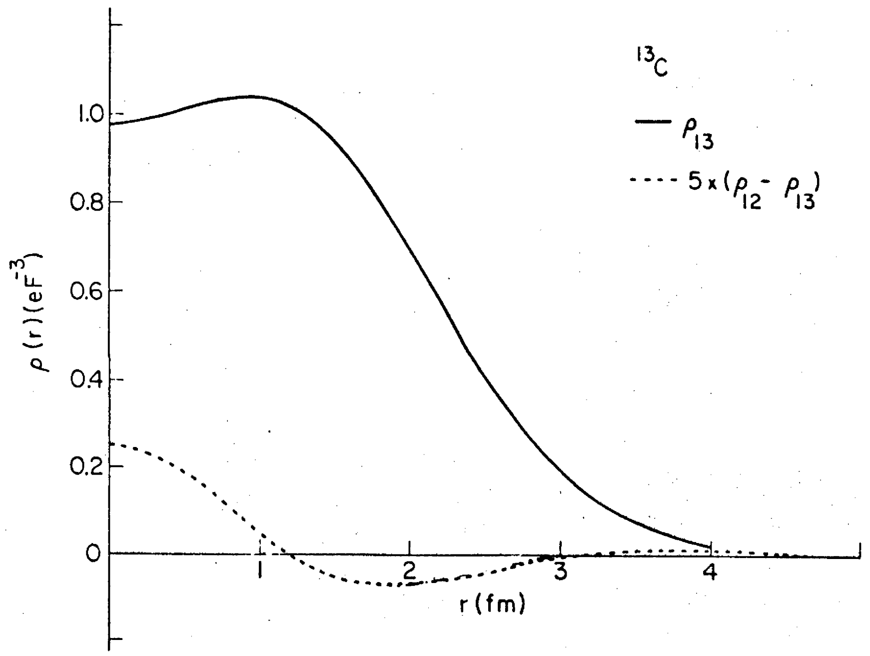

Fig.5.2 Charge distribution for ^{13}C (solid); the experimental ^{12}C-^{13}C difference (dashed) (He70).

The present inelastic scattering measurements at 120° (lab) have an advantage over those performed at forward angles in that only one classical orbit contributes, hence there are no additional complications due to interfering trajectories (Gl74). Further, for back angle measurements the nuclear and Coulomb inelastic amplitudes are approximately of equal magnitude at the interference minimum, while for small angle scattering the Coulomb amplitude could be a factor of two larger (Co76). Thus the cross-sections at back angles are more sensitive to the geometry of the nuclear form factor. Furthermore for these measurements, the nuclear interaction, which is not well understood, can be accurately compared with the well known Coulomb interaction and any erroneous assumptions about the former should be more apparent.

The sensitivity of the inelastic scattering was exploited in this work by measuring cross-sections for inelastic scattering induced by ^{12}C, ^{13}C, ^{16}O and ^{18}O. By using a series of isotopes as projectiles to excite a state in a given nucleus, the Coulomb interaction is the same. This is because the Coulomb form factor does not depend upon the charge distributions of the projectiles and the excitation energy, reduced matrix elements and atomic numbers are the same. Therefore the measured differences between the excitation functions of ^{12}C and ^{13}C and between ^{16}O and ^{18}O can be only due to different reaction mechanisms or ion-ion potentials. Indeed the various shapes of the excitations are quantitatively reproduced by DWBA using collective form factors with different optical potentials.

The main discrepancies in the fits arise at high incident energies where the theoretical curves overestimate the data. However at these energies the first order calculations might be suspect because the experimental elastic and inelastic cross-sections are of comparable magnitude (He75). This implies that the inelastic flux removed from the elastic channel can be coupled back to the ground state, or to transfer and other inelastic channels. Indeed, the CCBA calculation (St74) for ^{56}Fe(^{16}O,^{16}O)^{56}Fe* (2^+, 0.86 MeV), unlike DWBA, does not overestimate the data at small apsidal distance, yet both calculations give very similar results below and around the interference minimum.

The OM potentials which give optimum fits to the elastic data do not necessarily give good quantitive fits to the inelastic data. It is shown that this discrepancy may be removed by performing grid searches on the OM parameters; thus the measurement of inelastic scattering imposes additional constraints on the choice of potential. This does not mean that the elastic scattering measurements are redundant, for as shown in fig.5.3, a set can be found that gives an excellent fit to the inelastic data, yet gives a totally unacceptable one to the elastic data. Clearly such a set is not appropriate.

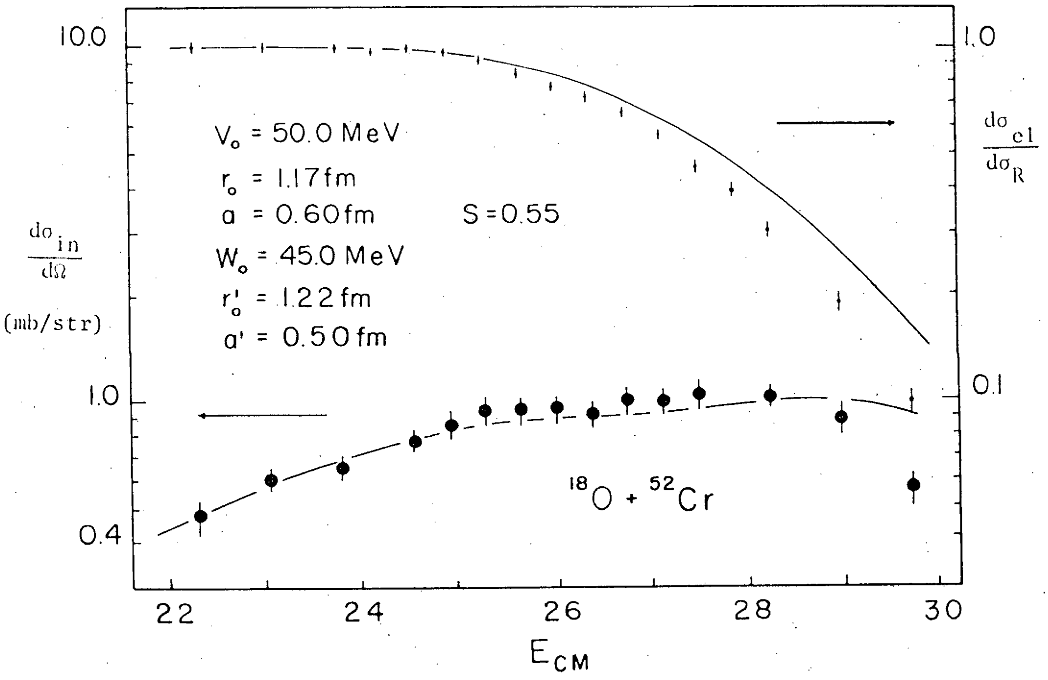

Fig.5.3

It is interesting to note that for those cases where a grid search was necessary the resulting potential tails are more diffuse compared to those obtained from just the elastic scattering. This choice of potentials is necessary to fit the inelastic data, particularly in the cases where the interference minimum is very pronounced. No systematic study of potential ambiguities was attempted. However by demanding that a given set reproduces two or three reactions, the effective ion-ion potential is accurately determined in the region of the strong absorption radius (Ch73, Pe73, Go76). A good example of this is the scattering of the carbon isotopes on ^{52}Cr and ^{54}Fe where the parameters for just the elastic scattering are very similar, yet when the inelastic scattering is taken into account the sets are very different. Where grid searches were performed only one set of parameters could be found to fit the data, within the limits of the searches.

In addition to providing a sensitive probe for the optical potential, the inelastic data gives model independent B(E2) values for incident energies below the Coulomb barrier. The B(E2)'s for ^{52}Cr (1.434 MeV) and ^{54}Fe (1.409 MeV) from the various reactions are consistent with each other and with most values obtained from Coulomb excitation (table 4.5). Also, above the Coulomb barrier, the optical potential deformation parameters, β_N are obtained (table 4.4) and are consistent with values from (p,p'), (α,α') and (^{16}O,^{16}O) experiments (table 4.5). The extracted β_N values for ^{12}C, ^{13}C and ^{16}O on the two targets are β_N = 0.16-0.17 and do not show any dependence on the projectile used. It is more appropriate however, to examine the variation of $R_T\beta_N/R_T^{c'}\beta_c$ for the different projectiles since in the inelastic scattering experiments the nuclear and Coulomb form factors are stringently compared. Table 4.4 shows that there is indeed a rough correlation with the incident projectile. This is not surprising since $R_T\beta_N$ represents the deformation length of the ion-ion potential which changes with incident projectile on a given target, while $\beta_c R_T^{c'}$, the charge density deformation length of the target, is fixed. Further, it is shown using crude folding model calculations that in order to extract parameters representative of the target mass deformation the projectile mass distribution has to be explicitly taken into account.

For ^{18}O induced inelastic scattering the extracted β_N's are considerably lower (27%) than those for ^{16}O and the carbon projectiles. Such small values of β_N were necessary to fit the inelastic data and since fits with a large number of optical potentials were attempted (1.00 fm $\leq r_o \leq$ 1.34 fm, 0.40 fm $\leq a \leq$ 0.72 fm, V_o = 50 MeV, W_o = 45 MeV, a' = 0.50 fm, r_o' = 1.2 fm) it can be stated with reasonable certainty that this discrepancy is not due to an inappropriate choice of optical potentials. Values of β_N consistent with the ones obtained for ^{16}O scattering result in a rise in the cross-section before the monotonic fall at high incident energies which is inconsistent with the data. Further, the small β_N cannot be attributed to the large imaginary potential required by the elastic scattering, in fact a smaller W_o gives rise to a pronounced interference minimum which is clearly not present in the data. This inconsistency might indicate some inadequacy of the collective form factor. However a more likely cause of this discrepancy is that DWBA is not applicable for this reaction because ^{18}O induced reactions, unlike ^{16}O, tend to be very sensitive to multistep processes (Co76, Re75, Vi76). This conclusion can be strengthened by noting that when using higher values of β_N, the discrepancies between theory and experiment occur predominantly at high incident energies where multistep are expected to be larger (G174). Therefore coupled channel calculations might be necessary to establish the cause of this discrepancy.

The full finite range DWBA calculations are, on the whole, in good agreement with the experimental measurements. The steep gradient of the low energy data is well reproduced for all cases with the exception of the ^{52}Cr(^{13}C,^{12}C)^{53}Cr (3.59 MeV) reaction. The spectroscopic factors were obtained from the low energy data and are therefore independent of any optical potential ambiguities, although the extracted spectroscopic factors are very sensitive to small changes in the bound states parameters.

To obtain spectroscopic factors in agreement with calculated values by Vervier (Ve66) and measured values from light ion work it was necessary to scale the bound state parameters of ^{12}C to give the right spectroscopic factor for ^{49}Ca (GS). The bound state parameters for all the targets were the same ones used for $^{48}Ca(d,p)^{49}Ca$ (Ra72) and $^{52}Cr(d,p)^{53}Cr$ (De69) reactions. Therefore the spectroscopic factors shown in table 4.9 are relative to the value of ^{49}Ca (GS).

The optical parameters used for the SNT calculations (table 4.8) all give a good description to the corresponding elastic data. In the cases of $^{52}Cr(^{13}C,^{12}C)^{53}Cr$ and $^{54}Fe(^{13}C,^{12}C)^{55}Fe$ reactions the incident channel OM parameters also reproduce the inelastic scattering data. Using these parameters the transfer peak cross-sections are well predicted in energy and reasonably well in magnitude with the exceptions of $^{48}Ca(^{13}C,^{12}C)^{49}Ca$ (GS) (see fig.4.26). This shows that the strong Q-value dependence for these reactions is well reproduced, particularly for the $^{54}Fe(^{13}C,^{12}C)^{55}Fe$ reaction, where the Q-value mismatch is relatively large. Further, this shows that spectroscopic factors can be extracted fairly reliably for incident energies where the nuclear potential plays a crucial role, provided appropriate optical potentials are used. Beyond the peak cross-section the theory generally underestimates the experimental points. Attempts to amend these discrepancies by varying the optical potentials showed that weaker imaginary potentials gave better descriptions to the data. However the resulting potentials did not necessarily give good fits to the elastic or inelastic measurements. This could indicate that the outgoing channel OM parameters are not precisely taken into account. Alternatively it might be that one or more assumptions made in the SNT calculations starts to break down as the ions come into closer contact.

The reaction $^{52}Cr(^{13}C,^{12}C)^{53}Cr$ (3.59 MeV) reaction is not reproduced by the DWBA calculations. It is difficult to attribute this inconsistency to inadequacy of the theory since the $^{52}Cr(^{13}C,^{12}C)^{53}Cr$ (GS), $^{53}Cr(^{12}C,^{13}C)^{52}Cr$ (GS) and $^{52}Cr(^{13}C,^{12}C)^{53}Cr$ (2.32 MeV) data are well reproduced, although it might be that the heavy ion transfer mechanism assumed for this state is not appropriate. The experimentally measured excitation function has contribution from three states (3.586 MeV, 3.61 MeV, 3.71 MeV) and an assigned 3.69 MeV state (Ra68) which makes a clear comparison between theory and experiment rather difficult.

In conclusion, the heavy ion reactions induced by the carbon and oxygen isotopes studies in this work have been shown to be physically understood using semi-classical treatments. The OM and DWBA give a quantitive description of the data with relatively minor disagreements at high incident energies. The inelastic scattering reactions induced by ^{12}C, ^{13}C and ^{16}O are consistently described by DWBA. However, coupled channel calculations might be necessary to give satisfactory description of the ^{18}O induced inelastic scattering. Realistic folding model or microscopic calculations might also be necessary to explain the very different optical potentials for ^{12}C and ^{13}C scattering.

REFERENCES

Af68 D.F. Alfonion *et al*, Soviet J.Nucl.Phys. 6, 160 (1968).

Al66 K. Alder and A. Winter, 'Coulomb Excitation', Academic Press (1966).

Al72 K. Alder, R. Morf, M. Pauli and D. Trautmann, Nucl.Phys. A191, 399 (1972).

Au64 N. Austern *et al*, Phys.Rev. 133, B3 (1964).

Au70 N. Austern, 'Direct Nuclear Reaction Theory', Wiley-Interscience, Vol.XXV.

Ba62 R.H. Bassel, G.R. Satchler, R.M. Drisko and E. Rost, Phys.Rev. 128, 2693 (1962).

Ba65 D.L. Barnard et al, Nucl.Phys. 73, 513 (1965).

Ba71 A.R. Barnett, W.R. Phillips, P.J.A. Buttle and L.J.B. Goldfarb, Nucl.Phys. A176, 405 (1971).

Ba75 J.B. Ball *et al*, Nucl.Phys. A252, 208 (1975).

Be35 H.A. Bethe, Phys.Rev. 47, 747 (1935).

Be63 L.C. Becker, F.C. Jobes and J.A. McIntyre, Proc. Third Conf. on Reactions between Complex Nuclei ed. by Chlorso, Diamond and Conzett, Uni. of California (1963).

Be64 J. Bellicard *et al*, Nucl.Phys. 60, 319 (1964).

Be67 R. Beringer, Phys. 18, 1006 (1967).

Be72 F.D. Becchetti *et al*, Phys.Rev. C6, 2215 (1972).

Be73 F.D. Becchetti, P.R. Christensen, V.I. Manko and R.J. Nickes, Nuc.Phys. A203, 1 (1973).

Be76 L. Bennett, Ph.D. thesis, Australian National University (1976) unpublished.

Bi74 P.K. Bindal, K. Nagatani, M.J. Schneider and P.D. Bond, Phys.Rev. C9, 2154 (1974).

Bo53 A. Bohr and B.R. Mottelson, Kgl Danske. Videnskab, Selskab Mat.fys. Medd 27, No.16 (1953).

Bo73 P.D. Bond *et al*, Phys.Lett. 47B, 231 (1973).

Br52 G. Breit, M.H. Hull and R.L. Gluckstern, Phys.Rev. 87, 74 (1952).

Br56 G. Breit and E. Abel, Phys.Rev. 103, 679 (1956)

Br64 G. Breit , Phys.Rev. 135, B1323 (1964).

Br72 R.A. Broglia, S. Landowne and A. Winter, Phys.Lett. 40B, 293 (1972).

Br72b R.A. Broglia and A. Winter, Phys.Rep. 4C, 155 (1972).

Br74 R.A. Broglia, Conf. on Reactions Between Complex Nuclei, Nashville, Tennessee eds. R.L. Robinson *et al* (Amsterdam: North-Holland), vol.2, p.303 (1974).

Br74b D.M. Brink and N. Rowely, Nucl.Phys. A219, 79 (1974).

Bu66 P.J.A. Buttle and L.J.B. Goldfarb, Nucl.Phys. 78, 409 (1966).

Bu71 P.J.A. Buttle and L.J.B. Goldfarb, Nucl.Phys. A176, 299 (1971).
Ch54 K.F. Chackett et al, Phil.Mag. 45, 173 (1954).
Ch73 P.R. Christensen, I. Chernov, E.E. Gross, R. Stokstad and F. Videbæk, Nucl.Phys. A207, 433 (1973).

Ch73b P.R. Christensen, V.I. Manko, F.D. Becchetti and R.J. Nickles, Nucl.Phys. A207, 33 (1973).

Co67 S. Cohen and D. Kurath, Nucl.Phys. A101, 1 (1967).

Co76 M.E. Cobern, N. Lisbona and M.C. Mermaz, Phys.Rev. C13, 674 (1976).

Cu74 A. Cunsolo *et al*, Phys.Rev. C10, 180 (1974).

De69 G. Delic and B. Robson, Nucl.Phys. A134, 470 (1969).

De73 R.M. DeVries, Phys.Rev. C8, 951 (1973).

De74 C.W. de Jager, H. deVries and C. deVries, Atomic and Nuclear Data tables, 14, 479 (1974).

Do74 C.B. Dover and J.P. Vary, 'Symposium on Classical and Quantum mechanical aspects of Heavy Ion Collisions', Heidelberg, Germany (1974).

Ei71 Y. Eisen, Phys.Lett. 37B, 33 (1971).

Ei72 Y. Eisen *et al*, N.P. A195, 513 (1972).

El68 R.V. Elliott, Ph.D. thesis, Australian National University (1968) unpublished.

Fe49 S. Fernbach, R. Serber and T.B. Taylor, Phys.Rev. 75, 1352 (1949).

Fe54 S. Feshbach, C.E. Porter and V.F. Weisskopf, Phys.Rev. 96, 448 (1954).

Fo59 F.W. Ford and J.A. Wheeler, Ann.Phys.(N.Y.) 7, 287 (1959).

Fu64 H.O. Funsten , N.R. Roberson and E. Rost, Phys.Rev.134, B117 (1964).

Gi67 A.F. Gibson *et al*, Phys.Rev. 155, 1208 (1967).

Gl67 N.K. Glendenning, Proc. Intern. School of Physics, 'Enrico Fermi' Course XL, Academic Press (1967).

Gl68 N.K. Glendenning, Ann.Rev.Nuc.Sci. 13, 191 (1963).

Gl74 N.K. Glendenning, Conf. on Reactions Between Complex Nuclei, Nashville, Tennessee eds. R.L. Robinson *et al* (Amsterdam: North-Holland), vol.2, p. 131 (1974).

Go64 M.L. Goldberg and K.M. Watson, 'Collision Theory', Wiley, New York (1964).

Go74 L.J.B. Goldfarb, Conf. on Reactions Between Complex Nuclei, Nashville, Tennessee eds. R.L. Robinson *et al* (Amsterdam: North-Holland), vol.2, p.283 (1974).

Gr68 G.W. Greenlees, G.J. Pyle and Y.C. Tang, Phys.Rev. 171, 1115 (1968)

Gr74 E.E. Gross, H.G. Bingham, H.L. Halbert, D.C. Hensley and M.J. Saltmarsh, Phys.Rev. C10, 45 (1974).

He70 S. Heisenberg, J.S. McCarthy, I. Sick, Nucl.Phys. A157, 435 (1970).

He75 W. Henning, J.P. Schiffer, D.G. Kovar, S. Vigdor, B. Zeidman, Y. Eisen and H.J. Körner, Phys.Lett. 58B, 129 (1975).

Ho66 P.E. Hodgson, Adv. in Phys. 15, 329 (1966).

Ho71 P.E. Hodgson, 'Nuclear Reactions and Nuclear Structure', Clarendor Press, Oxford (1971).

Ig58 G. Igo, Phys.Rev.Lett. 1, 72 (1958).

Ig59 G. Igo, Phys.Rev. 117, 1665 (1959).

Kl73 F.J. Kline *et al*, Nucl.Phys. A209, 381 (1973).

Kn71 H. Knoth *et al*, Phys.Rev. 172, 25 (1971).

Ko71 H.J. Körner and J.P. Schiffer, Phys.Rev.Lett. 27, 1457 (1971).

Ko72 D.G. Kovar *et al*, Phys.Rev.Lett. 29, 1023 (1972).

Ko73 D.G. Kovar *et al*, Phys.Rev.Lett. 30, 1075 (1973).

Ko74 D.G. Kovar, Conf. on Reactions Between Complex Nuclei, Nashville, Tennessee eds. R.L. Robinson *et al* (Amsterdam: North-Holland), vol.2, p.234 (1974).

Ko76 D.G. Kovar, Y. Eisen, T.R. Ophel, B. Zeidman, J.R. Erskine, H.T. Fortune, P. Sperr and E. Vigdor, To be published.

Ja76 H.R. Jagaman and A.Z. Mekjian, Nucl.Phys. A259, 157 (1976).

Je71 A.S. Jensen and C.Y. Wong, Nucl.Phys. A171, 1 (1971).

Jo74 G.D. Jones, J. Durell, J.S. Lilley and W.R. Phillips, Conf. on Reactions Between Complex Nuclei, Nashville, Tennessee eds. R.L. Robinson *et al* (Amsterdam: North-Holland), Vol.1, p.97 (1974).

Jo76 A. Johnson, Private communication.

La74 S. Landowne, 'A Semi-Classical Approach to Heavy ion Collisions', Jahn-Heitner-Inst. für Kernforschung Berline (1974).

Le68 G.H. Lenz and G.M. Temmer, Nucl.Phys. A112, 625 (1968).

Le72 G.M. Lerner and J.B. Marion, Nucl.Phys. A193, 593 (1972).

Le76 J.R. Leigh, E.C. Pollacco, N. Shikazono, D.C. Weisser, and C. Garrett, J.Phys.G:Nucl.Phys., Vol.2, No.3, 62, L39 (1976).

Li72 A.S. Litvinenko *et al*, Sov.J.Nucl.Phys. 14, 23 (1972).

Lo74 K.S. Low and T. Tamura, Phys.Lett. 48B, 285 (1974).

Ma68 G. Mainle, U. Schmidt-Rohr and G.J. Wagner, Nucl.Phys. A115, 570 (1968).

Ma73 R.A. Malfield, S.L. Landowne and V. Rostokin, Phys.Lett. 44B, 238 (1973).

Ma75 V.A. Madsen, 'Nuclear Spectroscopy and Reactions', Ed. J. Cerni, Vol.D, Academic Press, New York and London (1975).

Mc60 J.A. McIntyre, T.L. Watts and F.C. Jobes, Phys.Rev. 119, 1331 (1960).

Mc66 F.K. McGowan *et al*, Proc. Conf. Bases for Nucl. Spin-Parity assignments. Gatlinburg Tenn. (1966).

Me62 A. Messiah, 'Quantum Mechanics', Vol.I&II, North-Holland Publishing Co., Amsterdam (1962).

Mi72 T.J. Miller, F.P. Gibson, R. Hagland, W. Morrison and G. Westley, Nucl.Phys. A191, 1 (1972).

Mo72 G.C. Morrison, H.J. Körner, L.R. Greenwood and R.J. Stimssen, Phys.Rev.Lett. 28, 1662 (1972).

Mo73 P.J. Moffa *et al*, Phys.Rev.Lett. 35, 992 (1973).

Mo76 P.J. Moffa, C.B. Dover and J.P. Va y, Phys.Rev. 13C, 147 (1976).

My74 W.D. Myers, Conf. on Reactions Between Complex Nuclei, Nashville, Tennessee eds. R.L. Robinson *et al* (Amsterdam: North-Holland), vol.2, p.1 (1974).

Na73 K.G. Nair, J.S. Blair , W. Resdorf, W.R. Wharton, W.J. Braithwaite and M. Mehta, Phys.Rev. C8, 1129 (1973).

Ob72 A.W. Obst, D.L. Mcsham and R.H. Davis, Phys.Rev. C6, 1814 (1972).

Or71 J. Orloff and W.W. Daehnick, Phys.Rev. C3, 430 (1971).

Ow64 L.W. Owen and G.R. Satchler, Nucl.Phys. 51, 155 (1964).

Pa74 D.M. Parkinson, Ph.D. thesis, Australian National University (1974) unpublished.

Pe F.G. Perey code 'GENOA', unpublished.

Pe73 D. Pelte and U. Smilansky, Proc. Ninerva Symposium; Lecture notes in Physics, Springer Verlag, Berlin, Heidelberg and New York, 23, 148 (1973).

Ra68 M.N. Rao, J. Rapaport, A. Sperduto and D.L. Smith, Nucl.Phys. A121, 1 (1968).

Ra72 J. Rapaport. A. Sperduto and M. Salomaa, Nucl.Phys. A197, 337 (1972).

Re56 H.L. Reynolds and A. Zucker, Phys.Rev. 101, 166 (1956).

Re75 K.E. Rehm *et al*, Phys.Rev. C12, 1945 (1975).

Ro67 B.A. Robson, OR NL-TM-1831 (1967).

Ro71 B.C. Robinson , Phys.Rev. C4, 2176 (1971).

Sa68 M. Samuel and U. Smilansky, Phys.Lett. 28, 318 (1968).

Sa71 M. Samuel and U. Smilansky, Com.Phys.Comm. 2, 455 (1971).

Sa72 G.R. Satchler, Phys.Lett. 39B, 495 (1972).

Sa74 G.R. Satchler, Conf. on Reactions Between Complex Nuclei, Nashville, Tennessee eds. R.L. Robinson *et al* (Amsterdam: North-Holland), vol.2, p.171 (1974).

Sa75 G.R. Satchler, Phys.Lett. 59B, 121 (1975).

Sa75b G.R. Satchler, Phys.Lett. 59B, 408 (1975).

Sc73 M.J. Schneider *et al*, Phys.Rev.Lett. 31, 320 (1973).

Si65 J.J. Simpson, J.A. Cookson, D. Eccleshall and M.J.L. Yates, Nucl.Phys. 62, 385 (1965).

Si70 R.P. Singal, J.R. Moreira and H.S. Caplon, Phys.Rev.Lett. 24, 73 (1970).

Si75 B. Sinha, Phys.Rep. 20C, 1 (1975).

St64 V.M. Schmitinskii, J.Exptl.Theoret.Phys. 19, No.6, 1041 (1964).

St64b T. Stovall and N.M. Hindz. Phys.Rev. 135, B330 (1964).

Th76 S.T. Thornton, D.E. Gustafson, J.L.C. Ford, K.S. Toth and D.C. Hensley, Phys.Rev. C13, 1502 (1976).

To60 C. Towsley, D. Cline and R.N. Horoshko
University of Rochester, unpublished (1960).

U173 Ulhorn, B. Gonsior, M. Roth and R. Wilde, Proc. Int. Conf. on Nuclear Physics, Vol.1, Munich, North-Holland/American Elsevier (1973).

Va73 J.P. Vary and C.B. Dover, Phys.Rev.Lett. 31, 1510 (1973).

Va74 J.P. Vary and C.B. Dover, 'II. High Energy Heavy Ion Summer Study'. LBL (1975).

Ve66 J. Vervier, Nucl.Phys. 78, 497 (1966).

Vi72 F. Videbæk, I. Chernov, P.R. Christensen and E.E. Gross, Phys.Rev.Lett. 28, 1072 (1972).

Vi76 F. Videbæk, P.R. Christensen, O. Hansen and K. Ulbak, Nucl. Phys. A256, 301 (1976).

Wh74 R.L. White *et al*, Phys.Rev.Lett. 32, 892 (1974).

Wi66 A. Winter and J. Boer, 'Coulomb Excitation' ed. by K. Alder and A. Winter, Academic Press, New York and London (1966).

Wi75 M.E. Williams, R.H. Davis, C.I. Delaune, G.M. Hudson, K.W. Kemper and A. Zeller, Phys.Rev. 11C, 906 (1975).

Wo72 C.Y. Wong, Phys.Lett. 42B, 186 (1972).

Zi75 M.S. Zisman *et al*, Phys.Rev. C11, 809 (1975).